Opto-Magneto-Electrical Nanoactuators for Wireless Cell Stimulation

Zhang Yue

Tesi doctoral

Opto-Magneto-Electrical Nanoactuators for Wireless Cell Stimulation
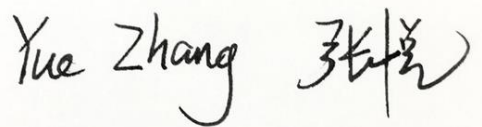
Yue Zhang

UNIVERSITAT DE BARCELONA

Opto-Magneto-Electrical Nanoactuators for Wireless Cell Stimulation

Programa de doctorat en Nanociències

Author:

Yue Zhang

Supervisors:

Dr. Borja Sepulveda

Dr. Jaume Esteve

Tutor:

Alejandro Perez Rodriguez

Lloc on s'ha dut a terme la tesi

Institut Català de Nanociència i Nanotecnologia (ICN2)

Institut de Microelectrònica de Barcelona (IBM-CNM)

UNIVERSITAT DE BARCELONA

Contents

Acknowledgements

Time flies! Three years doctoral journey is coming to an end, this wonderful and fruitful experience will always be in my heart and support me forever. I would like to give my deep gratitude to all the people I came across in this amazing city Barcelona, who had helped, supported and accompanied me during these three years.

First and foremost, I would like to express my deepest appreciation to my supervisor Dr. Borja Sepulveda. Thank you for guiding me in this fantastic and extremely valuable research project, your broad knowledge, critical thinking, inspiring insights have impressed me a lot and will exert a profound influence on me. The completion of my dissertation would not have been possible without your help and support. I am also grateful for all the learning opportunities and care in life you provided to me. I would also like to extend my sincere gratitude to my supervisor Dr. Jaume Esteve Tindo, thank you for all the support and guidance to my research work, whenever I needed some facilities or materials at CNM, you always helped me at the first moment, your practical suggestions and helpful advice played an important role in my work.

Secondly, I also wish to express my gratitude to all the members of Magnetic Nanostructures Group, Dr. Josep Nogués, Dr. María Jośe, Dr. Alex, Javi, Pau, Guba, Nour. I will never forget the memorable funny moments in these years and the team building BBQs, especially the mouth-watering Calçotada! Many thanks to María Jośe for a great amount of assistance with the opto-electric tests, you are always very nice and patient to us. I would also like to thank Alex for offering us a clean and ordered lab environment, a working atmosphere combining pleasure with hard-working. Thanks should also go to Javi and Pau, two Spanish guys in our office, they are so open minded and active, helped me a lot when I needed to make Spanish phone calls, I really cherish our lunch moments in the garden, enjoyed a lot our multifarious topics, and of course Javi's black humor. Guba and Nour are surprises for me, they came one and half years ago, now they are my best friends in Barcelona, thank you both for the pleasurable moments and the mental support, we are "Verduras y Frutas" forever.

I am also grateful to Oriol and Pol, who had performed the cells experiments with the FeGa/ZnO samples for my project. Furthermore, I would like to give my thanks to Manuela, for all her collaboration with HEK 293 cells culture and preparation for the

patch-clamp experiments. I very much appreciate Jośe Cruz for his help with the patch-clamp set up and guidance to the procedures. Thanks also to Andreu and Carolina, who had helped with cells experiments and Si photodiode test.

I would like to acknowledge the assistance of Raúl, who supported and helped me a lot with the nanofabrication instruments in the clean room at ICN2. Thanks also to Marcos and Francesco, who helped me a lot with the SEM.

I also appreciate the "China Scholarship Council" for providing me the financial support.

Finally, I am deeply grateful to my family: my parents, my brother, my sister-in-law, my lovely niece and nephew, whose care and support motivate me to move on and give me unlimited strength. I LOVE YOU ALL!

Authors' contributions

The work in this thesis was carried out at Catalan Institute of Nanoscience and Nanotechnology (ICN2), Barcelona Microelectronics Institute (IMB-CNM) and Autonomous University of Barcelona (UAB). I contributed to the theoretical analysis, experimental work, data analysis and manuscript writing of this thesis. My supervisor Borja Sepulveda guided this project and participated in the experiments design, data analysis and manuscript modification. The experiments related to cell culture were accomplished by students in Carme Nogues's group at UAB, in which I contributed in the data analysis. The detailed contributions of the main chapters are shown below.

In the work of Chapter 3, I performed the fabrication of Si/Au nanostructured system using the clean room facilities at ICN2 and CNM, the morphological characterization by SEM, and the opto-electric tests for the Si/Au nanostructures through a home-made testing system. The dopants implantation was carried out by technicians at the CNM. Dr. Maria Jose Esplandiu Egido helped with the set up for opto-electric tests and data analysis. The Finite-Difference Time-Domain (FDTD) simulations for the Si/Au nanostructures were conducted in collaboration with Dr. Borja Sepulveda. Cell culture and cell viability assays were done by Nour al Hoda Bast at UAB, and I was involved in the results analyses.

In the work of Chapter 4, I performed the main fabrication steps of the FeGa/ZnO nanodomes in PDMS film, including colloidal self-assembly of nanospheres, PDMS curing and peeling off, and ICP-RIE to produce the hollow nanodomes. Dr. Jordina Fornell Beringues performed the sputtering of the FeGa/ZnO layers and the vibrating-sample magnetometer tests at the Materials Science Department of UAB. Besides, I analyzed SEM and EDX for the samples at ICN2, and tested the photothermal effect of the FeGa/ZnO nanodomes in PDMS film with help of Pau Guell Grau. Cell culture and cell viability assays were done by Oriol Careta Borràs and Pol Torres Vila in the biolab at UAB, and I was involved in the preparation and optimization of the samples for cell culture, and in the analysis of the results.

Resumen

Los tratamientos clínicos basados en la estimulación eléctrica de células excitables han sido eficaces y ampliamente utilizados para una variedad de enfermedades. Sin embargo, estos dispositivos a menudo están limitados por su volumen, la necesidad de electrodos con cableado externo y la incapacidad de actuar en células específicas. Los dispositivos implantables que pueden convertir la energía óptica o magnética en estímulos localizados eléctricos o térmicos para activar las células, son alternativas prometedoras debido a su mínima invasividad, capacidad para estimular células de forma inalámbrica con alta resolución espacial y temporal.

Este proyecto de Tesis se ha centrado en el diseño racional y la fabricación de nanomateriales opto-eléctricos y magneto-opto-eléctricos de alto rendimiento para la estimulación celular inalámbrica. Actualmente, los estimuladores opto-eléctricos generalmente requieren luz visible de baja penetración en los tejido y altas intensidades, lo que limita su aplicación a implantes muy superficiales, y que incluso podrían causar daño tisular debido al calentamiento térmico excesivo. Por lo tanto, todavía es necesario aumentar drásticamente la eficiencia de actuación de los dispositivos implantables actuando en las ventanas biológicas del infrarrojo cercano (NIR) para lograr una actuación maximizada y segura en tejidos más profundos. Por otro lado, aunque el campo magnético puede penetrar a través de los tejidos sin atenuación, los estimuladores magnético-eléctricos generalmente proporcionan una pobre precisión espacial y temporal de las actividades celulares inducidas. Por lo tanto, es necesario conseguir estimuladores magneto-eléctricos con una resolución espacial más alta, más eficiente, y con una actuación de respuesta más rápida. En esta Tesis, se han desarrollado dos tipos de nanomateriales opto-eléctricos y magneto-opto eléctricos para superar estos desafíos.

El primer nanomaterial que fue estudiado y desarrollado está basado nanoestructuras de Si/Au para conseguir estimulación opto-eléctrica en la primera y segunda ventanas biológicas con intensidades de luz ultra-bajas. Comenzamos con el diseño racional y el análisis de las propiedades ópticas y electrónicas de las nanoestructuras de Si/Au a través de la combinación de simulaciones de diferencias finitas en el dominio temporal (FDTD) e ingeniería de banda de semiconductores, con el objetivo de maximizar la eficiencia de captura de luz, la separación de cargas fotogeneradas y la inyección de

carga en la solución electrolítica. Las simulaciones de FDTD predijeron que los nanopilares de Si cubiertos por nanodiscos de Au presentan una amplificación de un factor 6 en la absorción de luz en comparación con la oblea de Si, para una longitud de onda alrededor de 800 nm, esto es, dentro de la primera ventana biológica (650-900 nm). Este aumento se debe a la excitación de unas nuevas resonancias híbridas de metal/dieléctrico que permiten un gran aumento de la intensidad de campo electromagnético en la interfaz Si/Au y dentro del nanopilar Si. Cabe resaltar que el incremento del diámetro de los nanopilares permite un corrimiento hacia el rojo de las resonancias, lo que permite amplificar la absorción también en la segunda ventana óptica (950-1100 nm).

A continuación, se realizó un exhaustivo análisis de la respuesta opto-electro-química de nanoestructuras comparando nanodiscos de Au, nanopilares cortos (altura 350 nm) de Si/Au, nanopilares largos (altura 1 μm) de Si/Au sobre uniones p-n, con respecto a la oblea de Si con unión p-n. Se utilizó iluminación de luz pulsada y sinusoidal de 808 nm de longitud de onda en presencia de una solución salina similar a las condiciones fisiológicas. Los nanopilares cortos de Si/Au que solo exponen la región n al electrolito dieron el mayor rendimiento opto-eléctrico, logrando un fotovoltaje de 80 mV a una intensidad de luz ultrabaja de 0.44 μW/mm^2, que fue 11 veces mayor que la oblea de Si con unión p-n. Cabe destacar que esta intensidad de luz es casi 3 órdenes de magnitud menor que la intensidad más pequeña reportada para la estimulación celular, que normalmente requiere voltajes alrededor de los 70-100 mV. La fotocorriente promedio en el nanopilar corto de Si/Au también mostró una mejora sustancial de un factor 2.5 con respecto a la oblea de Si, mostrando una combinación de fotocorriente capacitiva y Faradaica que se pueden sintonizar con la densidad de los nanopilares de Si/Au. En contraste, a pesar de que los nanopilares largos de Si/Au presentaban la mayor absorción óptica teórica, estos mostraron la peor respuesta opto-eléctrica, debido principalmente a la rápida recombinación de carga causada por el cortocircuito de la unión p-n expuesta al electrolito conductor, y al mayor número de defectos superficiales. Además, los nanopilares cortos de Si/Au también proporcionaron el mayor voltaje y fotocorriente para el rango de frecuencia de 1 a 50 kHz, mostrando una ventana de frecuencia de 50-200 Hz para maximizar el voltaje y la fotocorriente para la estimulación celular eficiente.

Los nanopilares cortos de Si/Au presentaron una amplificación aún mayor de la respuesta opto-eléctrica en la segunda ventana biológica con láser de longitud de onda de 1064 nm, logrando una fotovoltaje de 90 mV a una intensidad tan baja como 0.45 $\mu W/mm^2$, que fue 40 veces mayor que la de la oblea de Si con unión p-n.

Finalmente, la biocompatibilidad de las nanoestructuras de Si/Au fue validada por los ensayos de viabilidad celular. Estos resultados sugieren el potencial de los dispositivos nanoestructurados de Si/Au como una alternativa terapéutica prometedora para la actuación opto-eléctrica eficiente en tejidos más profundos con luz infrarroja.

En segundo gran bloque de este trabajo presentamos un nuevo material nanoestructurado de FeGa/ZnO que permita responder simultáneamente a señales ópticas y magnéticas, para convertir la energía entregada en estímulos eléctricos locales y rápidos, con el objetivo de mejorar la versatilidad y la intensidad de actuación remota "wireless". El nanomaterial de FeGa/ZnO está compuesto por matrices de nanocúpulas huecas de FeGa/ZnO integradas en capas elastoméricas flexibles y biocompatibles. El principio de operación propuesto para la estimulación magneto-eléctrica se basa en la magnetostricción de la capa de FeGa para generar una deformación mecánica por un campo magnético externo al cambiar la dirección de la imanación. Esta deformación se transfiere inmediatamente a la capa piezoeléctrica de ZnO para inducir un cambio de voltaje a través de sus propiedades piezoeléctricas. Además, para la estimulación opto-eléctrica, se propone aprovechar la intensa absorción de luz NIR a través de la capa de FeGa para permitir generar un aumento de temperatura local que se transfiere a la capa de ZnO. Este aumento de temperatura del ZnO podría inducir una respuesta piroeléctrica para generar la estimulación eléctrica. En primer lugar, realizamos una optimización del comportamiento magnético de las nanocúpulas de ZnO/FeGa/ZnO con diferentes diámetros y distribución. Los resultados revelaron que las matrices hexagonales compactas de ZnO/FeGa/ZnO con nanocúpulas de 400 nm de diámetro proporcionaron el campo magnético de saturación más bajo y una remanencia mínima, lo cual es esencial para permitir una actuación simple con campos magnéticos pulsados. Además, mostramos que el ataque con SF_6 no afectó el comportamiento magnético de la capa de FeGa, por lo que la capa superior de ZnO se eliminó para proporcionar una menor rigidez a las nanoestructuras que permita una mayor deformación magnetostrictiva. El análisis de las propiedades fototérmicas de las nanoestructuras de FeGa/ZnO optimizadas magnéticamente mostró un intenso calentamiento óptico para

ambas longitudes de onda de luz de 808 nm y 1064 nm, lo que está de acuerdo con la estimación teórica de FDTD de la absorción de luz con alto ancho de banda. Finalmente, se probó la biocompatibilidad de las nanocúpulas de FeGa/ZnO integradas en la película PDMS mediante la evaluación de la viabilidad en células de hueso Saos-2 cultivadas en las muestras. Por lo tanto, las matrices de nanocúpulas de FeGa/ZnO son nanomateriales prometedores para fusionar propiedades magnéticas, ópticas y piezo/piroeléctricas para generar cambios de voltaje local mediante campos magnéticos externos y luz NIR pulsados.

En conclusión, los actuadores celulares nanoestructurados de Si/Au y FeGa/ZnO constituyen nuevas plataformas para la modulación electrofisiológica inalámbrica mediante luz NIR y campo magnético. Mirando hacia el futuro, son prometedores como nanoactuadores inyectables e implantables in vivo debido a las posibles optimizaciones, como la fabricación en sustratos flexibles y la funcionalización de su superficie para su unión a tipos celulares específicos, que podrían ser ampliamente aplicables tanto a los estudios biológicos fundamentales como a terapias clínicas.

Abstract

Clinical treatments based on electrical stimulation of excitable cells have been efficacious and widely used for a variety of diseases. However, these devices are often limited by their bulkiness, need for wiring electrodes and inability to target specific cells. Implantable devices that can directly convert optical or magnetic energy to localized secondary stimulus such as electrical or thermal output to actuate cells are promising alternatives, due to their minimal invasiveness, capacity to stimulate targeted cells wirelessly with high spatial resolution, and flexible signal control with high temporal resolution.

This Thesis project has been focused on the rational design and fabrication of high performance opto-electric and magneto-opto-electric nanomaterials for wireless cell stimulation. Currently, the opto-electric stimulators usually require visible light with low penetration in tissues and high light intensities, which limit their application to very superficial implants and might even cause tissue damage due to excessive thermal heating. Therefore, there is still need to drastically increase the actuation efficiency of implantable devices in the near infrared (NIR) biological windows for achieving safe and maximized actuation in deeper tissues. On the other hand, although the magnetic field can penetrate through the tissues without attenuation, the magnetic-electric stimulators usually provide poor spatial and temporal precision of induced cell activities. Therefore, higher spatial resolution and faster response actuation of the stimulators are needed. In this Thesis, two new types of opto-electric and magneto-opto-electric nanomaterials have been developed to overcome these challenges.

The first nanomaterial under study and development was based on Si/Au nanostructures on Si wafers with p-n junction to achieve opto-electric stimulation in the first and second NIR biological windows with ultralow light intensities. We started with the rational design and analysis of the optical and electronic properties of Si/Au nanostructures by combining finite-difference time-domain (FDTD) simulations and semiconductor band engineering, with the aim of maximizing the light trapping efficiency, the photogenerated charges separation and the charge injection into electrolyte solution. The FDTD simulations predicted that arrays of Si nanopillars capped by Au nanodiscs exhibited 6-fold enhancement of the light absorption compared with the plain Si wafer, for wavelength around 800 nm within the first biological

window. Such enhancement is due to the excitation of novel hybrid metal/dielectric resonances enabling a large enhancement of the electromagnetic field intensity at the Si/Au interface and inside the Si nanopillar. Interestingly, these resonances red-shifted as the diameter of the pillars increased, thus enhancing the light trapping also in the second biological window where the monocrystalline silicon is almost transparent.

Next, we performed an exhaustive experimental opto-electro-chemical analysis of Si/Au nanostructures to compare the properties of Au discs, short Si/Au nanopillars (height 350 nm), long Si/Au nanopillars (height 1 μm) on Si p-n wafer with respect to the plain Si p-n wafer, with pulsed and sinusoidal light illumination of 808 nm wavelength, in an electrolyte solution mimicking the physiological conditions. The short Si/Au nanopillars that only exposed the n-region to the electrolyte gave the highest opto-electric performance, achieving a photovoltage of 80 mV at ultralow light intensity of 0.44 μW/mm^2, which was 11-fold higher than the plain p-n Si wafer. Remarkably, this light intensity is almost 3 orders of magnitude lower than the smallest intensity reported for cell stimulation, which usually requires voltages in the 70-100 mV range. The photocurrent in the short Si/Au nanopillar also showed a substantial 2.5-fold enhancement with respect to the plain Si wafer, showing a combination of light-induced capacitive and Faradaic currents that can be tuned with the density of Si/Au nanopillars. In contrast, although the long Si/Au nanopillars theoretically showed the highest absorption, their opto-electric performance was worse. This was attributed to the fast charge recombination caused by the short-cut of the p-n junction exposed to the conductive electrolyte, and the increased number of surface defects. Besides, the short Si/Au nanopillars also provided the largest photovoltage and photocurrent for the frequency range of 1 to 50 kHz, showing a frequency window of 50-200 Hz to maximize the photovoltage and photocurrent for efficient cell stimulation. The short Si/Au nanopillars presented even higher amplification of the opto-electric response in the second biological window with 1064 nm wavelength laser, achieving a photovoltage of 90 mV at an intensity as low as 0.45 μW/mm^2, which was 40-fold higher than that in the plain p-n Si wafer.

Finally, the biocompatibility of the Si/Au nanostructures was validated by the cell viability assays. These results suggest the potential of the Si/Au nanostructured devices as promising therapeutic alternative for the efficient opto-electric actuation in deeper tissue with safe NIR light.

In the second main block of this work, we presented a novel FeGa/ZnO nanostructured material with the aim of responding to both optical and magnetic signals simultaneously, to generate local and fast electric stimulus that improve the wireless actuation versatility and strength. The FeGa/ZnO nanomaterial was composed of arrays of hollow FeGa/ZnO nanodomes integrated onto soft, flexible and biocompatible elastomeric films. The proposed magneto-electric stimulation is based on the magnetostriction of the FeGa layer to generate mechanical strain by a magnetic field that is immediately transferred to the piezoelectric ZnO layer to induce a voltage change by exploiting its piezoelectric properties. Moreover, the opto-electric stimulation is based on the intense NIR light absorption of the FeGa layer for generating a local temperature increase that is transferred to the ZnO layer. The temperature rise of the ZnO can then be translated into a pyroelectric response, leading to the electrical stimulation. We first optimized the magnetic behaviour of ZnO/FeGa/ZnO nanodomes with different diameters and distribution. The results revealed that the hexagonal-close-packed arrays of ZnO/FeGa/ZnO with 400 nm diameter nanodomes provided the lowest saturation magnetic field and minimal remanence, which is essential to enable simple magnetic pulse excitation. In addition, we showed that SF_6 RIE did not affect the magnetic behaviour of the FeGa layer, thus the top ZnO layer was eliminated to provide lower stiffness for larger magnetostrictive deformation. The photothermal test of the magnetically optimized FeGa/ZnO showed intense optical heating for light wavelengths of 808 nm and 1064 nm, which is in accordance with the FDTD theoretical estimation of the broadband light absorption. Finally, we proved the biocompatibility of the FeGa/ZnO nanodomes integrated onto PDMS film by evaluating the bone Saos-2 cells viability cultured on the samples. Therefore, the arrays of FeGa/ZnO nanodomes are promising nanomaterials to merge magnetic, optical and piezo/pyro-electric properties for generating local voltage change by external magnetic fields and NIR light pulses.

In conclusion, the Si/Au and FeGa/ZnO nanostructured cell actuators present new platforms for wireless electrophysiological modulation through NIR light and magnetic field. Looking forward, they are promising as implantable and injectable nanoactuators in vivo due to the possible optimizations such as fabrication on flexible substrates and surface functionalization for binding to specific cell types, which may be broadly applicable to both fundamental biological studies and clinical therapeutics.

1 Introduction

Electrical activity is ubiquitous in our bodies and it is necessary to keep the homeostasis of several tissues. The basic sources of the physiological electrical activity are electrically excitable cells, which regulate organs and normal activities in our bodies through electrical impulses[1]. For example, motor neurons can be electrically coupled to promote the rhythmic activity of different muscles by the transmission of electrical impulses to skeletal muscle fibers. This provides the mean to control the motor network in our body[2,3]. Malfunction of the excitable cells may lead to a variety of diseases such as neurological diseases (Alzheimer´s disease, Parkinson´s disease, paralysis)[4], and cardiac diseases (bradycardia, tachycardia)[5].

Medical treatments based on the modulation of these electrical impulses have been widely studied and used for repairing lost functions and restoring health. Although effective, current electrotherapeutics have several significant drawbacks as they generally require invasive surgery, wired electrodes, and do not target specific cells, thus encouraging the research of wireless devices capable of converting optical or magnetic energy into electrical signals. Micro- and nanodevices based on opto-electric and magneto-electric materials are becoming promising alternatives due to their minimal invasiveness, reduced size enabling the stimulation at single cell level, and capacity to be remotely powered and to generate the electrical stimulation. In particular, the advances in nanotechnologies and materials science, such as the matured nanofabrication techniques and advanced nanomaterials synthesis, have enabled the development of several types of materials including metallic, semiconductor and organic polymers showing the ability to wirelessly actuate cells and tissues.

In this introduction, the types, signaling mechanism and function of excitable cells are first described. Next, the main diseases associated to the malfunction of excitable cells and current clinical treatments are introduced, stressing their main limitations. Finally, the advantages and problems that should be solved in the emerging optical and magnetic cell stimulation technologies are reviewed.

1.1 Excitable cells

The electrical activity in our body is performed by excitable cells, which can be electrically excited to generate action potentials[6]. Typical excitable cells include neurons, muscle cells (e.g. myocardial cells), and some endocrine cells (e.g. pancreatic β cell). These cells have highly sophisticated electrical signaling mechanisms, allowing electrical impulses travelling across the body through the propagation of action potentials.

1.1.1. Action potential

In nearly all the cell types, the intracellular and extracellular fluids separated by the cell membranes have different ions concentrations. The cell membrane is mainly a phospholipid bilayer across which selective ion pumps work to generate the different ionic concentration, whose typical intra- and extracellular values are given in Table 1[7].

Table 1. Ion concentrations in the intracellular and extracellular fluids of a mammalian cell.[7]

ion	Intracellular concentration / mM	Extracellular concentration / mM
K^+	125	5
Na^+	12	120
Cl^-	5	125
Ca^{2+}	$1*10^{-4}$	2

Such differences in the ions concentration lead to a voltage difference called **membrane potential**, as shown in the simplified structure of a neuron cell membrane in Fig. 1.1[8]. The membrane potential of excitable cells in the baseline state is held at a relatively stable value, denoted as resting membrane potential, which typically is in the -60 mV to -90 mV range.
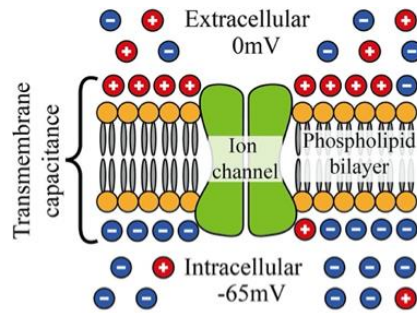
Figure. 1.1. Schematic of the phospholipid bilayer cell membrane, ionic charges and an ion channel.[8] Figure obtained from Ref. 8.

The **action potential** is the main electrical communication mechanism of excitable cells in the body, and consists of a rapid change of the cell membrane potential due to the fast transfer of ions through its integrated ion channels. At the **resting membrane potential** specific types of ion channels are closed (Fig. 1.2 step 1), but they rapidly open when a stimulus (e.g. changes in the surrounding charges, mechanical stress, signaling molecules)[9] induces a potential increase over a threshold value, thus triggering the action potential. A schematic example of an action potential in a neuron is depicted in Fig. 1.2.
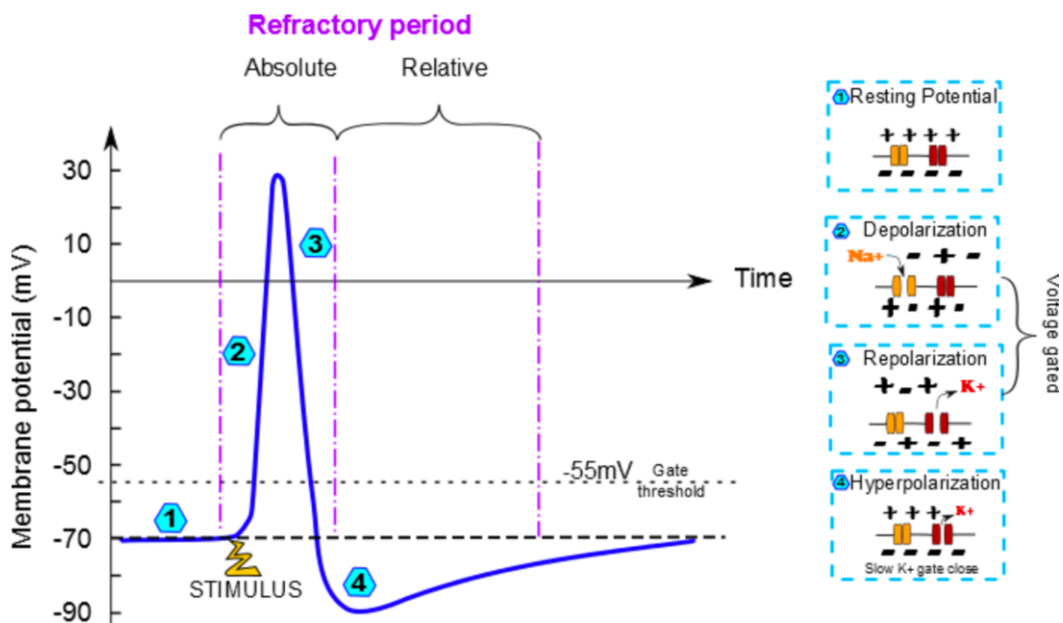
Figure 1.2. Schematic of action potential in a neuron[10]. Figure obtained from Ref. 10.

In more detail, a membrane potential rise over the threshold voltage triggers the **membrane depolarization** (Fig. 1.2 step 2) by opening voltage-dependent sodium channels, which results in a large influx of sodium ions. At the peak of the action potential, the sodium permeability is maximized. Then the sodium channels are rapidly closed and the voltage-gated potassium channels are activated. The large efflux of potassium ions results in the membrane **repolarization** (Fig. 1.2 step 3). However, some of these voltage-gated potassium channels do not close when the membrane potential returns to the resting potential, thus generating a more negative membrane potential than the resting potential. This process is called **hyperpolarization** (Fig. 1.2 step 4) and persists until the potassium permeability returns to its usual value and restores the membrane potential to its resting state[11,12].

The action potentials have two main functions. In neurons they provide the means by which electrical excitation propagates along neuronal axons toward presynaptic terminal for enabling the communication with neighboring neurons. In contrast, in muscle cells or some endocrine cells, the action potentials trigger a rapid influx of calcium ions into these cells for triggering cellular responses such as muscle contraction or hormones release[7].

1.1.2. Function of excitable cells

Excitable cells are very important for the normal function and health of human body. In the nervous system, the electrical impulses travel within and between the neurons, transmitting information towards other parts of the brain and body[1]. These electrical impulses can trigger the muscle contractions in muscle cells, facilitate the control of organs by releasing hormones from various endocrine cells, etc. The main types of excitable cells are neurons, myocytes and endocrine cells.

Neurons have three essential parts: soma, axon, and dendrites. The axons allow neurons transmitting information to other cells, and the dendrites are responsible for receiving the input signals. Neuron-to-neuron communication usually occurs at the synapse, which is a specialized gap structure that permits neurons to pass either electrical or chemical signals to other neurons[13]. Typical structure of chemical and electrical synapses are shown in Figure 1.3[14]. In the case of the chemical synapse, when the action potential arrives at the axon terminal, it triggers the release of neurotransmitters, which move across the synapse cleft and bind the receptors at the postsynaptic terminal,

thus exciting or inhibiting the postsynaptic neuron[15]. On the other hand, at the electrical synapse, an ionic current is directly transferred through the gap junctions that connect the interior of two adjacent cells, enabling synchronization of spiking activity among neurons[16].
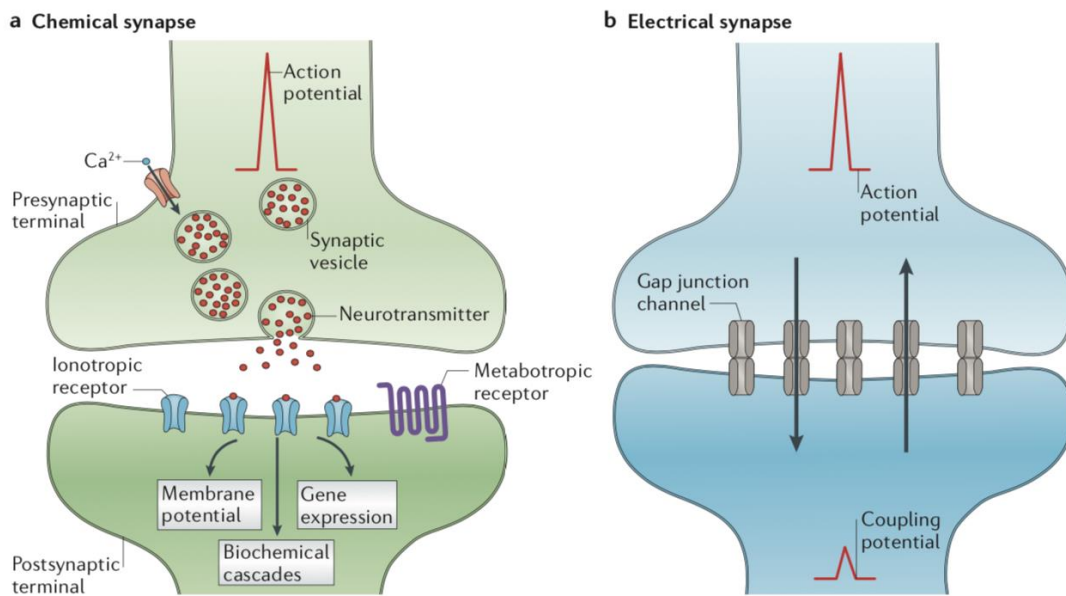
Figure 1.3. Schematic of chemical synapse and electrical synapse. (a) Chemical transmission at a chemical synapse. An action potential activates the voltage-gated calcium channels, leading to neurotransmitter release at the presynaptic terminal, the receptors at the postsynaptic terminal detect and translate the neurotransmitters into various postsynaptic events, ranging from changes in membrane potential to gene expression, etc. (b) Electrical transmission at an electrical synapse, which is mediated by gap junctions that connect the interior of two adjacent cells, thereby directly enable the bidirectional passage of electrical currents by ions.[14] Figure obtained from Ref. 14.

Neurons are typically classified into three different types based on their function: sensory neurons, motor neurons and interneurons[17]. **Sensory neurons** respond to stimulus such as touch, sound or heat that affect the sensory organs, and convey that information to the central nervous system[18,19]. **Motor neurons** get information from the brain and spinal cord and pass these signals to the effector muscles and glands all over the body. **Interneurons** are neural intermediaries located exclusively in the central nervous system that enable the communication between neurons (sensory neurons,

motor neurons or other interneurons), thereby forming simple reflex circuits that help reacting to external stimulus and more complex networks in the brain[20].

Myocytes (also known as muscle cells) are the cells found in muscle tissue. There are various specialized forms of myocytes with distinct properties: cardiac, skeletal, and smooth muscle cells[21].

Cardiac muscle cells (also known as cardiomyocytes) are found in the heart. They are responsible for generating sequential contractile force to ensure the rhythmic beating of the heart to efficiently pump blood to other parts of the body[22]. Its mechanical activity is controlled by electrical impulses with action potential durations as long as 300 ms, which are coordinated by the sequential opening and closing of ion channels[23]. **Skeletal muscle cells** are the building block of the muscle tissues attached to bones and allow the movement and balance control of the body. The skeletal muscle cells can be activated by the acetylcholine neurotransmitter released from motor neurons, which results in membrane depolarization and Ca^{2+} influx. The Ca^{2+} concentration increase activates the endoplasmic reticulum, thus allowing myosins binding to actin filaments to generate the cells and mucscle contraction[24]. **Smooth muscle cells** are found in the digestive system and blood vessels. They obtain the signals from the autonomous nervous system and are responsible for the involuntary contraction of organs such as the stomach and bladder[25].

The **endocrine system** includes eight major glands that produce and release a wide variety of hormones, which travel through our bloodstream to tissues and organs to regulate the body functions[26]. For example, pancreatic β-cells secrete insulin to control blood glucose levels. The electrical activity in these cells is induced by the detection of an increase of the circulating glucose concentration. This opens the voltage-gated Ca^{2+} channels and generates the action potential[24]. On the other hand, thyroid gland cells synthesize thyroid hormones that regulate the body´s metabolism, growth and development. They also help to maintain normal blood pressure, heart rate, and digestion[27]. The adrenal gland cells produce corticosteroids, which regulate the balance of salt and water in the body and the immune system, etc.[28]

1.1.3. Diseases associated to the malfunction of excitable cells

Excitable cells play an important role in the normal electrical activity and the pathophysiology of various biological processes. Therefore, the dysfunction of the excitable cells may lead to a variety of diseases.

The impair of neurons activity may lead to many neurodegenerative diseases. For example, the dendritic integrity of specific neurons is damaged in patients with Alzheimer's disease. Moreover, the abnormal changes of dendritic morphology might also have implications in the neuronal network malfunction and result in neurodegenerative diseases[29]. In addition, the atrophy of astrocytes is involved in a variety of neurological diseases such as amyotrophic lateral sclerosis, Parkinson´s disease, Alzheimer´s disease, and dementia[4]. Some biochemical processes, as the ablation of ferroptosis inhibitor Gpx4 in neurons, can cause rapid motor neuron degeneration leading to paralysis[30]. The overactive voltage-gated ion channels in excitable cells have been associated with the malignant trend in cancer, and play a vital role in the evolution of diseases including congenital myotonia, hyperkalemia, and cardiac arrhythmias[31].

In the case of cardiomyocytes, sodium channels dysfunction that results in slightly shortened action potential duration and slower conduction velocity can induce cardiac arrhythmia. When the heartbeat is too slow (bradycardia) or too rapid (tachycardia), the blood pressure cannot be maintained, which can lead to loss of consciousness, syncope and death[5]. Heartbeats are orchestrated by the coordinated contraction of some specialized cardiomyocytes termed the sinoatrial node (SAN). Sinus node dysfunction may induce many diseases including sinus bradycardia, sinus arrest, etc.[32]

Endocrine diseases occur if the hormone level is too high or too low, or if the body does not respond to the hormones release in a normal way. For example, diabetes is a common endocrine disease, in which the blood glucose level is too high due to the abnormal secretion of insulin hormone. This is caused by the slower glucose-induced oscillatory electrical activity of pancreatic β cells, and by the generation of continuous or intermittent action potentials that are independent of the glucose level[33]. On the other hand, hyperthyroidism is associated to the abnormal electrical cell depolarization in response to thyroid hormones[34]. In addition, adrenal insufficiency occurs when the

adrenal gland releases insufficient cortisol or aldosterone hormone, and the typical symptoms include fatigue, anorexia and dehydration[35].

1.2. Electrical stimulation for therapies

In order to treat the diseases related to the malfunction of excitable cells, electrical therapies to stimulate excitable cells have been intensely researched and used. Treatments based on electrical stimulation have been proved to be effective for various neurological disorder diseases and cardiac diseases. Therefore, it is important to understand how artificial electric stimulation can be induced in excitable cells.

1.2.1. Mechanism of electrical cell stimulation

The excitable cells can be artificially stimulated by electrical signals to generate action potentials. This voltage or current signals can be delivered from electrodes attached to the cell membrane. The electrical characteristics of the cell-electrode interface can be described as an equivalent electrical circuit (Fig. 1.4). In the point-contact model, the cell-electrode interface is simplified to a single point at the cell-electrode cleft. The cell membrane can be represented according to the Hodgkin-Huxley model by a resistance R_m and a capacitance C_m connected in parallel. This electrode model also considers the electrode-electrolyte impedance, which includes the interface capacitance Z_{CPA} and a charge transfer resistance R_{ct}[36,37]. The other elements are described in the figure caption.
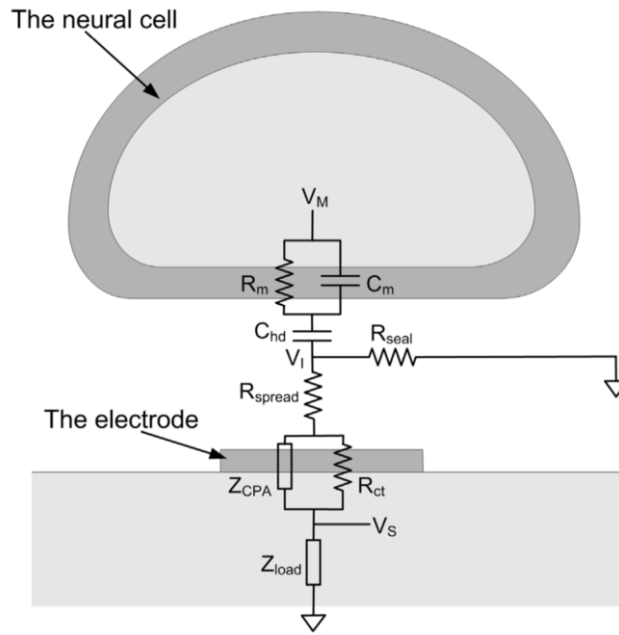
Figure 1.4. Point-contact model of the cell-electrode interface (not to scale).
The attached membrane consists of a resistance R_m in parallel with a capacitance
C_m. C_{hd} represents double layer capacitance at the cell membrane/electrolyte
interface. R_{seal} represents the sealing resistance between the cleft and the
surrounding solution. The electrode consists of an interface capacitance Z_{CPA}, in
parallel with a charge transfer resistance R_{ct}. R_{spread} represents the spreading
resistance for the current spreading from the electrode to the counter electrode. Z_{load}
represents the load impedance of the cell-electrode interface system[36]. Figure
obtained from Ref. 36.

Under electrical actuation, the charge reactions at the cell-electrode interface can be
capacitive or **Faradaic**, depending on the properties of the electrode material, as can
be observed in the schematic illustration of Fig. 1.5. **Capacitive reactions** involve
charging and discharging of the electric double layer at the electrode-electrolyte
interface, which is caused by the redistribution of ionic charges in the electrolyte. In
contrast, **Faradaic reactions** involve the transfer of electrons between the electrode
and the electrolyte due to the oxidation or reduction of some charged species. The real
electrode-electrolyte interface usually exhibits both capacitive and Faradaic reactions,
which are highly dependent on the material and applied voltages[38].
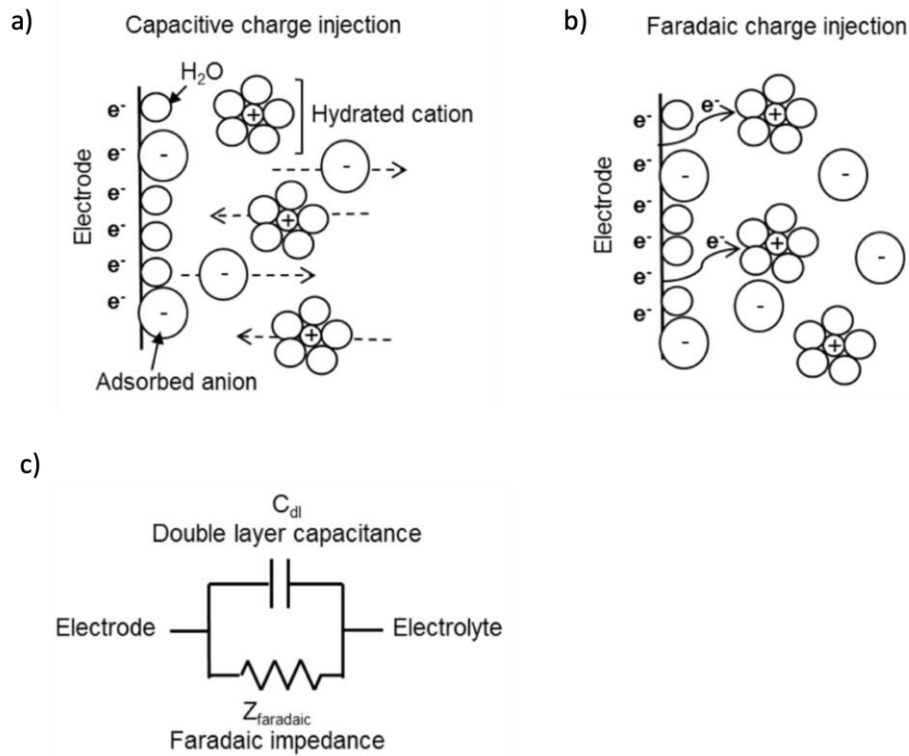
Figure 1.5. Charge injection mechanisms at electrode-electrolyte interface. (a) Schematic illustration of capacitive charge injection mechanism, which includes redistribution of charges at the electrode-electrolyte interface. (b) Schematic illustration of faradic charge injection mechanism, which includes transfer of electrons. (c) Two element circuit model for mechanisms of charge transfer at the electrode-electrolyte interface[38]. Figure obtained from Ref. 38.

1.2.2. Wired electrical stimulation

Clinical electrical stimulation treatments have been efficacious and widely used to treat the diseases associated with the malfunction of excitable cells. For example, implantable cardiac rhythm management devices like defibrillators and pacemakers save millions of lives every year (figure 1.6a)[39], and deep brain stimulation is an increasingly utilized therapy for Parkinson´s disease[40] and epilepsy[41]. Functional electrical stimulation can also activate paralyzed muscles to restore volitional movements (figure 1.6b) [42]. On the other hand, spinal cord stimulation (SCS) is a clinical tool for pain relief (figure 1.6c)[43]. Other examples include retinal prostheses (figure 1.6d)[44,45] or cochlear implants (figure 1.6e) [46] that can help to restore auditory or visual sensations[47], respectively.
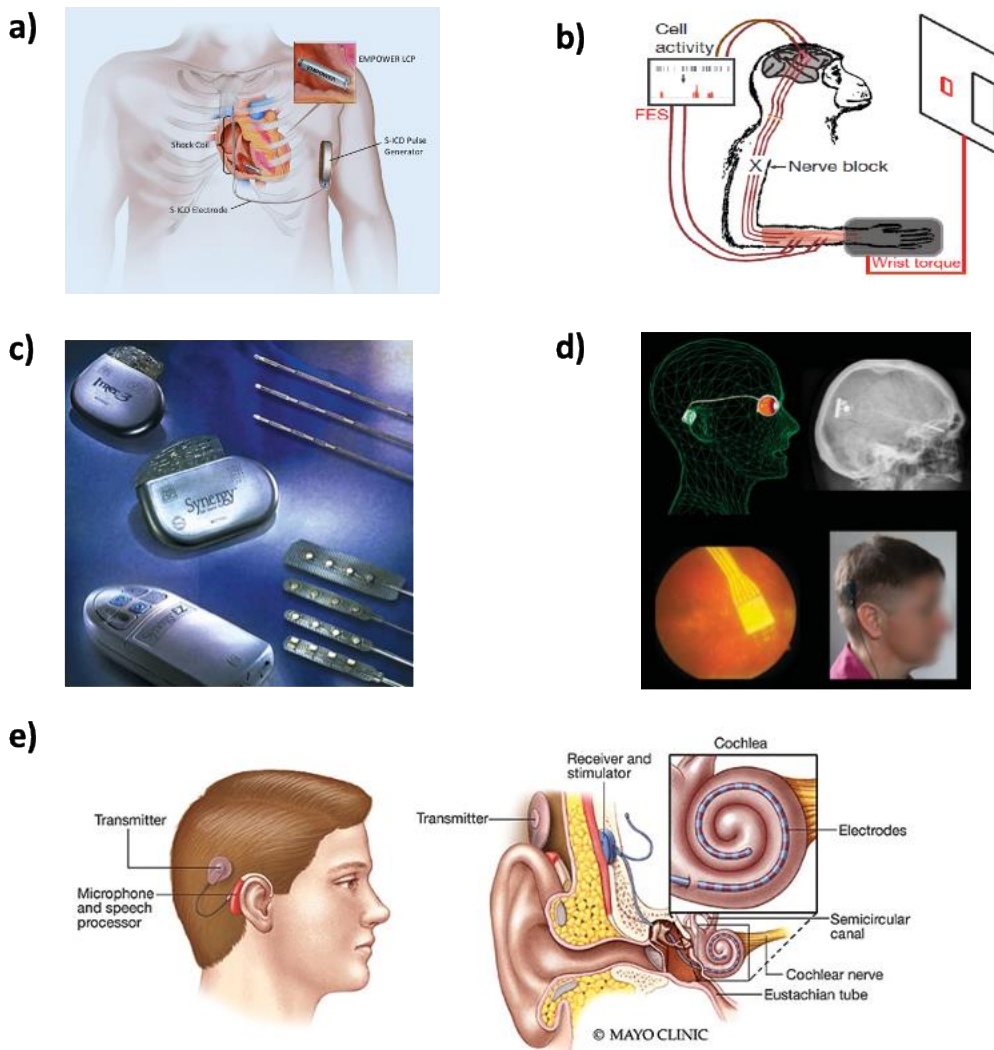
Figure 1.6. Clinical treatments based on electrical stimulation. (a) The modular cardiac rhythm management system (S-ICD: subcutaneous implantable cardioverter–defibrillator, LCP: leadless cardiac pacemaker)[39]. Figure obtained from Ref. 39. (b) Brain-controlled functional electrical stimulation (FES) of muscle during peripheral nerve block[42]. Figure obtained from Ref. 42. (c) Neurostimulator and lead systems used for spinal cord stimulation to treat chronic pain (Medtronic, Inc.) [43]. Figure obtained from Ref. 43. (d) The subretinal visual implant alpha-IMS (Retina Implant AG, Germany)[44]. Figure obtained from Ref. 44. (e) Cochlear implant delivers sound signals directly to the auditory nerve. Figure obtained from "MayoClinic.org".

The subretinal visual implant alpha-IMS is a representative example related to this thesis to show the complexity of current stimulation treatments. As shown in Fig. 1.6d, a subretinal chip with 1500 pixels is surgically implanted beneath the fovea, and it is connected with the subdermal coil behind the ear via a subdermal cable and a thin intraocular foil. The chip is composed of independent microphotodiode-amplifier-electrode elements, which are able to convert light into electrical signals to stimulate the neurons[48]. The subdermal coil receives power and control signals from the transmitter coil (placed above the subdermal coil) via transdermal magnetic induction. The external transmitter coil is powered by a small battery pack in the handheld control unit, by which the patients can turn on/off the device and adjust brightness and contrast sensitivity manually[44].

Although effective, these electronic medical devices are often limited by their bulkiness, the need for wiring electrodes and battery-driven power supply, as well as the inability to target specific cells and to generate precise electrical impulses. Firstly, their implantation or use usually require invasive surgeries, which may induce bacterial infection and severe inflammation[49]. In addition, current electrical devices usually excite or inhibit cells in the tissue indiscriminately, which complicate the clinical effects and may lead to diverse side effects. Lastly, in the neural network, specific neurons generate sets of precise electrical impulses forming the neural circuits, but the neural stimulation devices typically work with simple waveforms, rather than inducing precise modulations at the millisecond timescale[50].

1.2.3. Wireless cell stimulation

To solve some of the problems related to the invasiveness, researchers have been looking for new technologies to realize electrical cell stimulation in a wireless and noninvasive manner. Wireless cell stimulation techniques that directly convert optical, magnetic or acoustic energy to localized secondary stimulus such as electrical or thermal output signals to stimulate cells or tissues provide promising therapeutic alternatives[51,52,53].

A very relevant wireless optical stimulation method that has been developed in the last decades is optogenetics, which uses genetically modified light-activatable ion channels to realize controlled optical modulation of the electrical cell activity at the millisecond timescale. Although effective and non-invasive, its clinical implementation can be

hampered due to the need for genetic transfection[54,55]. On the other hand, implantable nanodevices that can be remotely powered by light or magnetic field are promising to solve aforementioned problems of wired actuators due to their minimal invasiveness, capacity to wirelessly stimulate specific cells with high spatial resolution, and their versatile external actuation control with high temporal resolution[56,57].

1.3. Wireless optical stimulation

Optical cell stimulation has several unique advantages, such as easy light manipulation to target one or more interested cells by finely focused beams, and accurate light power and actuation duration tunability. Emerging studies based on silicon (Si), organic semiconductors and gold (Au) nanostructures have shown significant progress towards implantable and injectable optical cell stimulation devices, exploiting opto-electric or photothermal effects.

In the opto-electric stimulation, light signals are converted by the opto-electric device into electrical outputs to modulate the ions redistribution or the redox state of the chemical species at the cell membrane for eliciting the biological electrical response. The opto-electric stimulation can be accomplished by different effects, such us photovoltaic or photothermal effects.

The **photovoltaic** actuation in a semiconductor is triggered by the induced photovoltage upon light illumination. The photovoltages can generate **photocapacitive** or **photoelectrochemical** actuation, depending on the nature of the materials and the light illumination conditions. The photogenerated charge carriers accumulate near the semiconductor/electrolyte interface, which triggers the migration of electrolyte counterions to the electrode surface forming a Helmholtz double layer. If there is no charge injection, the optical stimulation leads to a transient capacitive current. In contrast, if charges are injected into the electrolyte, light-induced electrons or holes cause redox reactions in the electrolyte species. In both cases, the local cell membrane potential or the local concentration of ions can be altered[58].

On the other hand, in the **photothermal** stimulation the photon energy is absorbed by the materials and dissipated via a non-radiative recombination process, to generate local transient heat[58]. The rapid temperature change can alter the capacitance of the plasma membrane and induce transient capacitive currents to excite the cells[59].

To emphasize recent advances towards wireless optical cell stimulation via opto-electric or photothermal transduction devices, below we discuss the different advanced cell actuators according to the representative materials, which include silicon, organic semiconductors, gold, graphene and quantum dots.

1.3.1. Optical electrostimulation based on silicon

Silicon (Si) has been widely exploited for biophysical research and biomedical applications, due to its low bandgap enabling light absorption over a broad spectral range, highly tunable optical and electrical properties, natural abundance and biocompatibility[60]. Moreover, silicon-based devices can be easily fabricated into various sizes and geometries at the nanometer scale, matching the size of subcellular structures and biological molecules.

Keith and co-workers reported a subretinal prosthesis composed of silicon photodiode arrays, which elicited neural spikes in degenerate rat retina (Fig. 1.7a)[57,61]. They induced the photovoltaic stimulation through near-infrared light pulses (905 nm, pulse length 0.5-4 ms), with low irradiances of 200-1000 μW/mm^2.

Jiang et al. used lipid-supported mesoporous silicon as bioelectric interface to permit optical modulation of the electrophysiology dynamics and elicitation of action potentials in a single neuron. The actuation process was based on fast photothermal effects, using visible light of 532 nm wavelength with intensity of $6.7 \cdot 10^7$ μW/mm^2. The fast response was crucial for the capacitive current generation at the phospholipid bilayer[62].

In addition, Si nanomaterials with various structures such as nanowires, nanoparticles and nanoarrays, have been studied for neural stimulation, tissue actuation, retinal prosthesis, etc.

Si nanowires offer unique advantages given their attractive properties, including one-dimensional structure with high surface-to-volume ratio, well-controlled doping profile during fabrication or synthesis, and fast signal responses[63,64]. They can be well-aligned into arrays for implantation or applied in a drug-like fashion. Coaxial p-type/ intrinsic/ n-type Si nanowires have been proved to be effective to generate photocurrents through a photoelectrochemical process and extracellularly elicit action potentials in DRG neurons in a drug-like manner, using visible light (532 nm) with intensity of $8.6 \cdot 10^5$

µW/mm² [60]. Textured intrinsic Si nanowires have been used to build synapse-like interfaces with cell membranes and to elicit intracellular and intercellular calcium wave propagations via photothermal modulation in a variety of cell types including glial cells, neurons, and cancer cells (Fig. 1.7b), the photothermal effect can be achieved by light illumination of 592 nm wavelength ($2.8 \cdot 10^6$ µW/mm² intensity) [65]. The Si nanowires could also be internalized by glial cells to trigger optical stimulation of intracellular calcium dynamics, which lead to subsequent intercellular calcium wave propagations to the neighboring glial cells and neurons, using visible light (514 nm, $3 \cdot 10^6$ µW/mm²)[66].
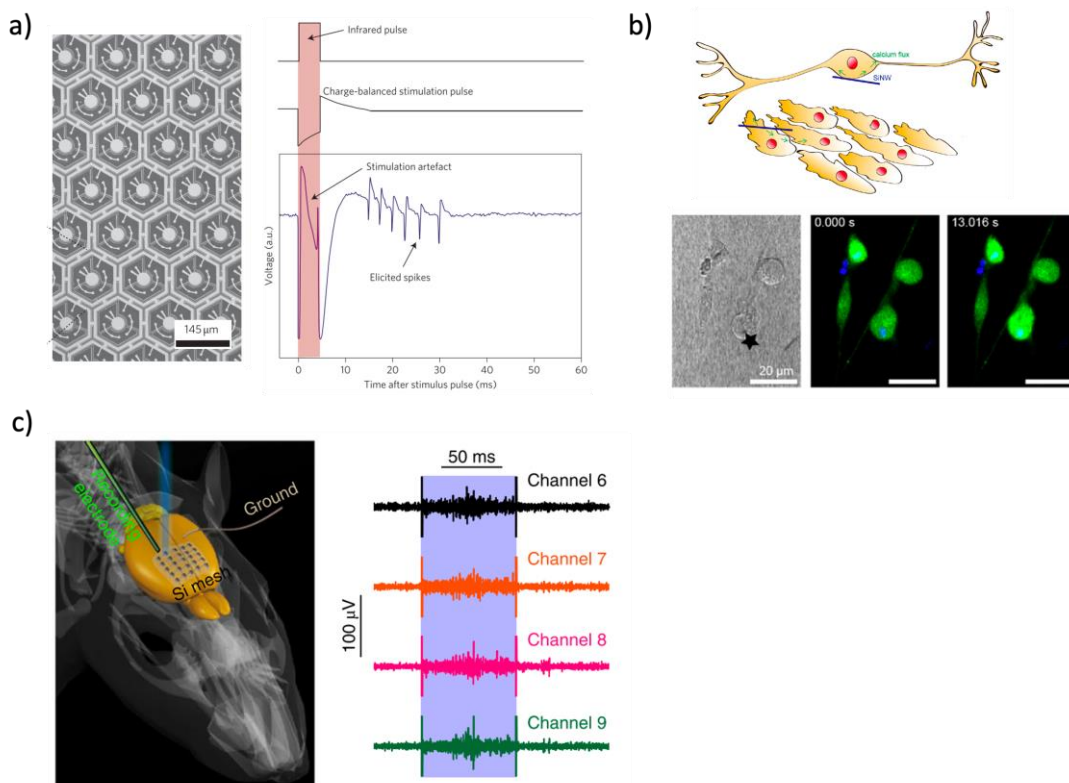
Figure 1.7. Wireless optical stimulation by Si-based devices. (a) Subretinal photodiode array (left), and infrared pulse and excited spikes of neurons (right) [57]. Figure obtained from Ref. 57. (b) Optical stimulation of cells by Si nanowires can elicit intracellular calcium wave propagation and subsequent intercellular propagation[65]. Figure obtained from Ref. 65. (c) Schematic of in vivo photo-stimulation test on a head-fixed anaesthetized mouse brain with silicon mesh(left), example traces of neural response in a single light stimulation marked by a light blue band (right)[66]. Figure obtained from Ref. 66.

In addition to the single cell level, Si-based devices can also be in tight contact with the biological organ by van der Waals forces and realize the optical stimulation at the organ level. Gold decorated p-i-n Si mesh on a holey PDMS membrane could be attached to the mouse brain cortex with sufficient adhesion, enable effective light-controlled modulation of mouse brain activity in vivo, triggering forelimb movements of the mouse, using visible light (473 nm, $1.3 \cdot 10^5$ μW/mm²). This optical modulation technique exploits the light-induced large photocurrent generated by the p-i-n Si diode junction, in which the Au-decorated surface was useful to further increase the capacitive and Faradaic currents (Fig. 1.7c)[66]. On the other hand, polymer-supported Si nanowires mesh allowed for optical stimulation of cultured cardiomyocytes by means of a focused green laser (514 nm, $3 \cdot 10^6$ μW/mm²) which was scanned along the sample, enabling the ex vivo heart stimulation beating at a higher frequency[67].

1.3.2. Optical stimulation by organic semiconductors

The biomedical application of organic semiconductor materials is related to their easier solution processability and mechanical compatibility with biological tissues, showing high stretchability and flexibility[68]. Light absorption in organic semiconductors results in excitons generation, rather than free electron-hole pairs. The excitons are confined in a tiny volume and they are not able to dissociate into free charges due to the large coulombic barrier in organic materials. To achieve efficient photocurrent generation, the organic semiconductor devices usually rely on a heterojunction between two different materials (electron-donor and electron-acceptor)[69,70].

As example, a photovoltaic device based on the organic blend poly (3-hexylthiophene-2, 5-diyl) (P3HT) and phenyl-C61-butyric-acid-methyl ester (PCBM) could trigger action potentials of neurons by short pulses of visible light (532 nm, 10^4 μW/mm²) with high temporal resolution and spatial selectivity. At the heterojunction, the PCBM and P3HT acted as electron acceptor and donor, respectively, thus ensuring high charge generation efficiency[71]. Ghezzi and collaborators used a single-component organic film of P3HT to replace the photoreceptor cell layer in a rat retinal explant, and demonstrated that the P3HT film was able to trigger neuronal action potentials upon light illumination (532 nm, $1.5 \cdot 10^4$ μW/mm²) and to restore light sensitivity of the rat retinal explant with photoreceptor cells degeneration. The effective charge dissociation in the P3HT film was ensured by the interface with the conductive indium tin oxide (ITO) film (Fig. 1.8a)

[72], in a similar manner as the P3HT/PCBM heterojunction[71]. The use of a single P3HT component may help to reduce material toxicity during light illumination, as fullerenes photo-excitation can produce reactive oxygen species (ROS)[73]. In addition, Maya-Vvetencourt et al. reported a fully organic subretinal prosthetic device composed of three layers (P3HT/ PEDOT: PSS/ silk), which was implanted in a rat eye (Fig. 1.8b). The photovoltaic retinal prosthesis was able to recover light sensitivity and visual acuity in the rat that persisted up to 6-10 months after surgery[74].
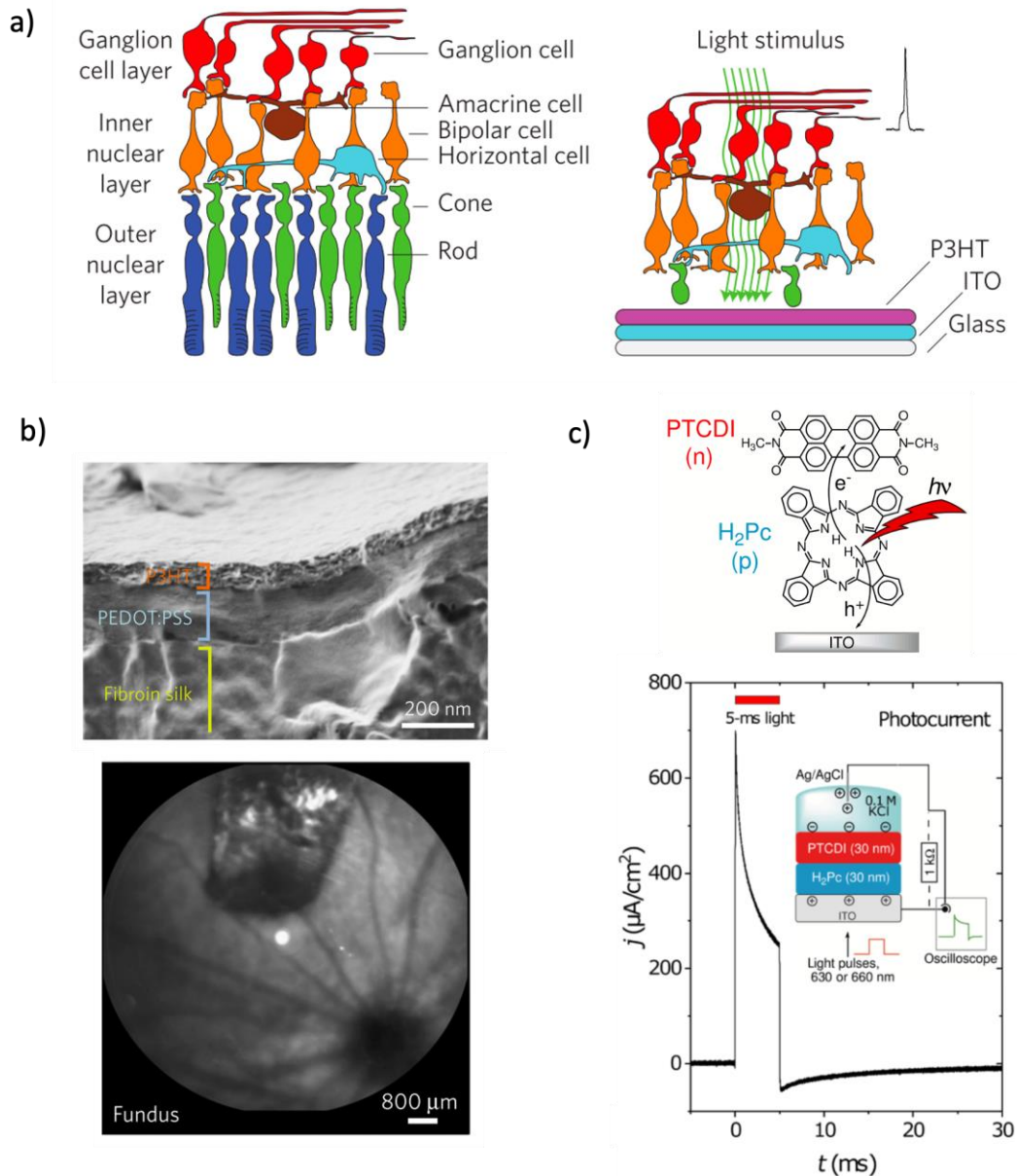
Figure 1.8. Organic semiconductor devices for wireless optical stimulation. (a) Schematic illustration of the retinal structure (left) and the degenerate retina with photoreceptor layer replaced by the organic polymer device[72]. Figure obtained from Ref. 72. (b) cross-section SEM image of the fully organic prosthetic device (top) and sample confocal scanning laser ophthalmoscopy image of the surgical prosthesis placement in the eye fundus of a dystrophic RCS rat (bottom)[74]. Figure obtained from Ref. 74. (c) The mechanism of OEPC devices rely on photoinduced charges transfer between H_2Pc (as electron donor) and PTCDI (as electron acceptor), the conducting ITO layer plays a role in storing positive charge and serving as the return electrode in solution [75]. Figure obtained from Ref. 75.

In addition, organic semiconductor materials such as H_2Pc (phthalocyanine) (p-type) and PTCDI (N, N'-demethyl-3,4,9,10-perrlenetetracarboxylic) (n-type) were also widely studied and showed excellent performance. Rand and co-workers reported a device comprising a thin trilayer of Cr/Au, H_2Pc and PTCDI, achieving effective photostimulation of neurons and light-insensitive embryonic chicken retinas, via a photocapacitive process. They used 660 nm light wavelength, which is at the edge of the first biological tissue transparency window, and pulsed light whose intensity and duration were 4800 $\mu W/mm^2$ and 5 ms, respectively[76,57]. The same group presented an optimized organic electrolytic photocapacitor (OEPC) device, consisting of a transparent conducting ITO layer with H_2Pc (p-type) layer as the electron donor and PTCDI (n-type) layer as the electron acceptor (Fig. 1.8c). They found that the OEPC with catalytically-active gold layer photochemically produced hydrogen peroxide as result of oxygen reduction on the PTCDI layer, while the ITO-based OEPC did not, thus yielding a truly photocapacitive actuation. They demonstrated that the OEPC device was able to effectively depolarize the cell membrane by measuring photo-induced opening of potassium channels, and change the membrane potential in the range of 20 to 110 mV on Xenopus *laevis* oocytes cells, using visible light of 660 nm wavelength with $6 \cdot 10^3$ $\mu W/mm^2$ intensity[75].

A major disadvantage of organic semiconductor materials is that their conductivity may deteriorate upon exposure to light due to light-induced chemical changes, as well as swelling or shrinkage caused by repeated charging and discharging processes[77, 69].

1.3.3. Optical stimulation by gold nanostructures

Gold nanomaterials are attractive for photothermal therapeutics due to their high biocompatibility, large surface to volume area, easy surface functionalization, and high absorption in the visible-near infrared (NIR) range based on the excitation of the localized surface plasmon resonances (LSPR)[78]. The LSPR occurs when Au nanostructures are stimulated by the electromagnetic field of an incident light beam, and results in the collective coherent oscillation of conduction electrons with respect to a positive metallic lattice, thus enhancing the light to heat generation efficiency of Au nanostructures. When the cells are attached with the Au nanostructures and under light illumination, the generated heat can induce local temperature increase at cell membrane

and change the membrane capacitance, leading to membrane depolarization and elicit the action potentials.

The main light absorbers of visible and infrared light in biological tissues are hemoglobin and water respectively. However, they have their lowest absorption coefficient in the near-infrared region around 650-900 nm, which is the region typically used in photothermal actuation to maximizing tissue penetration and avoiding thermal damage due to tissue absorption[79].

Eom and collaborators demonstrated the optical stimulation of rat sciatic nerve in vivo, based on photothermal effect of Au nanorods (Fig 1.9a), using a pulsed NIR light (980 nm, $1.56 \cdot 10^6$ µW/mm²)[80]. Similarly, Yong et al. presented a photothermal modulation strategy for cultured auditory neurons, by means of silica-coated gold nanorods as extrinsic absorbers and a pulsed NIR laser (780nm, $1.15 \cdot 10^7$ µW/mm²) at the LSPR wavelength[81].
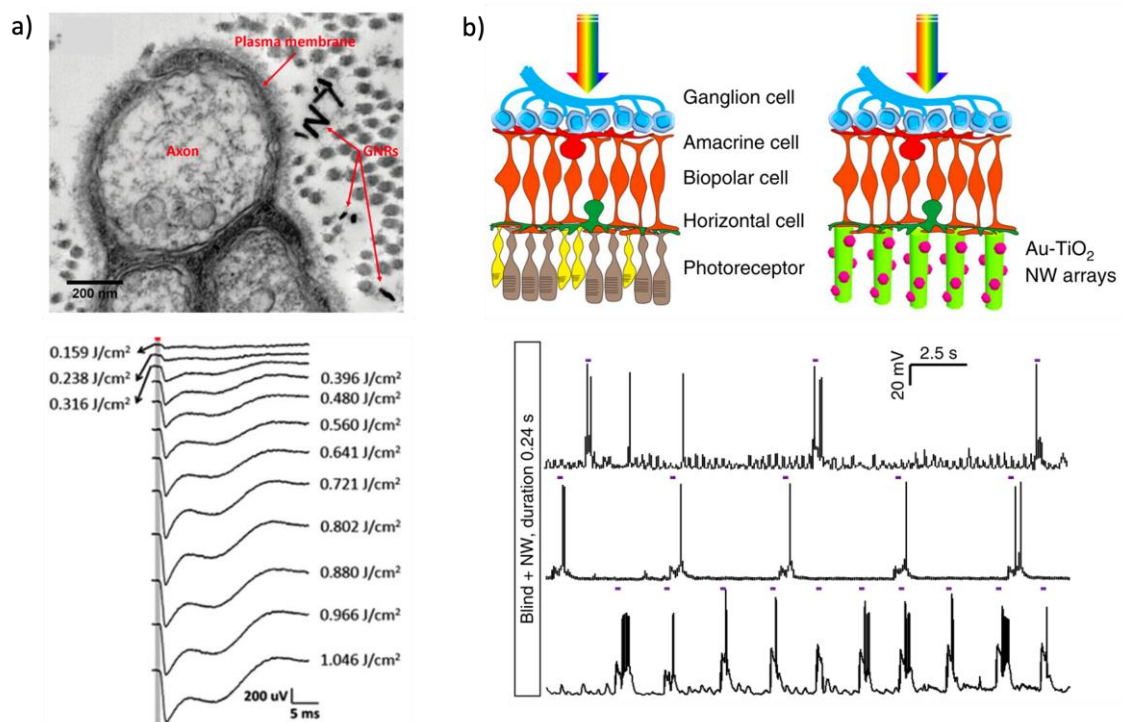
Figure 1.9. optical stimulation by Au nanomaterials. (a) TEM image of rat sciatic nerve with gold nanorods located near the plasma membrane (top); stimulated nerve action potentials recorded for 12 different laser powers (bottom)[80]. Figure obtained from Ref. 80. (b) Comparison of a retina and nanowire arrays interfaced blind retina that lacks photoreceptors(top); light responses to near UV light stimulation in NW arrays interfaced blind retina (bottom)[82]. Figure obtained from Ref. 82.

A significant drawback of free injected Au nanorods is their necessity to be extremely close to the selected cells in order to induce photothermal effect with the lowest delivered energy. However, most of the injected nanorods are often located around the cells rather than attached to them. Carvalho and co-workers reported a new photothermal approach with ligands-conjugated gold nanoparticles (Au NPs) targeting dorsal root ganglion (DRG) neurons, and green light millisecond pulses (532 nm, $3.1 \cdot 10^8$ μW/mm²). Interestingly, they proved that these Au NPs can be highly resistant to convective washout, which is very important for long term application[83]. Furthermore, Cardinal and colleagues showed the optical stimulation of hippocampal neurons via local activation of Ca^{2+} transients by means of plasmonic excitation of Au NPs targeted on neuronal membranes, using NIR light (800 nm, $2.7 \cdot 10^9$ μW/mm²)[84].

In addition to the photothermal effects, Au NPs can also be used in combination with semiconductor materials to enable more efficient photo absorption and charge separation, thus improving the generation of photocurrent or photovoltage upon light illumination through photovoltaic effects. For example, Tang et al. developed vertically oriented Au-TiO$_2$ nanowires arrays as artificial photoreceptors in retina (Fig. 1.9b), which triggered spiking activities in the retinal ganglion cells and restored green, blue, and near UV light responses with the spatial resolution approaching 50 μm. Moreover, they implanted the Au-TiO$_2$ NW arrays into blind mice with degenerated photoreceptors, and demonstrated the functional and behavioral restoration of the light sensitivity[82].

1.3.4. Optical stimulation by quantum dots

Quantum dots (QDs) are semiconductor nanocrystals with diameter of 2-10 nm whose optical and electronic properties change as a function of size, composition, and structure[85,86]. Under illumination they are able to emit light with various colors depending on their sizes, making them attractive for bioimaging and biosensing[87]. Besides, they can be implemented as light-harvesting sites for photovoltaic conversion and photocurrent generation due to the tunable absorption spectrum and high light extinction coefficients, which make them promising for opto-electric cell stimulation applications[88].

In this contexrt, Pappas and co-workers prepared thin films of semiconductor HgTe quantum dots produced by the layer by layer assembly on ITO substrate. Under laser illumination (532 nm, $8 \cdot 10^3$ μW/mm²), the photogenerated electrons in HgTe QDs were injected into the solution, inducing a photocurrent flow across the cell membrane. This resulted in the depolarization of cell membrane and the excitation of action potentials in neurons[56]. Besides, by integrating CdTe QDs films with prostate cancer cells or CdSe QD films with cortical neurons, the fields produced by the photogenerated dipoles from the QDs could perturb the cell membrane potential and activate the voltage-gated ion channels, thus generating action potentials and enabling the communication among cells[89].

However, QDs toxicity is crucial to establish a biocompatible photoactive QDs-cell interface. Toxic effects of QDs include apoptotic biochemical changes, increased concentrations of reactive oxygen species, suppressed metabolic activity and reduction in cell viability. Although some treatments like ZnS coating is demonstrated to be able to effectively reduce QD cytotoxicity, more investigation and other treatment methods are still needed, and potential safety risks for using QD should be under consideration[90,91].

1.3.5. Optical stimulation by graphene

Graphene, a two-dimensional single layer of carbon atoms densely packed into a benzene-ring structure, has many intriguing properties, including electrical conductivity, optoelectronic conversion of light into electricity, high surface area and biocompatibility[92,93], which make it promising for opto-electric cell stimulation.

Savchenko et al. demonstrated that graphene-based biointerface both in substrate or dispersible configurations could optically stimulate cardiomyocytes, and the efficiency of stimulation was independent of light wavelength. They also performed optical modulation (610nm, $1 \cdot 10^3$ μW/mm²) of the heart activity in zebrafish embryos in vivo using dispersible graphene biointerface[51]. Besides, Kim and co-workers presented a stretchable and transparent cell-sheet-graphene hybrid implanted on the hind limb muscle of mouse in vivo, for effectively optical activation (470 nm, 464 μW/mm²) of muscle cells[94].

1.3.6. Limitation of current optical stimulators

Taken together the optical stimulation devices described above, they have been versatile to stimulate excitable cells in vitro and in vivo, at targeted single cells or tissues. However, these optical stimulators usually require low penetration visible light and high light intensities (table 2), which limit their application to very superficial implants and might even cause tissue damage due to excessive thermal heating[95,96]. Moreover, the employed light intensities are much higher than the ocular safety limit for continuous exposure to visible light (for example, 107 μW/mm^2 at 532 nm)[61,72], thus hampering their application for retinal prosthesis. Besides, some nanostructured materials like the QDs may be internalized by cells, causing damage or malfunction of the cells. Therefore, there is still need to drastically increase the actuation efficiency of implantable devices in the NIR biological windows for achieving safe and maximized actuation in deeper tissues.

Table 2. Optical cell stimulation materials and employed light conditions

Materials	Wavelength (nm)	Intensity ($\mu W/mm^2$)	Stimulated cells or tissues	Refs
Lipid-supported mesoporous Si	532	$6.7 \cdot 10^7$	DRG neuron	[62]
Coaxial p-i-n Si	532	$8.6 \cdot 10^5$	DRG neuron	[60]
Au-decorated p-i-n Si	473	$1.3 \cdot 10^5$	Mouse brain in	[66]
Textured i-Si nanowires	592	$2.8 \cdot 10^6$	Neuron, glial	[65]
Supported p-i-n Si	514	$3 \cdot 10^6$	Cardiomyocyte	[67]
Si photodiode array	905	800	Rat retina	[57]
Si photodiode array	915	550	Rat retina in	[97]
Hybrid organic film rr-P3HT: PCBM	532	10^4	neuron	[71]
P3HT film	532	$1.5 \cdot 10^4$	Neuron	[72]
Metal/ H_2Pc/ PTCDI/ film	600	$4.8 \cdot 10^3$	neuron	[76]
PTCDI/ H_2Pc/ITO	660	$6 \cdot 10^3$	Xenopus laevis oocytes	[75]
Au nanorods	980	$1.59 \cdot 10^6$	neuron	[80]
Silica-coated Au	780	$1.15 \cdot 10^7$	neuron	[81]
Au nanoparticle (20 nm)	532	$3.1 \cdot 10^8$	DRG neuron	[83]
Au nanoparticle (100nm)	800	$2.7 \cdot 10^9$	neuron	[84]
Au nanoparticle	532	$8 \cdot 10^3$	cardiomyocyte	[98]
Au-decorated TiO_2 nanowires array	546	470	Blind rat retina	[82]

1.4. Wireless magnetic stimulation

Wireless magnetic stimulation can be induced in the tissue by externally controlled alternating magnetic field, which can penetrate through the tissues without attenuation[8,52]. The commonly used non-invasive brain stimulation methods based on direct magnetic stimulation is transcranial magnetic stimulation (TMS)[99]. Although non-invasive, the actuation devices have some drawbacks, such as poor spatial selectivity and high peak power consumption[8]. In TMS, high intensity magnetic fields are required for functional stimulation of deep brain regions. However, such a high intensity magnetic fields may stimulate cortical regions and facial nerves over the standard limit, which may lead to cervical muscle contraction, facial pain or other unexpected side effects[100]. Magneto-electric or magneto-thermal nanomaterials are promising alternative to solve these problems, as they are able to locally convert magnetic energy into electric energy or heat, to locally stimulate cells or tissues with nanoscale spatial resolution, molecular-level selectivity and remote controllability.

1.4.1. Magneto-electric stimulation

Remotely controlled magnetic fields can actuate on magneto-electric (ME) nanomaterials to induce local electric charge oscillations that can directly interact with cells for generating localized and targeted cell stimulation[101]. ME nanomaterials are generally made of multiferroic materials, i.e. materials that simultaneously show ferroelectricity and ferromagnetism. The magnetic to electric energy conversion in these materials exploits the properties from two different phases of the material, that combine the magnetostrictive property in the ferromagnetic phase with the piezoelectric property in the ferroelectric phase. Thus, when an external magnetic field is applied, the magnetostrictive stress generated in the ferromagnetic phase is transferred to the ferroelectric phase, which changes its polarization and the associated electric field due to the piezoelectric effect[102]. The schematic magnetic-elastic-electric couplings in multiferroic materials is shown in Fig. 1.10.
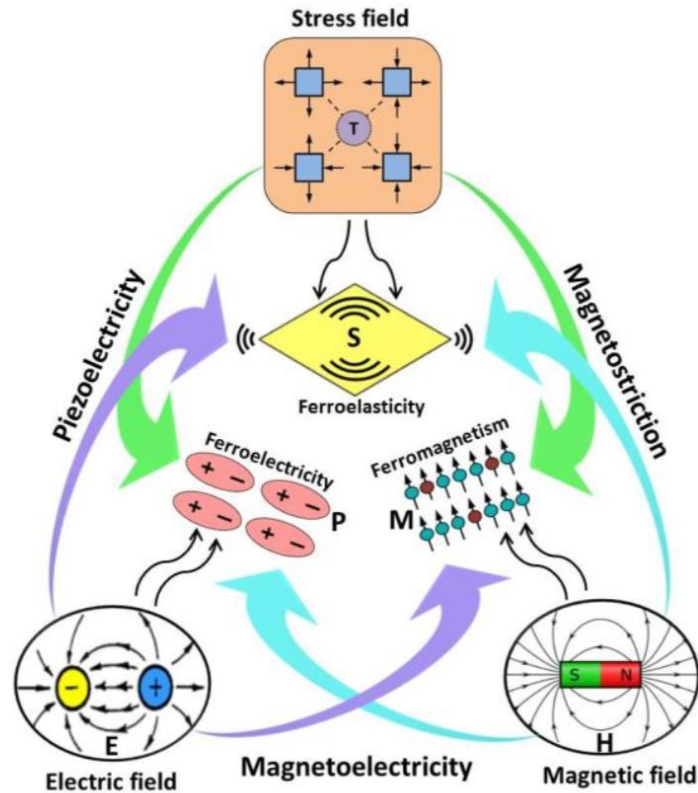
Figure 1.10. Schematic illustrating magnetic-elastic-electric couplings in multiferroic materials[103]. Here, M is magnetization, S is mechanical strain, P is dielectric polarization. Figure obtained from Ref. 103.

The multiferroic nanocomposites can be in different forms such as spherical core-shell nanoparticles with a magnetostrictive core and a piezoelectric shell, magnetostrictive rod with a piezoelectric coating, and composite spheres of piezoelectric ceramics with embedded magnetic nanoparticles[104] (Fig. 1.11). These structures are expected to exhibit excellent magnetoelectric performance due to: i) good mechanical contact at interface of the two ferroic phases (which is an issue for laminar composites bonded by gluing or pressing); ii) the magnetostrictive stress can be efficiently transferred to the piezoelectric phase due to the very thin piezoelectric shell; and iii) the absence of substrate clamping effect that restricts magnetostrictive strains in some film structures[104].
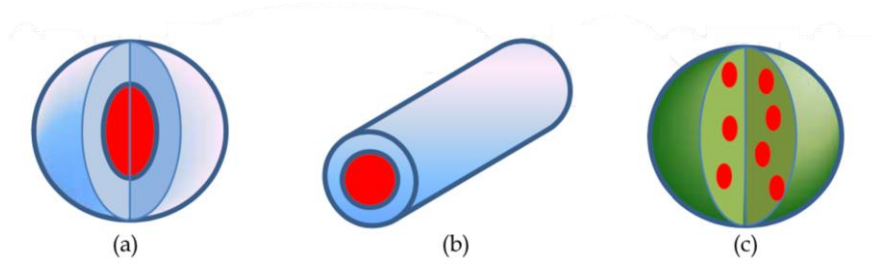
Figure 1.11. Three types of magnetoelectric nanomaterials structure. (a) spherical core-shell nanoparticles with a magnetostrictive core and piezoelectric shell, (b) magnetostrictive rod with a piezoelectric coating, (c) spheres of piezoelectric ceramics with embedded magnetic nanoparticles[104]. Figure obtained from Ref. 104.

The magnetic actuation is translated by ME composite nanoparticles (NPs) into a local electric field that induce a redistribution of charges at the surface, which is able to trigger biochemical processes[105,106]. If the ME NPs are placed near the cell membranes, the ion channels can open accordingly, thus leading to the membrane depolarization and generation of action potentials. By varying the conditions of the applied alternating magnetic field, such as strength and duration, a tight control over the ion channel gating can be achieved[104]. In addition, ME nanoparticles can be synthesized to be smaller than 20 nm in diameter, which is essential to penetrate the blood-brain barrier, to effectively and non-invasively penetrate into the brain[101].

The concept illustration of using ME nanoparticles for noninvasive electric stimulation of deep brain regions is shown in Fig. 1.12. Guduru and collaborators fabricated $CoFe_2O_4$-$BaTiO_3$ Core-shell ME NPs (30 nm). Approximately 10 μg of these ME NPs were injected in the blood stream through the tail vein of a mouse, and forced to cross the blood-brain barrier via a d.c. field gradient of 3000 Oe/cm. The ME NPs administered in the brain can generate local electric field upon exposure to an external magnetic field. Through a surgically attached two-channel electroencephalography (EEG) headmount, the in vivo test showed that the ME NPs could modulate the electric waveforms deep in the brain via an external 100 Oe a.c. magnetic field in a frequency of 0 - 20 Hz[52].
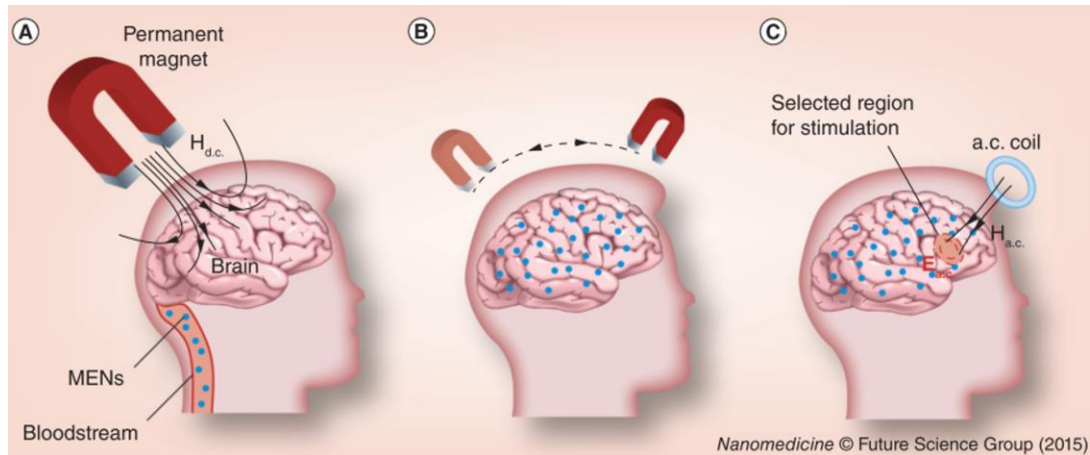
Figure 1.12.   Concept illustration of using ME NPs for noninvasive electric field stimulation of selected regions deep in the brain. (A) ME NPs are forced into the brain via application of a d.c. magnetic field gradient. (B) ME NPs are distributed over the brain via spatially varying d.c. magnetic field gradient. (C) Stimulation of selected regions deep in the brain[52]. Figure obtained from Ref. 52.

On the other hand, the typical neural stimulators that are used to treat many neurological disorder diseases usually operate safely and effectively in the high frequency "therapeutic band" between 100 and 200 Hz. Thus, Wickens and collabrators fabricated ME neural stimulators by boding a magnetostrictive layer (Metglas) to a piezoelectric layer polyvinydine fluoride (PVDF), which can convert a.c. magnetic fields into a voltage. The magnetically-powered enabled the stimulation of neurons in ex vivo brain slices, effective deep brain stimulation in a freely moving rat (Fig. 1.13), as well as operation in the therapeutic band (100-200 Hz). In addition, as the voltage produced by the film depended on the thickness of the piezoelectric layer rather than the film area, even smaller film could serve as effective stimulators[107].
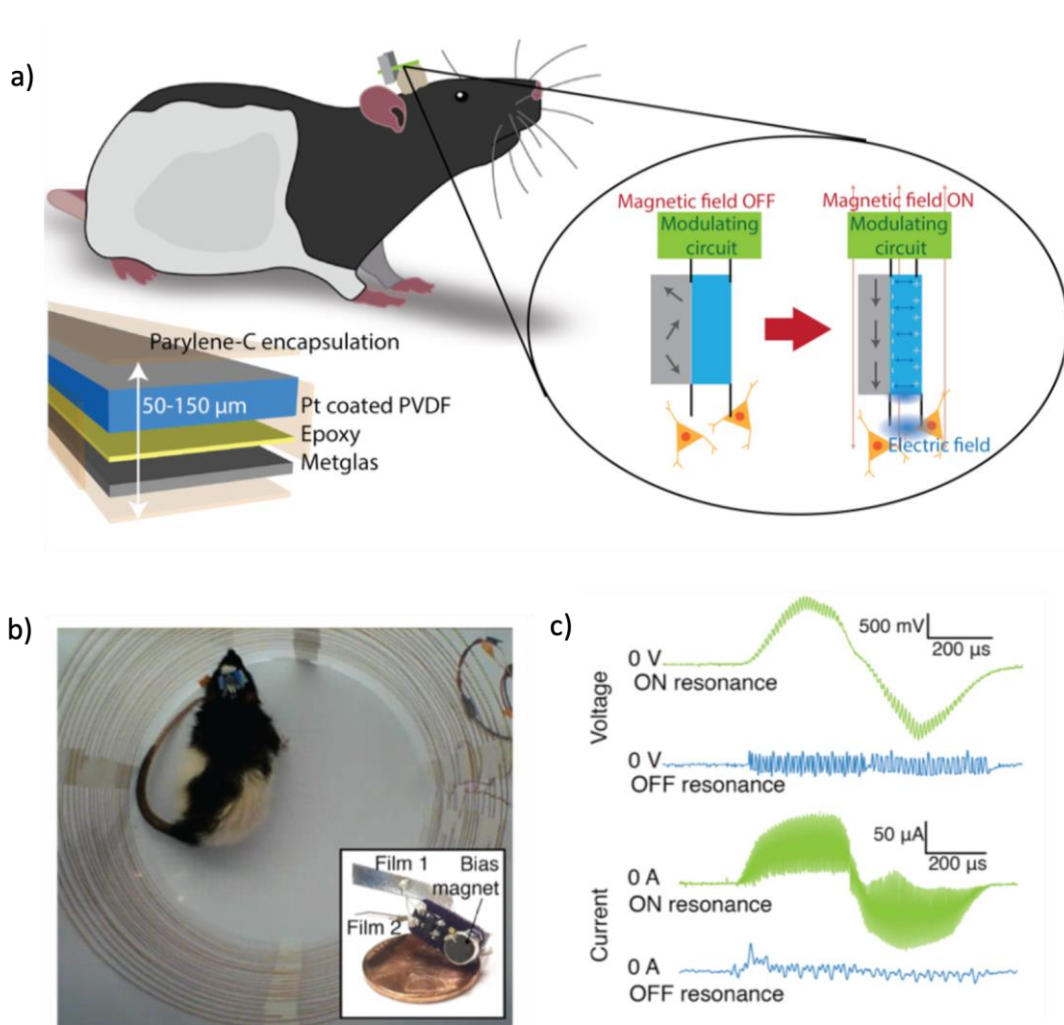
Figure 1.13. Magnetoelectric stimulator on a freely moving rat for deep brain stimulation. (a) Diagram of the ME stimulator. Insert shows the operating principle of the ME stimulator. (b) a rat implanted with ME stimulator in a circular enclosure wrapped with magnet wire. (c) Voltage generated by the ME device in rat brain and the current applied to the brain on/off resonance[107]. Figure obtained from Ref.107.

It is worth mentioning that polymer-based ME materials can be more suitable for bone tissue engineering, which typically requires lightweight, versatile, flexible and biocompatible biomaterials. Ribeiro and collaborators fabricated TD/P(VDF-TrFE) (Terfenol-D/ poly (vinylidene fluoride-co-trifluoroethylene)) composite film, in which Terfenol-D has high magnetostrictive coefficient and biocompatibility, and P(VDF-TrFE) shows high piezoelectric coefficient. They proved that the ME composites were able to provide mechanical (up to 110 ppm) and electrical stimuli (up to 0.115 mV) to

MC3T3-E1 pre-osteoblast cells cultured under dynamic magnetic stimulation (0 Oe - 230 Oe). The stimulation enhanced cell proliferation by 25%, which can be a promising approach for tissue engineering[108].

1.4.2. Magneto-thermal stimulation

Thermal modulation of cells activity can be achieved through the heating induced transmembrane capacitance change and the non-uniform conductance change of various ion channels[8]. Magnetic nanoparticles (MNPs) that can convert alternating magnetic field (AMF) energy into heat have received a great attention as a unique platform to achieve magnetothermal modulation of cellular activities.
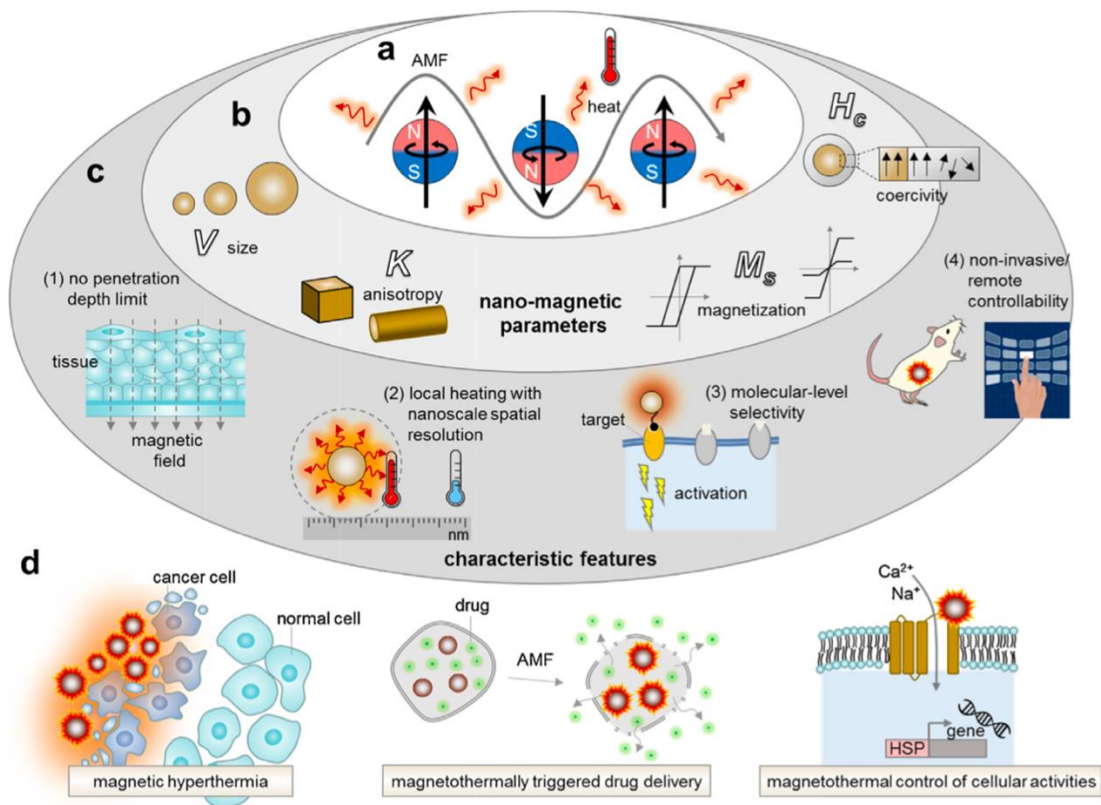
Figure 1.13. Magnetic heating as a versatile platform for biomedical applications. (a) MNPs as mediators to convert AMF energy into heat. (b) The magnetic heating efficiency can be tuned by the parameters including size, anisotropy, saturation magnetization, and coercivity. (c) characteristic features of magnetic heating. (d) Magnetic heating can be applied for magnetic hyperthermia, magneto-thermally triggered drug delivery, and magnetothermal control of cells activities[109]. Figure obtained from Ref. 109.

Fig. 1.13 illustrates the magnetic parameters that control the heating efficiency, the characteristics of magnetic heating, as well as its emerging biomedical applications[109]. The magnetic heating efficiency can be tuned by the parameters including particle size, anisotropy, saturation magnetization, and coercivity. Moreover, the magnetic heating through MNPs has many advantages like no penetration depth limit, nanoscale spatial resolution, and molecular-level selectivity.

The capsaicin receptor TRPV1 is a heat-sensitive ion channel that can be activated when temperature increases above 43°C[110]. Magnetic nanoparticles $MnFe_2O_4$ (d=6 nm) [111] and Fe_3O_4 (d=22 nm) [112] could both convert magnetic field into heat to activate the ion channels TRPV1 and cause an influx of calcium ions (Fig. 1.14), thereby eliciting action potentials in neurons. In particular, the Fe_3O_4 nanoparticles have been demonstrated to be effective for in vivo magnetothermal stimulation of neurons in the targeted deep brain region of mice[112].
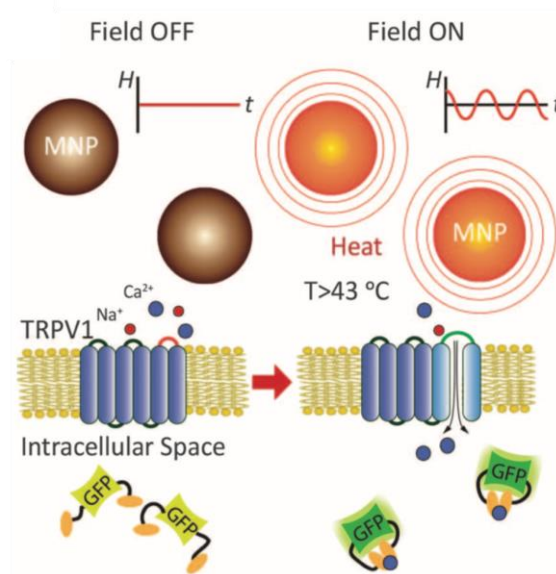

Figure 1.14. Magnetic nanoparticles heating induces opening of TRPV1 and influx of calcium ions. Figure obtained from Ref. 112.

In addition, activation of the temperature sensitive ion channel TRPV1 can stimulate synthesis and release of bioengineered insulin driven by a calcium-sensitive promoter.

Stanley et.al. used iron oxide nanoparticles binding to TRPV1 channels, which were heated in a radio-frequency magnetic field for stimulating insulin release and controlling glucose homeostasis in mice[113].

However, there are still several aspects to be optimized for magnetic cell stimulation by the nanomaterials, such as reduce stimulation latency, extend their residential lifetime at the cell interface, and target nanomaterials into specific locations[114].

1.5 Objectives

Given current limitations of the optical and magnetic cell stimulation methods, including the necessity of high light intensity and low penetration visible light, or the low spatial/temporal precision of the magnetic actuation, the aim of this thesis has been developing new nanomaterials that can be wirelessly controlled to electrically stimulate excitable cells with high spatiotemporal resolution, combining the cost-effective colloidal lithography techniques at the wafer scale.

In particular, two types of nanomaterials have been developed: 1) Si/Au nanostructures for wireless opto-electric actuation of excitable cells, with ultralow light intensity in the NIR biological window; 2) FeGa/ZnO nanoactuators on flexible elastomer for wireless magneto-opto-electric actuation of excitable cells. To progress towards these goals, the following specific objectives were defined:

i) Theoretical design of Si/Au nanostructure combined with p-n junctions, and optical analysis of their absorption efficiency by Finite-Difference Time-Domain (FDTD) simulations.

ii) Fabrication and opto-electric characterization and optimization of Si/Au nanostructured with high penetration NIR light.

iii) Demonstration of cells viability on the Si/Au nanostructured devices.

iv) Design, fabrication and magneto-opto-electric characterization of FeGa/ZnO nanoactuators on flexible elastomers.

v) Prove that FeGa/ZnO nanoactuators on flexible elastomer are not cytotoxic and do not disturb the cell viability.

vi)   The final objectives were the experimental demonstration in vitro of the optical and combined magnetic/optic stimulation of excitable cells with the Si/Au and FeGa/ZnO nanomaterials through patch-clamp experiments. However, the COVID lock-down impeded carrying out these final experiments and including them in the Thesis manuscript.

In the following parts of the Thesis manuscript, we first introduce the experimental materials and methods used in this work in Chapter 2. In particular, it includes the detailed description of the nanofabrication of opto-electric and magneto-opto-electric nanomaterials with tunable lengths, shapes and densities at the wafer scale.

Then in Chapter 3 we present the work related to the Si/Au nanostructures for opto-electric stimulation in the near infrared biological window with ultralow light intensities.

In Chapter 4 we show novel FeGa/ZnO nanostructures for the generation of electrical actuation under optical and magnetic signals simultaneously, with the aim of improving the wireless actuation versatility and strength.

Finally, the main conclusions of this Thesis are discussed in Chapter 5, and some perspectives for future work are presented in Chapter 6.

2 Experimental materials and methods

Abstract:

In this chapter we first describe the method for theoretical absorption analysis of Si/Au nanostructures through Finite-Difference Time-Domain (FDTD) stimulation, following by the description of nanofabrication process of Si/Au nanostructures, which presents the result of each step. We fabricated Si/Au nanopillars with tunable lengths, diameters and densities at the wafer scale through the cost-effective colloidal lithography techniques. Next, we present the nanofabrication process of FeGa/ZnO nanodomes integrated in PDMS film.

Then, the main analysis methods are introduced, including scanning electron microscopy, opto-electric test system for Si/Au nanostructures, vibrating sample magnetometer for testing magnetic properties of FeGa/ZnO nanodomes, and photothermal efficiency evaluation method for FeGa/ZnO nanodomes.

Finally, to prove the biocompatibility of the Si/Au and FeGa/ZnO nanostructures, we present the cell culture protocols and cell viability assay procedures. In particular, we used HEK 293 cells for Si/Au nanostructures, tested cell morphology cultured on Si/Au nanostructures by SEM, evaluated cell viability by cell tracker assay and cell proliferation assay. On the other hand, we used Osteosarcoma Saos-2 cells for FeGa/ZnO nanostructures, and checked the biocompatibility by SEM and cell tracker assay.

2.1   FDTD stimulation of the Si/Au nanostructures

Finite-Difference Time-Domain (FDTD) is a numerical analysis technique used for modelling computational electrodynamics, which solves Maxwell's equations in the time domain using finite-difference approximations[115]. We used FDTD stimulation (Lumerical software) to compare absorption spectrums of various Si/Au nanostructures, for the design, analysis and optimization of Si/Au nanostructures.

Firstly, to maximize the light trapping efficiency, we performed FDTD stimulation for the following system: i) the plain Si wafer, ii) Au nanodiscs (diameter D=230 nm, thickness T=50 nm) on Si wafer, iii) short Si nanopillar (length L=350 nm, D=230 nm), iv) short Si nanopillar with Au disc (L=350nm, D=230 nm), v) long Si nanopillar with Au disc (L=800nm, D=230 nm). To model the response of an array of nanostructures we used periodic boundary conditions with a cross section area of 500 nm x 500 nm, as illustrated in Fig. 2.1. We employed an incident broadband plane wave (650 nm to 2200 nm) incident on the array of nanostructures and we assumed that the incident medium is water (refractive index n_i = 1.33). A fine mesh of 2 nm was employed around the Au nanostructures to ensure the accuracy of the calculations. In these models we used two power monitors to calculate the reflected (R) light by the structures and transmitted (T) light through a plane located 1 μm inside the Si substrate. Therefore, the absorbed light in the first micron of sample is calculated as A = 1-T-R. We also incorporate a monitor to extract the electromagnetic field distribution inside and around the nanostructures. In particular we focus on the electric field in the direction of the plane wave polarization, i.e. E_x.
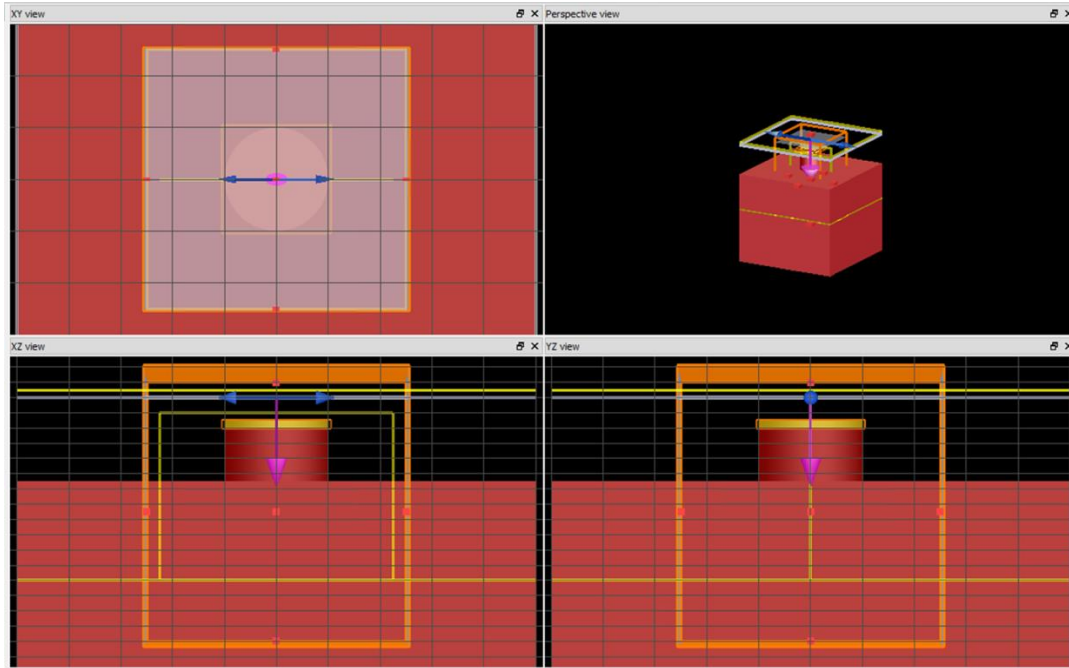
Figure 2.1. Three dimensional views (XY view, XZ view, YZ view) of FDTD stimulation for short Si/Au nanopillar.

To model the effect of nanopillar diameter, we tuned the diameters from 200 nm to 350 nm, for the short Si/Au nanopillar (L=350nm). In addition, to model the effect of the nanostructures density we varied the periodicity of the structures from 500 nm to 300 nm, also for the short Si/Au nanopillar (L=350nm, D=230 nm).

2.2   Fabrication of the Si/Au nanostructured system

Based on the theoretical analysis, and in order to fully understand and maximize the opto-electric response of the Si/Au nanostructures, we fabricated different Si/Au nanostructured surfaces on Si wafer with p-n junction (p-n Si), including: Au nanodiscs, and Si/Au nanopillars with different lengths and densities. We employed a cost-effective, scalable and highly tunable process based on colloidal lithography nanofabrication.

The fabrication process of Si/Au nanopillars mainly includes the following 5 steps, as illustrated in Fig. 2.2:

Step 1 (Figure 2.2a): n-dopant implantation on a 4-inch p-type silicon wafer, up to a depth of 560 nm ± 10 nm, to form the p-n junction.

Step 2 (Figure 2.2b): deposition of Ti/Au films of 1 nm/75 nm thick by Electron Beam Evaporation.

Step 3 (Figure 2.2c): colloidal self-assembly of polystyrene nanospheres on the Au surface, leading to a randomly ordered but homogeneous, or hexagonal closed-packed distributions of colloids on the whole wafer.

Step 4 (Figure 2.2d): Au discs production by inductively coupled plasma - reactive ion etching (ICP- RIE) with argon (Ar) gas, using the nanospheres as masks.

Step 5 (Figure 2.2e): Si/Au nanopillars fabrication by deep reactive ion etching (DRIE) via Bosch process, using Au discs as masks. The Bosch process alternates repeatedly between an isotropic etching with SF_6 gas and creation of a passivation layer by C_4F_8 gas. It is very important to fine tune the time of the etching and passivation steps to obtain Si/Au nanopillars with vertical side-walls.
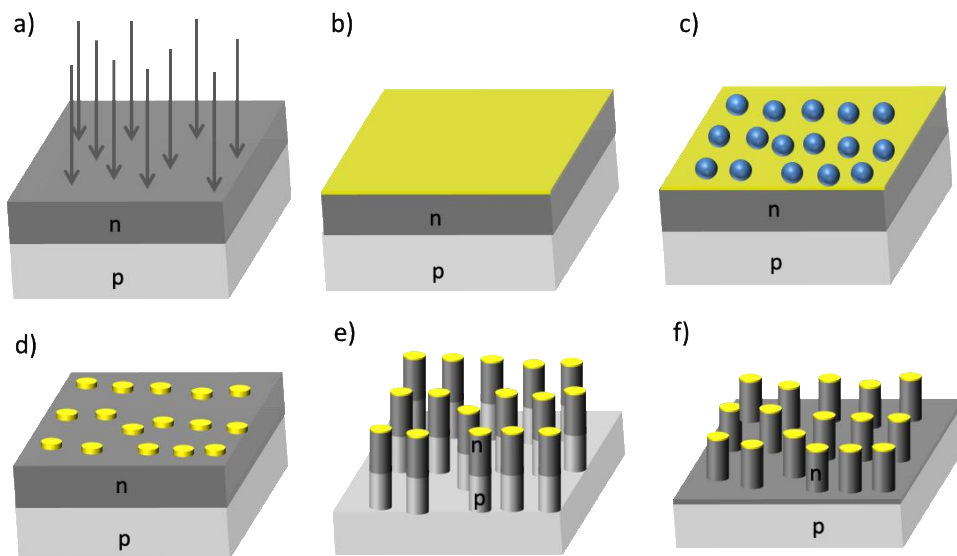

Figure 2.2. Schematic fabrication process of Si/Au nanostructures. (a) n-doping on p-type Si wafer. (b) Au film deposition. (c) colloidal self-assembly of nanospheres. (d) ICP-RIE to define Au discs. (e) Bosch process to produce long Si/Au nanopillars. (f) Bosch process to produce short Si/Au nanopillars.

2.2.1 Ion implantation to form p-n junction in Si wafer

Ion implantation is a low temperature process in which ions of one element are accelerated by an electrical field into a solid target. If the ions differ in composition from the target, they will alter the elemental composition of the target and possibly change the chemical, physical or electrical properties of the target[116]. Ion implantation was established as a technique for producing the p-n junction of photovoltaic devices in the early 1980s. When implanted into the silicon, the p-type dopant boron atoms can create an excess of holes, and the n-type phosphorus dopant atoms can generate the excess of electrons.

We used the Ion Implanter IBS IMC 210RD to introduce phosphorus dopants into a 4-inch p-type silicon wafer. The ion implantation was performed with the implanted dose of $4 \cdot 10^{15}$ ions/ cm^2 and energy of 50 KeV, followed by annealing at 950 °C for 10 minutes in Annealsys ASMaster-2000 RTCVD furnace.

2.2.2 Electron beam evaporation

Electron beam evaporation is a physical vapor deposition (PVD) technique in which the target material is bombarded with an intense electron beam from a filament, and vaporize the material for deposition on the substrate in a high vacuum environment. The E-beam evaporation technique has several advantages. Firstly, it permits the direct transfer of electron beam energy to the target evaporated material, leading to the formation of higher density films with increased adhesion to the substrate. Secondly, several thin films from different target materials with the highest purity can be obtained by using a multiple crucible E-beam evaporator without breaking the vacuum, thus avoiding interlayer contamination.

In our case, a titanium/ gold layer of 1nm/ 75nm was deposited on the Si wafer by electron beam evaporation (model: ATC-8E Orion, AJA International Inc.). We used 10 kV HV source (Telemark). The deposition rates of Ti and Au were 0.05 nm and 0.2 nm per second separately. The vacuum range of the cryopumped main chamber was up to $1 \cdot 10^{-8}$ mbar, and the turbopumped loadlock chamber was around to $2 \cdot 10^{-6}$ mbar.

2.2.3 Colloidal self-assembly

Colloidal lithography is an unconventional lithographic technique for patterning and fabrication of various nanostructures on planar substrates and non-planar substrates. It allows low cost, fast, large patterning area, and a broad choice of microspheres sizes. The microspheres can self-assemble into two-dimensional extended periodic arrays, short-range ordered distribution, to be used as masks for etching and deposition. Many different micro/ nanostructures such as pillars, cones, rings, and holes have been developed by colloidal lithography[117].

Hexagonal closed packed nanospheres

To achieve periodic colloidal self-assembly nanospheres on Au coated silicon wafers we first self-assembled a monolayer of colloids at a water/air interface, as illustrated in Fig. 2.3. The carboxylate modified latex beads (4% w/v), of 300 nm in diameter (or D500 nm nanospheres for fabrication of D350 nm nanopillars) were purchased from Thermo Fisher scientific. The as-received polystyrene nanospheres were diluted by ethanol at a ratio of 1:1. The mixture was sonicated for 5 minutes, and then it was continuously injected onto the water/air interface through a precisely controlled syringe pump system at a rate of 4 µL/min. The needle tip was positioned to exactly contact the water surface.
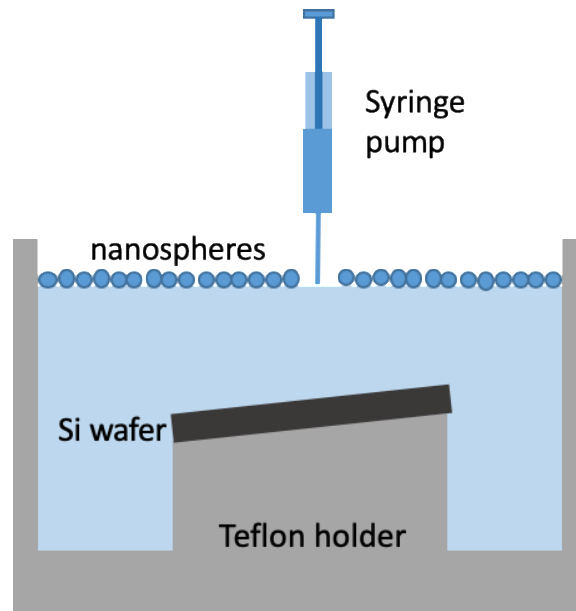

Figure 2.3 Schematic illustration of the formation of close packed nanospheres on water surface.

When the hexagonal close packed monolayer was formed on the whole water surface, the water was drained from the bottom of the Teflon bath and ultimately the nanospheres monolayer was transferred onto the silicon wafer underneath. One SEM image of the close packed nanospheres is shown in Fig. 2.4.
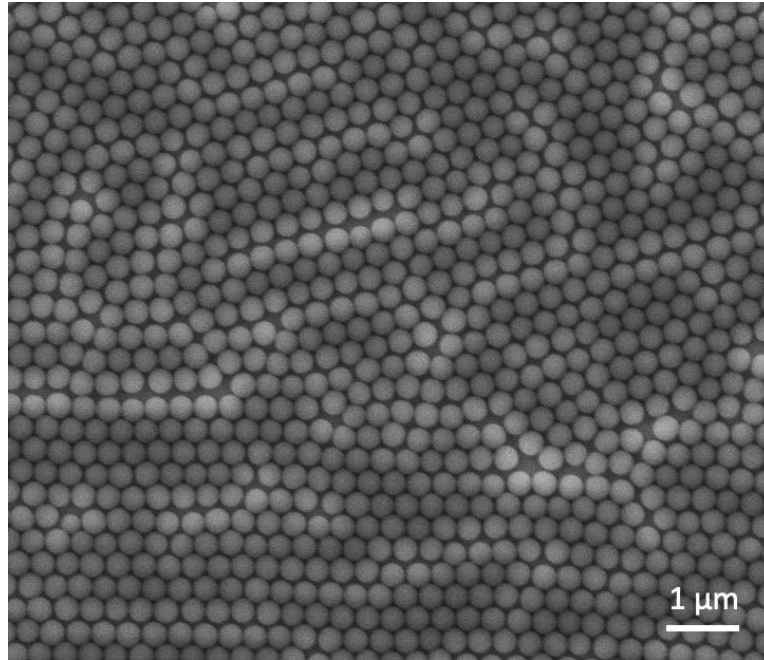

Figure 2.4. SEM image of the close packed nanospheres of 300 nm in diameter.

Separated nanospheres by electrostatic colloidal self-assembly

The electrostatic colloidal self-assembly method permits the attachment of charged particles from dilute aqueous solutions onto oppositely charged substrates. The driving force is primarily due to the electrostatic attraction with the substrate and repulsion between spheres[118]. The process is much easier and faster than the hexagonal close-packed self-assembly, as illustrated in Fig. 2.5.
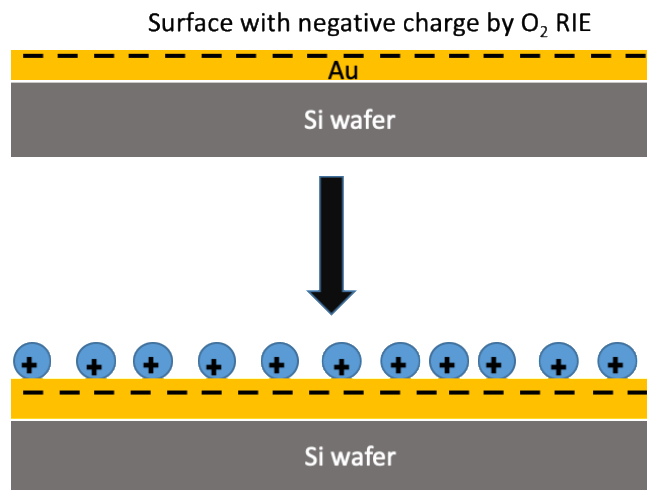
Surface with negative charge by O_2 RIE

Figure 2.5 Schematic illustration of the electrostatic colloidal self-assembly

Firstly, the silicon wafer with Au film was treated by O_2 RIE for 2 minutes, to remove surface contaminants and activate surface by introducing negative surface charges. Then the positively charged Amidine latex beads (Thermo Fisher Scientific, 4% w/v, diameter 200 nm) was diluted to 0.1% w/v in Milli-Q water, sonicated for 5 minutes, and dropped on the wafer surface. After 5 minutes, the wafer was rinsed with Milli-Q water to remove extra nanoparticles and blown dry by N_2 gas. The process results in a randomly ordered but homogeneous distribution of nanospheres on the whole wafer. One SEM image of the separated nanospheres is shown in Fig. 2.6.
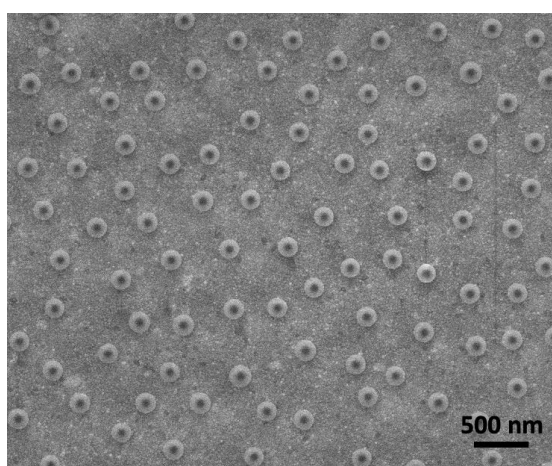

Figure 2.6 SEM image of separated nanospheres of 200 nm in diameter

2.2.4 Inductively coupled plasma - reactive ion etching

Inductively coupled plasma -reactive ion etching (ICP-RIE) is an anisotropic dry-etching process during which material can be removed by the chemically reactive plasma under a low pressure (1- 100 mTorr). The ICP-RIE can be used for rapid etching of a wide range of materials including semiconductors, dielectrics, metals, and polymers. The etching conditions can be adjusted and optimized by tuning the process parameters such as radio frequency (RF) power, pressure, and gas flows. ICP-RIE is a popular dry-etching technique because of its possibility for high etch rates, great selectivity and reduced ion bombardment damage.

We used the ICP-RIE machine (Oxford Instruments, model: PlasmaPro Cobra 100) for two different etching processes: i) O_2 RIE to reduce the size of polystyrene nanospheres, and ii) Ar RIE to produce Au nanodiscs using the nanospheres as masks.

Through the O_2 RIE we could reduce the size of the close packed nanospheres from a diameter of 300 nm to around 220 nm, by using HF power of 100W, pressure of 80 mTorr, gas flow of 30 sccm (standard cubic centimeters per minute), and a duration of 25 seconds. One SEM image of the close packed nanospheres after O_2 RIE is shown in figure 2.7.
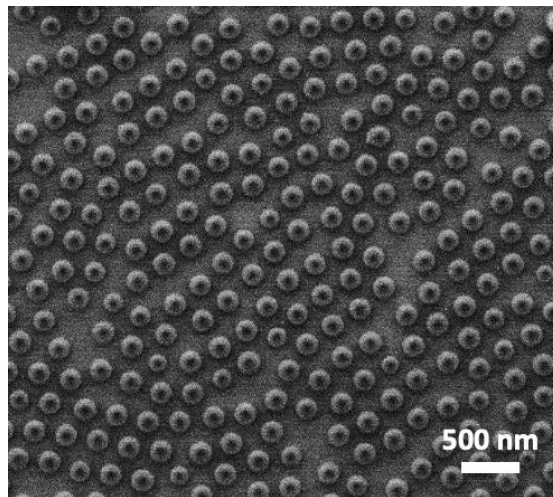

Figure 2.7. SEM image of the close packed nanospheres D300 nm after O_2 RIE

By Ar ICP-RIE we could remove the Au film deposited on Si wafer, using nanospheres as masks to produce the Au nanodiscs. We employed HF power of 40 W, ICP power of 1000W, pressure of 8 mTorr, gas flow of 20 sccm and duration of 2.5 minutes. An SEM image of the close packed Au nanodics obtained by O_2 and Ar RIE is shown in Fig. 2.8.
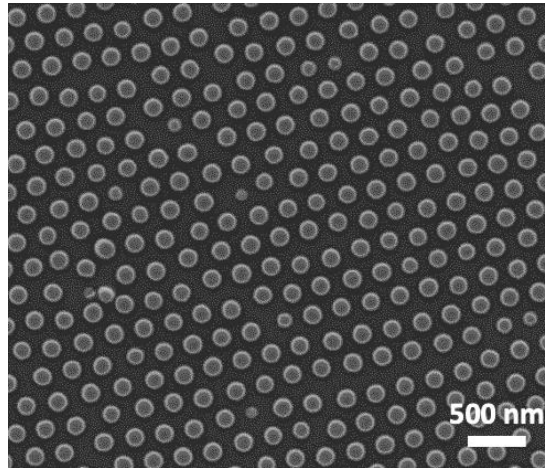

Figure 2.8. SEM image of the close packed Au nanodics obtained by O_2 and Ar RIE

In order to produce the Si nanopillars, we used the instrument ALCATEL AMS 110 DE for generating deep reactive ion etching (DRIE). Deep reactive-ion etching is a highly anisotropic etching process used to create deep, steep-sided holes and trenches in wafers, typically with high aspect ratios. One of the main technologies of high rate DRIE for deep-vertical etching of silicon is Bosch process.

The Bosch process alternates repeatedly between two etching and passivation modes to achieve nearly vertical structures. The etching step is a standard isotropic plasma etch with sulfur hexafluoride (SF_6) ions, which attack the Si wafer quite isotropically. The second step creates a passivation layer by octafluorocyclobutane (C_4F_8) source gas. The passivation layer protects the vertical side walls from chemical attack and prevents further etching. During the next etching process, the directional ions will attack the passivation layer at the bottom of the trench, but not along the sides, thus exposing only the bottom substrate to the chemical etchant. These etching/passivation steps are

repeated several times, thereby resulting in etching steps taking place only at the bottom of the etched pits and leading to deep vertical structures.

In our case, the conditions for Bosch process were: source power 500W, RF power 30W, SF_6 gas flow 150 sccm with step time 1.1 seconds, C_4F_8 gas flow 100 sccm with step time 3.5 seconds. An etching duration of 6 minutes using the Au discs as masks enabled obtaining Si/Au nanopillars with around 230 nm in diameter and 1 μm in length. Typical HR-SEM images of the Si/Au nanopillars are shown in Fig. 2.9.
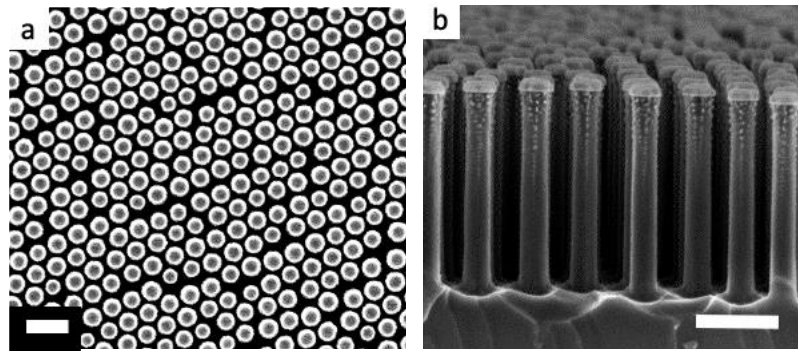
Figure 2.9. HR-SEM images of the Si/Au nanopillars. (a) top-view, (b) sectional view. Scale bar: 500 nm.

The lengths of the Si/Au nanopillars can be tuned by varying the Bosch process conditions. For example, using SF_6 for 1.1s, C_4F_8 for 3.5s, duration 2 mins we could fabricate Si/Au nanopillars with length (L) of 350 nm. Changing the parameters to SF_6 for 1.1s, C_4F_8 for 4 s, duration 7 mins and SF_6 for 1.1s, C_4F_8 for 10s, duration 18 mins, lead to lengths of 1 μm and 2 μm, respectively. In all the cases the diameter (D) was kept approximately constant around 230 nm (Fig. 2.10).

Figure 2.10. Tunable lengths of Si/Au nanopillars. (a) D ≈ 230nm, L ≈ 350 nm; (b) D ≈ 230nm, L ≈ 1 μm; (c) D ≈ 230nm, L ≈ 2 μm. Scale bar: 500 nm.

2.2.5 Tunable densities of Si/Au nanopillars

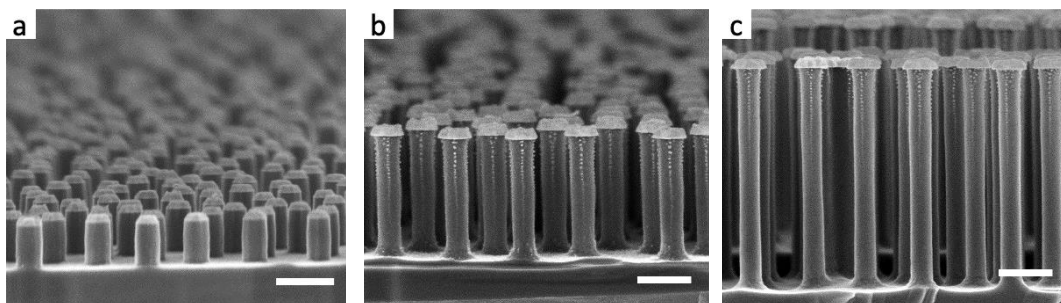By controlling the concentration of nanospheres in the electrostatic colloidal self-assembly from 0.005%, 0.02% to 0.1% w/v (Fig. 2.11 a, b, c, respectively), we could produce Si/Au nanopillars with different densities, while keeping the same diameter of around 230 nm and lengths of around 1 µm.
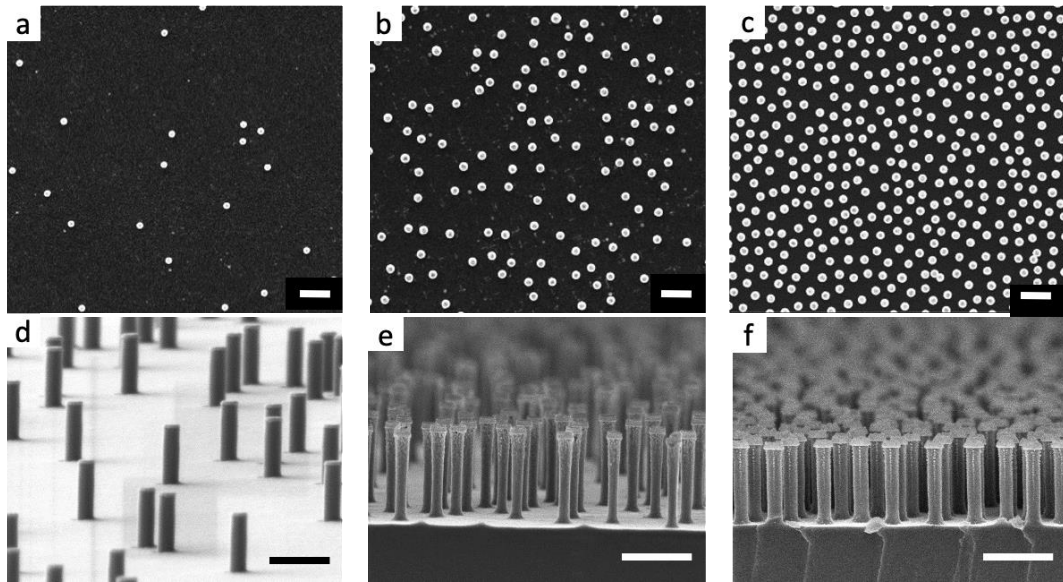
Figure 2.11. Tunable densities of Si/Au nanopillars. (a) (b) (c) SEM images from top view, (d) (e) (f) HR-SEM images from sectional view. Scale bar: 1 μm.

2.3   Fabrication of the FeGa/ZnO nanodomes

In order to fabricate the arrays of FeGa/ZnO nanodomes integrated in a flexible and biocompatible PMDS films in a cost-effective and scalable manner, we employed the colloidal self-assembled monolayers as transferrable supports, combined with sputtering deposition to deposit the FeGa/ZnO layers and SF_6 RIE to liberate these layers (Fig. 2.14).
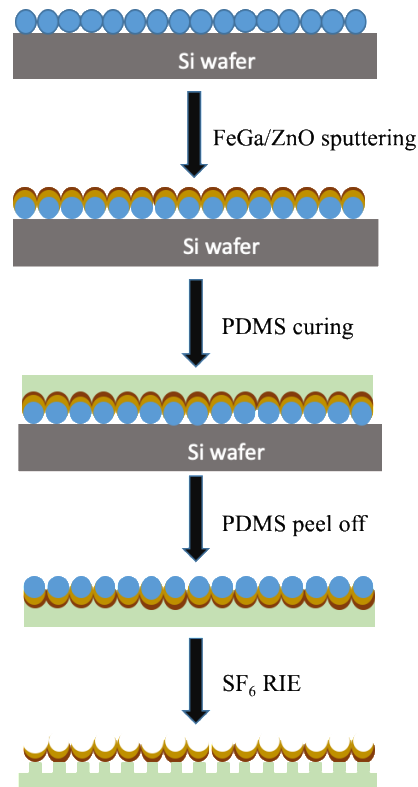
Figure 2.14. Schematic illustration of fabrication process of FeGa/ZnO nanodomes integrated in PDMS film.

This fabrication process started with colloidal self-assembly of carboxylate modified latex beads (4% w/v, 400 nm in diameter) on a 4-inch silicon wafer for preparing close packed arrays of nanospheres as previously described. The silicon wafer was pre-treated by oxygen plasma using PVA Tepla PS-210 microwave plasma etcher for 5 minutes at power of 400W, to remove surface contaminants and to leave a very hydrophilic surface.

On the other hand, to prepare the isolated FeGa/ZnO nanodomes, we used O_2 RIE for 25 seconds (HF power 100W, pressure 80 mTorr, gas flow 30 sccm) to reduce the size of nanospheres to around 320 nm.

The second step was sputtering the FeGa (40 nm) and ZnO (20 nm) layers on the close packed nanospheres. The FeGa and ZnO coatings were deposited by magnetron sputtering using an ATC Orion 5 from AJA International equipment (N. Scituate, MA, USA). Magnetron sputtering is a plasma-based coating method where positively charged energetic ions from a magnetically confined plasma collide with a negatively

46

charged target material. The sputtered atoms from the target are then deposited onto a substrate[119]. We used magnetron sputtering for deposition of FeGa/ZnO layers because reactive O_2 atmosphere is necessary for ZnO deposition, while it is not available by E-beam evaporation at ICN2. Firstly, FeGa was sputtered using an individual Fe80Ga20 (at %) target at 150W DC to achieve a final thickness of 40 nm. Then, ZnO was sputtered from a Zn target at 100 W DC up to a final thickness of 20 nm under reactive O_2 atmosphere.

The third step consisted on pouring liquid PDMS elastomer film of 1 mm in thickness on the wafer with nanospheres covered with FeGa/ZnO layers, and curing for its solidification. The SYLGARD 184 silicone elastomer kit was used as received. First, the liquid silicone and the curing agent were mixed with ratio of 10:1. The mixture was then poured to cover the whole patterned wafer. The bubbles inside the elastomer were removed in low vacuum for half an hour. Then the sample was put on a hot plate for one hour at temperature of 60 degree to fully cure the polymer. Finally, the PDMS film was peeled off from the silicon wafer, thus transferring the nanospheres with FeGa/ZnO inside the PDMS film.

The fourth step consisted on removing the polystyrene nanospheres to free the FeGa/ZnO layers by SF_6 RIE, using HF power 30 W, ICP power 1000W, pressure 12 mTorr, SF_6 gas flow 40 sccm, and a duration of 2.5 minutes.

Since the PDMS film is insulating, for checking scanning electron microscopy (SEM) clearly, the samples were firstly sputtered with a platinum (Pt) layer of 5 nm thickness by a high vacuum sputter coater Leica EM ACE600, to improve the surface conductivity.

In addition, in order to optimize the nanostructure for the maximum magnetization of FeGa layer, we fabricated ZnO/FeGa/ZnO (20nm/ 40nm/ 20nm) nanodomes with different diameters and densities, including D200 nm separated nanodomes, D400 nm separated nanodomes, D400 nm patterned nanodomes, and D500 nm patterned nanodomes. The separated nanospheres were prepared with electrostatic colloidal self-assembly, and the patterned nanospheres were prepared with hexagonal close-packed self-assembly.

2.4 Characterization techniques

2.4.1 Scanning electron microscopy

We used the scanning electron microscopy (SEM) with energy-dispersive x-ray spectroscopy (EDX) to perform morphological analysis and to make sure that the Au films were totally removed in the etching processes. In the SEM, the sample is scanned with a focused beam of electrons, the incident electrons interact with the atoms in the sample and emit secondary electrons that contain information about the topography of the sample, generating an image of the surface.

Energy-dispersive x-ray spectroscopy (EDX) is a surface analytical technique used for the elemental analysis of a sample. It applies electron beam to excite the atoms on the surface, then detects and analyzes the specific X-ray emissions from different atoms. The X-ray emissions of various atoms are different depending on the atomic structure of the elements.

The SEM images have been obtained using FEI Quanta 650F ESEM, with the Oxford Instruments Ultim Extreme EDX detector system integrated on it, operating at 20 kV. Through this instrument, we can get the SEM images from top view, and analyse the elements information of the sample. At the same time, we use the FEI Magellan 400L XRSEM to take high resolution SEM images from cross section view.

2.4.2 Opto-electric tests for Si/Au nanostructures

We tested the light induced photocurrents and photovoltages generated by Si/Au nanostructured system under continuous, pulsed and sinusoidal laser signals with 808 nm wavelength. The different samples included: Si wafer with p-n junction (Si p-n), Au discs on Si p-n wafer, Si/Au nanopillars with two different lengths, and short Si/Au nanopillars with different densities. The samples were pre-treated by several steps before being mounted on a homemade holder for opto-electric tests. Firstly, we employed SF_6 RIE for 30 seconds to remove the silica layer on the wafer backside by using the following conditions: pressure 6 mTorr, gas flow 40 sccm, ICP power 500W, HF power 30W. Then, Ti of 1 nm and Au of 50 nm were deposited on the backside with the edges covered by kapton tape to avoid Au deposition at the wafer edges.

We tested the light induced photovoltages and photocurrents by pulsed laser illumination, as well as photocurrents and photovoltages versus frequency with

sinusoidal laser illumination. Through a homemade LabView program, we could synchronize the laser signal and data acquisition. The testing system is illustrated in figure 2.13. The waveform generator (SIGLENT SDG1025) was connected to the computer to be manipulated by the LabView software, and was used to control the laser signal. The laser controller (THORLABS, ITC4005) was used for tuning the laser intensity by varying the driving currents through the signal generator. A photodiode amplifier (THORLABS, PDA200C) was used for amplifying the current signal. The voltages and current were acquired and transferred to the computer with a data acquisition (DAQ) (NATIONAL INSTRUMENTS, NI USB-6361).
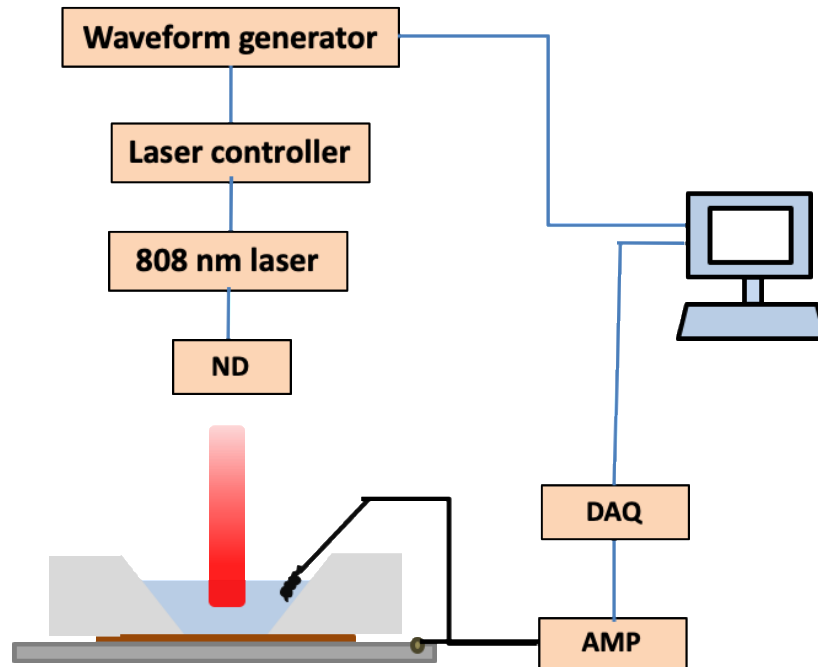
Figure 2.13. Schematic of opto-electric testing system with LabView programs, amplifier (AMP) and data acquisition (DAQ). The intensity of 808 nm laser can be controlled by a laser diode current driver and various neutral density (ND) filters, with programmed signals from waveform generator manipulated by LabView programs.

The pulsed laser signal was modulated with square signal frequency of 50 Hz, i.e. pulse width of 10 ms, with intensities ranging from 0.44 μW/mm^2 up to 68 μW/mm^2, and

then the photovoltages and photocurrents response of the Si/Au nanostructures to the laser signals were recorded.

The sinusoidal laser signal had a peak to peak amplitude from 1.2 to 7.5 $\mu W/mm^2$, the frequency was varied from 1 Hz to 50k Hz, and we recorded the light induced photovoltages and photocurrents versus frequency.

2.4.3 Vibrating sample magnetometer

Vibrating sample magnetometer (VSM) was used to characterize the magnetic properties of materials as a function of magnetic field amplitude. The samples were mounted onto a sample holder of the VSM device (Micro Sence. LOT-Quantum Design. Darmstadt, Germany), parallel or perpendicular to the applied magnetic field as the magnetization loops were tested in plane and out of plane respectively. The sample was located between two electromagnets and between 4 pick up coils, once the electromagnets were powered, the applied magnetic field was variated from -20000 to 20000 Oe, while the samples were continuously vibrating. The induced voltages originated on the pick-up coils were processed by a software and related to the magnetic moment of the sample as a function of the applied magnetic field, thus obtaining the magnetization loops.

In order to evaluate the magnetic properties of ZnO/GaFe/ZnO (20nm/40nm/20nm) nanodomes with different diameters and densities integrated in PDMS film, to find the nanostructure with the lowest magnetic field to saturate the magnetization, we performed VSM in these samples to obtain the magnetization loops, including separated D200nm/ D400nm nanodomes, patterned D400nm/ D500nm nanodomes, and patterned D500nm nanodomes with GaFe layer of 30nm in thickness.

2.4.4 Photothermal efficiency evaluation

In order to evaluate the heating efficiency of the patterned D400nm FeGa/ZnO nanodomes integrated in PDMS film, we tested its photothermal efficiency by measuring the temperature increase as a function of the laser intensities, using 808 nm and 1064 nm wavelength laser illumination (B1-808-1500-15A Laser Components, KA64FAMFA-5.000W), which are within the first and second NIR biological window, respectively.

When the FeGa/ZnO nanodomes sample was illuminated, the temperature was detected and analyzed with a thermal infrared thermopile detector (MLX90614, Melexis). Various measurements were done with different laser intensities for the 808 nm and 1064 nm laser. Finally, the temperature increase (i.e. the rise of temperature with respect to the initial temperature without illumination) as a function of the laser intensities was plotted.

2.5 Cell culture

2.5.1 Human embryonic kidney cells

Human embryonic kidney (HEK) 293 cells are a specific cell line originally derived from human embryonic cells grown in tissue culture. In 1977, HEK 293 cells were generated by transfection of normal human embryonic kidney cells with sheared fragments of adenovirus type 5 DNA[120]. The HEK 293 cells used in this work are a derivative of the HEK 293 cells, they express a single type of voltage-gated K^+ shaker channels.

Cell culture chemicals

HEK 293 cell culture medium: DMEM (Dulbecco's Modified Eagle Medium), with high glucose and glutamin, purchased from ThermoFisher. Cell medium is mixed with 10% of fetal bovine serum (Gibco) and 200 µg/ml of hygromycin B solution (Sigma-Aldrich).

Dulbecco´s phosphate buffered saline (DPBS), without calcium chloride and magnesium chloride, was purchased from Sigma-Aldrich.

Cell culture protocols

- DMEM was removed from petri dish with pipette.

- 3 ml Ca/Mg free PBS was put in the dish and removed afterwards.

- Further 3 ml Ca/Mg free PBS was put in the dish and the dish was placed in the incubator for 5 minutes. In a Ca/Mg free PBS the cells will detach from the bottom of the dish.

- PBS containing the dissolved cells was pipetted in 2 ml Eppendorf and centrifuged for 5 minutes at 2000 rpm.

- Remove the PBS, putting 5 ml DMEM into the Eppendorf, the pellet was detached from the wall and mixed with the medium.

- The cells in DMEM were then diluted depending on the amount of cells and on the further use of the cells, distributing them over several petri dishes.

- The dishes were placed into the incubator at 37 ℃ and 5% CO_2.

HEK293 cells on Si/Au nanopillars

To culture the cells on top of the Si nanopillars, the same protocol was followed. The Si nanopillars samples were sterilized with a bath of 70% ethanol for 2 hours, then the cells were plated at about 10% to 15% confluence. After plating, the cells on the electrodes were incubated for 24 hours with the normal cell medium, to let them attach to the electrode surface.

2.5.2 Cell morphology analysis

In order to make sure that the HEK293 cells can grow well on the Si nanopillars, we checked the SEM after seeding the cells on the samples for 48 hours. The Si/Au NPs samples are sterilized in 70% ethanol for 2 hours, and covered with 0.8 mg/ml of Poly-L-Lysine for 1 hour. Then the cells were introduced into a 4-multiwell plate at density of $3*10^5$ cells/ 2ml in each well, and cultured at 37 ℃ and 5% CO_2. After 48 hours, cultured cells were rinsed in 0.1M Cacodylate buffer, and fixed in 2.5% Glutaraldehyde in PBS for 45 minutes. Cell dehydration was performed by 8 minutes washes in a series of ethanol: 50%, 70%, 90% and twice 100%. Finally, samples were dried using hexamethyldisilazane (HMDS, Electron Microscopy Sciences) for 15 mins, analysed by SEM (FEI Quanta 650F ESEM).

2.5.3 Cell Tracker Green CMFDA Dye assay

At the same time, after seeding the cells for 48 hours, we checked the status of the cells by fluorescence microscope using cell tracker Green CMFDA (Invitrogen). This cell tracker is a fluorescent probe that can easily penetrate cell membranes. When enters the alive cells, a glutathione S-transferase-mediated reaction takes place and makes the cell tracker impermeant, thus only living cells will retain the cell tracker and be able to be viewed on the confocal microscope.

Firstly, the medium was replaced with fresh cell medium (1ml) containing 1μl of cell tracker, incubate them at 37 ℃ and 5% CO_2 for 30 minutes. Then the media was replaced with 1ml of fresh media. The cells were analyzed with fluorescence microscope using green emission (492/517 nm).

2.5.4 Cell proliferation assay

We performed Alamar Blue assay to test the cells proliferation over 1, 2, and 3 days after seeding. We chose the Alamar Blue cell viability reagent (Invitrogen) because it is not toxic to cells and allowed reusing the same cells and materials during the 3 days assay. Firstly, 50000 cells were seeded into each well of a 4-multiwell plate containing Si/Au NPs MD, Si/Au NPs LD and control glass coverslip. After 24 hours, the medium was replaced by fresh medium with 10% Alamar Blue, and kept in standard conditions (37 ℃ and 5% CO_2) for 5 hours. Then the media were replaced with fresh media. Immediately, the fluorescence of the extracted medium was quantified using Cary Eclipse Fluorescence Spectrophotometer (Agilent. Santa Clara, California, USA), with an excitation at 560 nm and emission range between 570 and 600 nm. The assay was repeated after 2 days and 3 days. Experiments were performed in triplicate.

2.5.5 Osteosarcoma cells

The human osteosarcoma cell line Saos-2 (American Type Culture Collection, USA) was cultured in Dulbecco's modified Eagle medium (DMEM; ThermoFisher Scientific, UK) with 10 % fetal bovine serum (FBS; Life Technologies, UK) under standard conditions (37 ℃ and 5% CO_2).

We tested the Saos-2 cells viability cultured on the samples, including patterned FeGa/ZnO nanodomes, isolated FeGa/ZnO nanodomes, and patterned ZnO nanodomes integrated in PDMS film.

This part of work was done in collaboration with Carme Nogués's research group in Universitat Autònoma de Barcelona (UAB). I fabricated the FeGa/ZnO nanodomes integrated onto PDMS film samples, and the students in UAB performed the experiments with Saos-2 cells, including the cell culture, cell morphology test by SEM, and cell tracker green CMFDA dye assay.

Saos-2 cells culture protocol on FeGa/ZnO nanodomes

Prior to culture cells on the FeGa/ZnO nanodomes, the samples were sterilized with a bath of 70% ethanol for 30 minutes, then let them dry inside the biosafety cabinet for another 30 minutes. The samples with 5 mm x 5 mm size were put inside a 24-multiwell plate. All the samples were tested in triplicate. Then 150.000 Saos-2 cells were cultured in each well, as well as in control wells (i.e. the wells without any samples), following the protocol below:

- Cell medium (DMEM with 10 % FBS) was removed from petri dish.

- 8 ml Ca/Mg free Hank's Balanced Salt Solution (HBSS) was put in the dish and removed afterwards.

- 2 ml trypsin was put in the dish and placed in the incubator for 5 minutes.

- 8 ml of fresh cell medium was added in order to stop the action of trypsin, and the cells detached from the bottom of the dish.

- The cells were counted in the Neubauer chamber and the concentration of cells could be calculated, as well as the volume containing 150.000 cells.

- In our case, we put 500 µL cells in each well and added 500 µL cell medium.

- The dishes were placed into the incubator at 37 ℃ and 5% CO_2.

2.5.6 Characterization of Saos-2 cells on FeGa/ZnO nanodomes

We evaluated the Saos-2 cells viability cultured on FeGa/ZnO nanodomes by SEM to check cell morphology, and cell tracker green CMFDA dye assay to check the live cells.

Cell morphology analysis

We checked the SEM after seeding the cells on the samples for 24 hours. Samples with cells were rinsed with phosphate buffered saline (PBS), then the cells were fixed in 4 % paraformaldehyde (PFA) in PBS for 15 minutes. Cell dehydration process was performed by 8 minutes washes in a series of ethanol: 50%, 70%, 90% and twice 100%. Finally, samples were dried using hexamethyldisilane (HMDS, Electron Microscopy Sciences) for 15 mins.

The samples with dried cells were mounted on the SEM stubs and sputtered with Pt of 5 nm thickness, then analysed by SEM (Zeiss Company, Oberkochen, Germany).

Cell tracker green CMFDA dye assay

We performed the cell tracker green CMFDA dye (Eugene, Oregon, USA) assay after 3 days of cell culture. Firstly, the cell medium was replaced with fresh cell medium (1ml) with 1μl of cell tracker for all the samples, and incubated in standard conditions (37 ℃ and 5% CO_2) for 15 minutes. Then the medium was replaced with 1ml of fresh cell medium. Finally, the cells were checked with fluorescence microscope using green emission (492/517 nm).

3 Si/Au Nanostructures for wireless opto-electric cell stimulation in the NIR biomedical windows
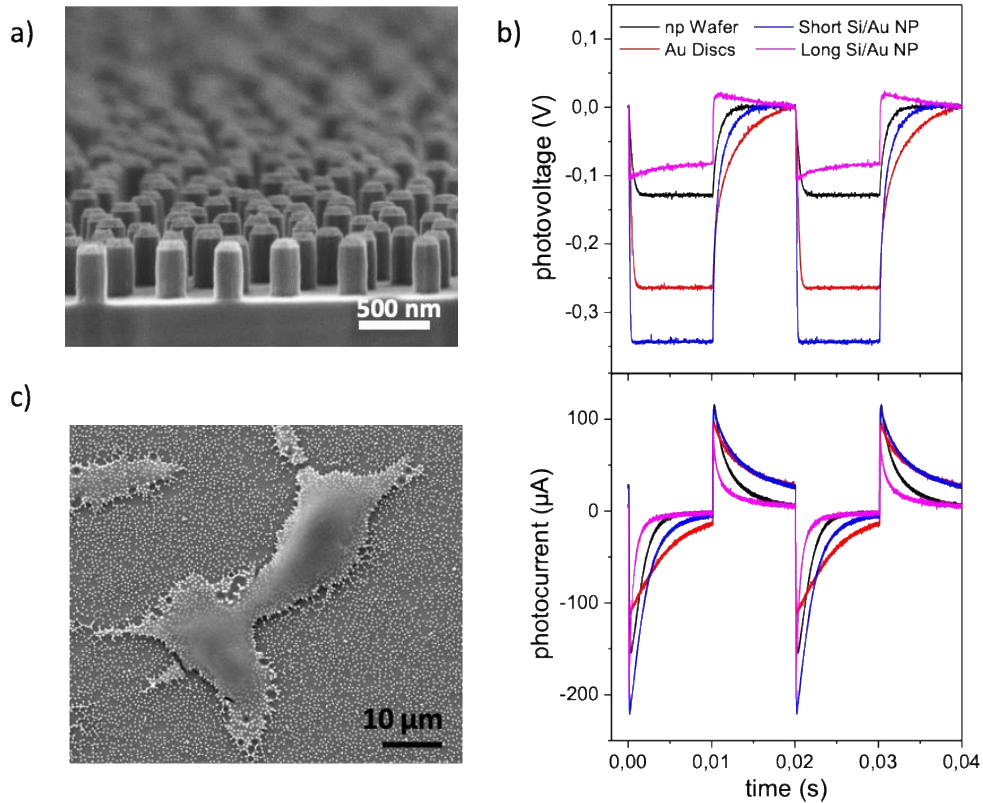
TOC Figure. (a) SEM image of short Si/Au nanopillars (D ≈ 230nm, L ≈ 350 nm) on the p-n Si wafer. (b) Photovoltage and photocurrent under square laser pulses at 22 µW/mm^2, pulse width 10 ms. (c) HEK 293 cells cultured on Si/Au nanopillars.

Abstract:

In this Chapter we first theoretically analyzed the electronic and light absorption features of the Si/Au nanostructures on wafers with p-n junctions, with the objective of maximizing the photon trapping efficiency, the photogenerated charges separation and the charge injection in the electrolyte solution. We show that Si/Au nanopillars (diameter around 200 nm) exhibit hybrid metal/dielectric resonances within the first NIR biological window enabling a large enhancement of the electromagnetic field

distribution at the Si/Au interface and inside the Si nanostructures, within the active p-n junction region. This leads to a 4- to 6-fold enhancement of the light absorption within the first micron depth, for wavelengths in the first biological window (ca. 800 nm). We exploited the simple, robust, tunable and scalable strategy for the nanofabrication of Si/Au nanostructured surfaces described in Chapter 2. Next, we studied the opto-electric performance of the Si/Au nanostructures by evaluating their photovoltage and photocurrent response to pulsed light and sinusoidal light of 808 nm wavelength. We found that the short Si/Au nanopillars presented the highest opto-electric performance, achieving photovoltage of 80 mV at ultralow light intensity of 0.44 μW/mm^2, which is 11-fold higher than the plain p-n Si wafer, and photocurrent of 37 μA at irradiance of 20 μW/mm^2, showing a behaviour of combination of light-induced capacitive and Faradaic currents. We then probed the opto-electric performance of short Si/Au nanopillars with different densities to find the optimized nanostructure. In addition, we presented the opto-electric performance of short Si/Au nanopillars with p-type Si exposed, which showed reversed photovoltage and photocurrent, indicating the applied potential for hyperpolarization of cell membrane. We also studied the opto-electric performance of short Si/Au NP D350 nm/ D230 nm under pulsed illumination with 1064 nm and 808 nm laser, for exploring their opto-electric property in the second biological window. Finally, we validated the cell viability cultured on the Si/Au nanostructured devices.

Considering the need to drastically increase the opto-electric actuation efficiency of implantable devices in the near-infrared (NIR) biomedical windows for reducing the required light intensity and achieving safe actuation in deeper tissues, three main steps must be carefully designed and optimized: i) the efficient photon absorption, ii) the correct separation of the photogenerated carriers, and iii) the efficient charge injection into the electrolyte solution.

To fulfil these conditions with NIR light in the first biological window, we selected a system formed by a monocrystalline Si wafer with p-n junction whose surface is nanostructured by Si nanopillars capped by Au nanodiscs (Fig. 3.1). The low band-gap of monocrystalline Si enables NIR opto-excitation, and robust control of the doping levels and band structure *via* standard microelectronic techniques to form tailored p-n junction, for separating the photocarriers. On the other hand, Au nanostructures in direct contact to the Si form a Schottky junction to efficiently trap the photoelectrons, thus acting as electron concentrators and reduction centers for injecting the electrons into the electrolyte solution.

3.1   Design of Si/Au nanostructures for efficient opto-electric stimulation

We started with the rational design of the geometric, optical and electronic properties of the Si/Au nanostructured surfaces to maximize the light trapping efficiency, the photogenerated carriers separation and the charge injection in the electrolyte solution by combining: i) semiconductor band engineering, ii) semiconductor/metal junctions, and iii) surface nanostructuration *via* scalable and cost-effective colloidal lithography techniques.
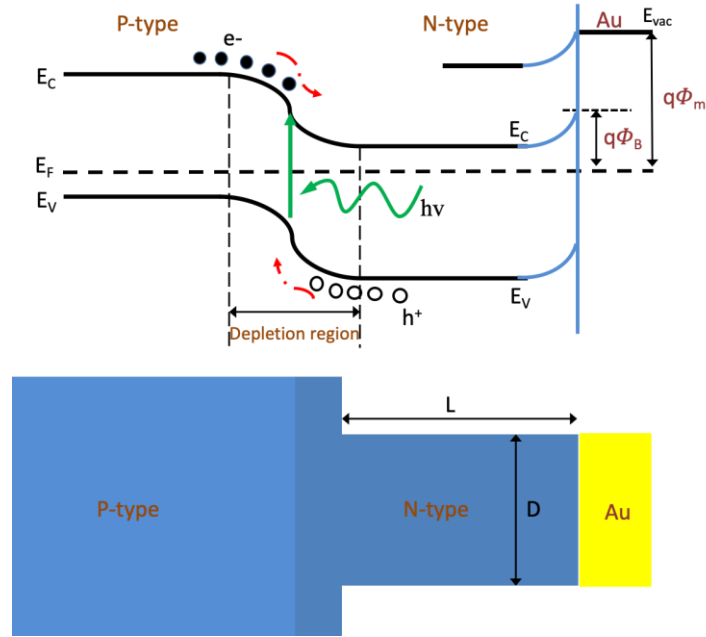
Figure 3.1. Schematic band diagram of the p-Si/n-Si/Au nanostructured system.

Considering the schematic band diagram of the p-Si/n-Si/Au nanostructure shown in Fig. 3.1, the absorbed photons generate electron-hole pairs, and the photogenerated electrons within the p-n junction are pushed towards the Au interface by the built-in electric field in the depletion region of the junction. The induced electric potential by such field can help photoelectrons overcoming the Schottky barrier formed at the n-Si/Au interface. Thus, photogenerated electrons can be efficiently trapped at the Au structures and then injected into the electrolyte solution for producing the photocurrent[121,58,122].

To achieve efficient opto-electric effects at ultralow light levels, a very efficient photon absorption in the active region is necessary. However, monocrystalline silicon is a poor optical absorber in the NIR due to its very low absorption coefficient in this spectral region. In fact, the light absorption percentage during the first 1.2 µm of the Si wafer, which is the region in which photogenerated carriers efficiently generate photovoltages due to the p-n junction, drops from 20% at 650 nm to 1.75% at 900 nm wavelength (Fig. 3.2a) and 0.53% at 1000 nm. Such absorption efficiency reduction imposes a large increase of the photon flux to achieve similar photovoltages.

The modification of the Si wafer surface with Au nanodiscs or Si nanopillars do not generate a noticeable increase in the NIR light absorption within the active p-n junction region (Fig. 3.2 a). The Au nanodiscs on the flat Si wafer generate a plasmonic resonance located around 1800 nm (Fig. 3.2b), i.e. far from the Si bandgap energy threshold. In addition, a very small resonance peak located around 830 nm is observed, which shows a weak electromagnetic field confinement at the Si/Au interface (Fig. 3.2d). On the other hand, the dielectric Mie resonances of short/ long Si nanopillars (NP) on a Si wafer are drastically damped due to the high refractive index Si substrate.
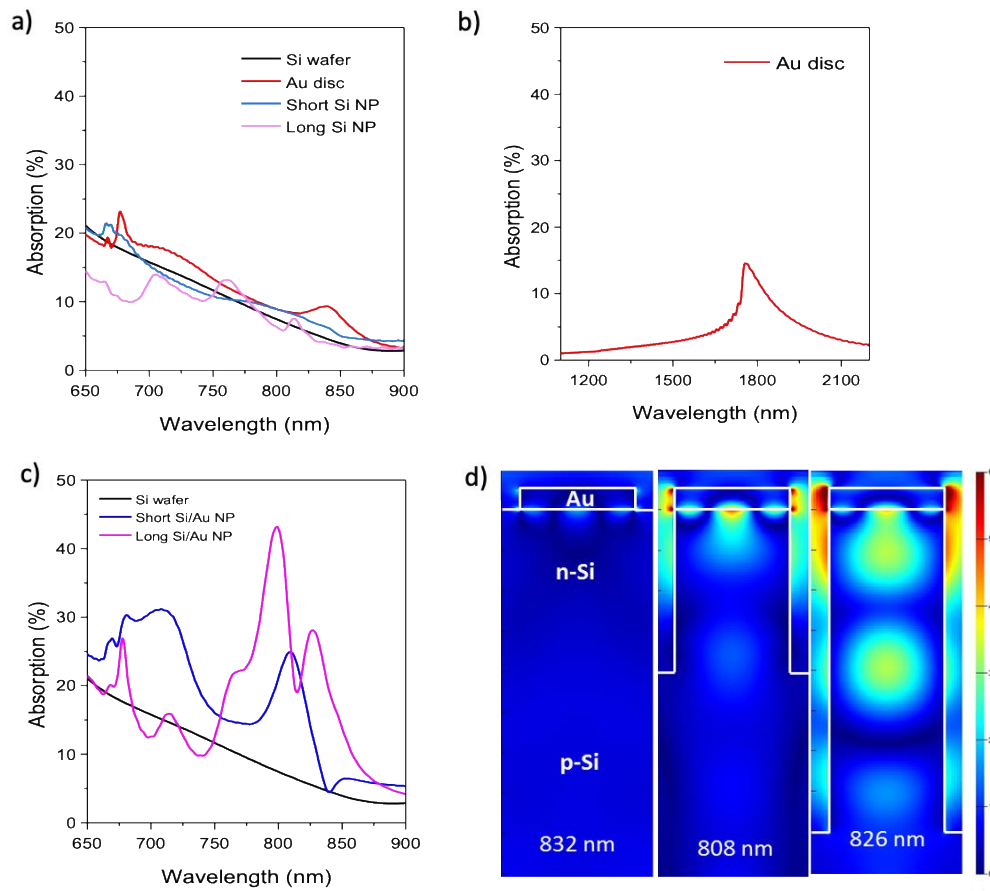

Figure 3.2. (a) Absorption spectra after 1 μm light penetration inside the Si wafer, for the plain Si wafer with p-n junction, Au discs on the Si wafer, Si nanopillars of 350 nm (short) and 800 nm (long) in length, by Finite-difference time-domain (FDTD) simulation. (b) Absorption spectrum of Au discs on Si wafer in NIR range. (c) Absorption spectra of short Si nanopillar with Au disc, long Si nanopillar with Au disc, and the plain Si p-n wafer. (d) Electric field (Abs [Ex]) distributions for Au nanodiscs, short and long Si/Au nanopillar at the resonances located at 832 nm, 808 nm and 826 nm wavelength, respectively.

In contrast, the combination of Au and Si nanostructures, i.e. Si nanopillars capped with Au discs, gives rise to strong hybrid metal/dielectric resonances, which lead to large amplification of the absorbed light in the p-n region (Fig. 3.2c). By properly adjusting the diameter and length of the Au/Si nanostructures, it is possible to generate strong hybrid resonances in the first biological spectral window. These resonances generate an intense electromagnetic field enhancement both at the Si nanopillar and, particularly, at the Si/Au interface (Fig. 3.2d). Therefore, the hybrid metal/dielectric structures enable enhancing the photon absorption at the active opto-electronic regions, *i.e.* the p-n and Schottky junctions. For long Si/Au nanopillars (diameter D = 230 nm, length L = 800 nm) the hybrid resonances lead to 6-fold enhancement of the absorbed light at 800 nm and 826 nm wavelengths. The amplification is 2-fold and 4-fold in shorter Si/Au nanopillars (D = 230 nm, L = 350 nm) for the hybrid resonances located at 710 nm and 808 nm wavelengths, respectively.

For larger diameters, the hybrid resonances are red-shifted (Fig. 3.3a). This feature enables controlling the light color sensitivity of the nanopillars through the tunable diameters. Remarkably, D = 350 nm Si/Au nanopillars showed a resonance near 1 μm, which provides the possibility to actuate the Si/Au nanopillars in the second NIR biological window and above the bandgap threshold, i.e. in the range from 1000 nm to 1100 nm. The reduction of the Si/Au nanopillars diameters can also enable tuning the resonances within the visible spectrum to provide color-dependent enhancement in ultrathin Si films.
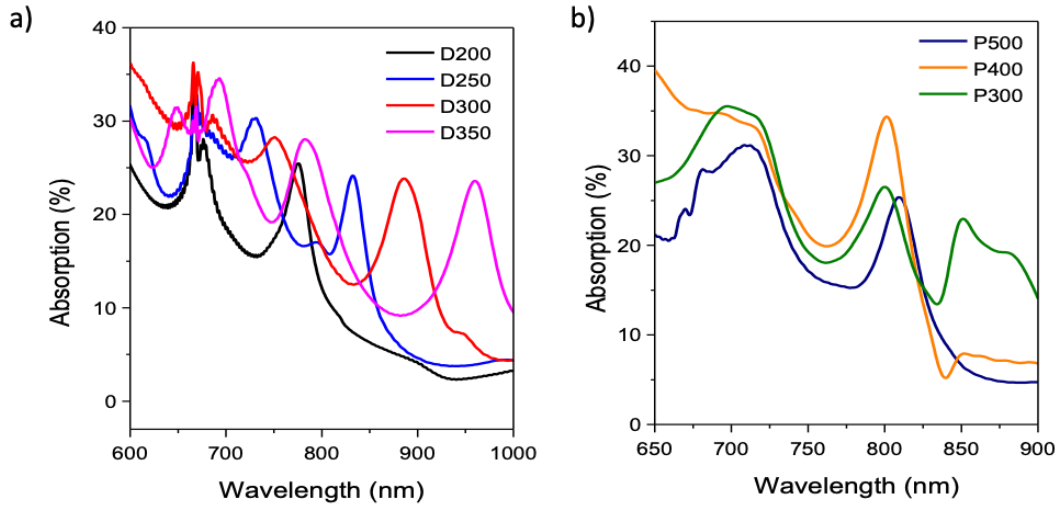
Figure 3.3. (a) FDTD absorption spectra of short Si/Au nanopillar arrays with diameters from 200 nm to 350 nm. (b) FDTD absorption spectra of short Si/Au nanopillar arrays with different densities by changing the array pitch from 500 nm to 300 nm.

Besides, the density of nanopillars can also affect the light absorption. As shown in the calculations of Fig. 3.3b that vary the pitch from 300 nm to 500 nm keeping a constant diameter, the short Si/Au nanopillars with 400 nm pitch show the highest absorption, thereby suggesting the optimal separation distance for diameter of 230 nm nanopillars.

In conclusion, based on the theoretical analysis, we proposed that the Si nanopillars capped by Au disc structure could: i) achieve efficient light absorption in the p-n region and at the Si/Au interface due to the strong hybrid metal/dielectric resonances, ii) improve charge trapping and injection through the Au disc, and iii) ensure fast light-generated charges separation through the p-Si/n-Si band engineering. In addition, the light absorption efficiency is related to the length, diameter and density of the Si/Au nanopillars.

3.2   Fabrication of Si/Au nanostructured system

To prove these hypotheses, we fabricated the opto-electrically active Si/Au nanostructures following the cost-effective and scalable process described in Chapter 2, for the opto-electric analysis and optical cell stimulation study, including (Fig. 3.4):

a) Si p-n wafer, b) Au nanodiscs on Si p-n wafer, c) short and d) long Si/Au nanopillars with different densities and diameters. The fabrication process started with the n-dopant implantation on 4-inch p-type silicon wafer, up to a depth of 560 nm ± 10 nm. Next, a 75 nm Au layer was deposited, which was followed by electrostatic colloidal self-assembly of polystyrene nanospheres (diameter *ca.* 200 nm) on the Au surface, leading to a randomly ordered but homogeneous distribution of colloids on the whole wafer. The nanospheres were used as masks to produce the Au discs by Ar ICP-RIE. Finally, the Au discs were used as masks to obtain Si/Au nanopillars (NP) with tunable lengths by deep reactive ion etching *via* Bosch process.
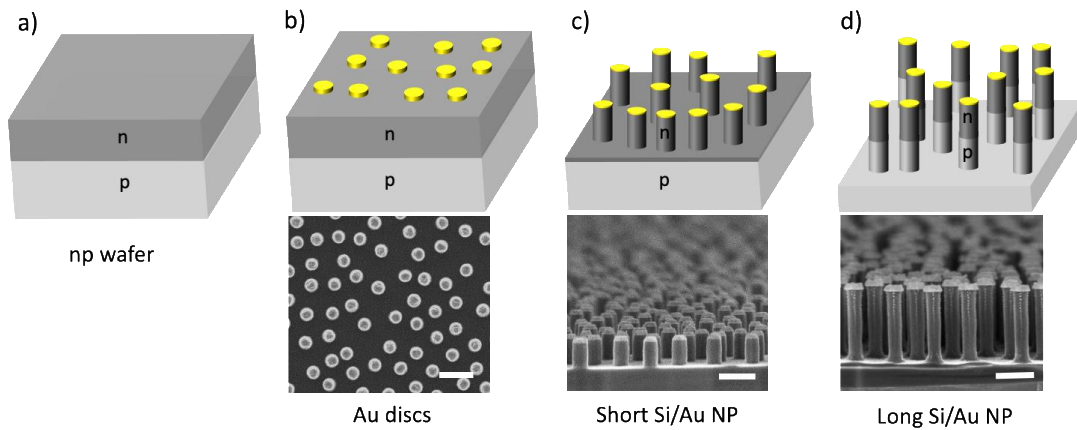

Figure 3.4. Schematics and corresponding SEM images of the different samples used for the opto-electric analysis: (a) Si wafer with p-n junction depth at 560± 10 nm; (b) Au discs on the p-n Si wafer; (c) Short Si/Au NP (D ≈ 230nm, L ≈ 350 nm), and (d) Long Si/Au NP, (D ≈ 230nm, L ≈ 1 µm) on the p-n Si wafer. Scale bar: 500 nm.

3.3 Opto-electric performance of Si/Au nanostructures

The action potential of excitable cells can be triggered by applying either voltage changes or currents (*e.g.*, 70 mV pulses[123] or 0.5 nA current pulses of 15 ms in neuron[124]) to activate the cellular ion channels and raise the membrane potential above the threshold value to generate the membrane depolarization. This process usually happens in a time range of several to tens of milliseconds.

Opto-electric tests with square light pulses

To assess the potential of the Si/Au nanostructures for efficient wireless and power free (i.e., without the need to apply a bias voltage) cell stimulation with high penetration and safe NIR light, we first studied the photovoltage and photocurrent response of the Si/Au nanostructures to square light pulses (10 ms) with 808 nm wavelength (*i.e.*, within the first NIR biological window) and under physiological conditions (phosphate buffered saline 1X, pH 7.4). In these measurements we used a metal contact at the back of the Si wafer as working electrode and a Pt wire electrode in the electrolyte solution as counter electrode, as described in Chapter 2.

As can be observed in Fig. 3.5a and b, square light pulses of 10 ms length induced square-shaped photovoltages, with a slower decay when the light pulse finishes. At a light intensity as low as 8.7 μW/mm^2 (Fig. 3.5a), the p-n Si wafer showed the lowest photovoltage (80 mV), which reflects its low absorption efficiency at the NIR. The incorporation of the Au nanodiscs provides a substantial photovoltage enhancement (200 mV), which is a result of the improved photocarrier separation by the Si/Au Schottky junction. Interestingly, the short Si/Au NP exhibited the largest photovoltage (280 mV), i.e. 3.5-fold larger than the plain p-n Si wafer. Such a high photovoltage amplification is due to the synergistic combination of increased photon absorption by the hybrid metal-dielectric resonance induced by the Si/Au nanostructure and the enhanced carrier separation of the Si/Au Schottky junction. In contrast, the long Si/Au NP shows a drastically lower photovoltage than the short Si/Au NP, despite it has the highest theoretical photon absorption. In this case, the p-n junction is completely exposed to the conductive electrolyte solution, which results in the short-cut of the junction, thus hampering the photocarriers separation. This effect can also be observed as a deformation of the square-shaped photovoltage, showing a slow decay during the constant light illumination period due to the rearrangement of the electrolyte double layer ions, whose dynamics is slower than that of the photocarriers. These results clearly point out that both the efficient optical absorption and the adequate photocarrier separation are key to amplify the photovoltages at low light levels.
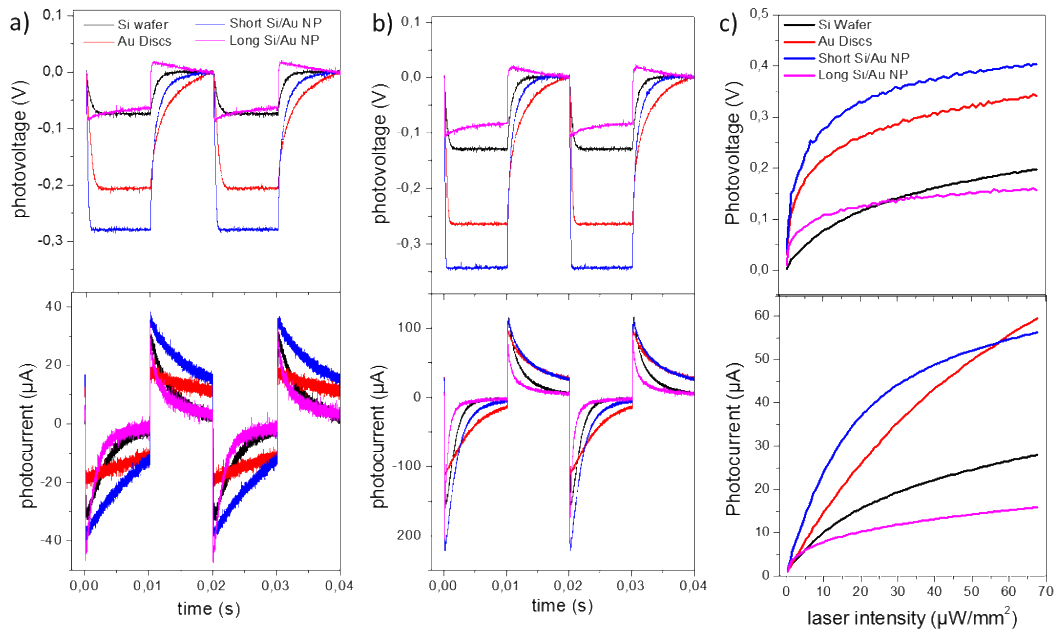
Figure 3.5. Photovoltage and photocurrent induced by laser illumination. (a) Photovoltage and photocurrent under square laser pulses at 8.7 μW/mm^2, pulse width 10 ms, (b) at 22 μW/mm^2. (c) Photovoltage and average photocurrent dependence on laser intensity.

The increase of the light intensity at the higher light intensity of 22 μW/mm^2 (Fig. 3.5b) produced a non-linear photovoltage rise for all the samples, keeping similar shapes as for low light intensity. This non-linear behavior can be seen in Fig. 3.5c, which displays the photovoltage as a function of light intensity. In the whole range (0-68 μW/mm^2) the short Si/Au NP sample presented the highest photovoltage with clear signs of saturation after 20 μW/mm^2 light intensity, where the photovoltage reached 329 mV. The p-n junction short-cut was even more evident at larger light intensities by the weak photovoltage increase in the long Si/Au NP sample. Another interesting parameter to analyze is the voltage responsivity at ultra-low light intensity, which can be defined as $\eta = dV/dI_{light}$, where V is the induced photovoltage and I_{light} is the light intensity. At the lowest measured intensity of 0.44 μW/mm^2, the voltage responsivity was 15, 133, 167 and 74 mV$\cdot$mm^2/μW for the plain p-n wafer, the Au nanodiscs and the Si/Au short and long nanopillars, respectively (Fig. 3.6). At this light intensity range, the short Si/Au NP achieves a 11-fold amplification of the photovoltage with respect to the plain p-n

Si wafer. The extremely high responsivity of the short Si/Au NP indicates that light intensities as low as 0.44 µW/mm^2 might be used to elicit action potentials, which is almost 3 orders of magnitude lower than the smallest intensity reported for cell stimulation (Table 2).
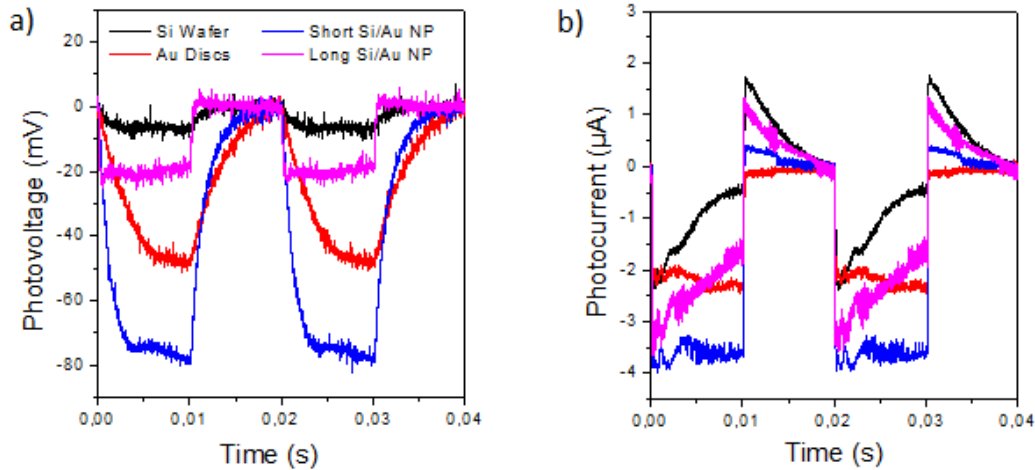

Figure 3.6. Comparison of (a) photovoltages and (b) photocurrents at ultralow laser intensity of 0.44 µW/mm^2.

As previously mentioned, excitable cells can also be fired by applying a current. The photocurrents show that Si wafer and long Si/Au NP present a sharp increase in current, followed by a fast decay to zero (Fig. 3.5a). This rapid decay is characteristic of a capacitive current, coming from accumulation of electrolyte ions near the solid surface to balance light generated excessive charge carriers. In the particular case of the long Si/Au NP, the faster decay also reflects its higher carrier recombination rate, which is due to the combination of p-n junction shortcut (i.e. less efficient carrier separation) and the increase number of defects at the lateral surface of the nanopillar.

In contrast, Au discs and short Si/Au NP showed a fast initial increase and sustained current afterwards, instead of returning to zero quickly during the 10 ms actuation, thus suggesting the combination of light-induced capacitive and Faradic currents[66]. This behavior is promoted by the Au cap, which can improve the photo-electrons trapping and injection into the solution at the solid-liquid interface for enhancing the reduction reactions. Notably, the photocurrents reverse to positive when light is off, indicating a

discharging process, and possibly the reversibility of the redox reaction at the Si/Au interface.

To show the evolution of the current with respect to the light intensity, we measured the photocurrent at different laser intensity points, and calculated the average peak-to-peak current amplitude in the 20 ms pulse period, by calculating the integral of the absolute value of the current over the 20 ms period, then divided by the period (Fig 3.5c). Likewise the photovoltage, the average photocurrent amplitude of short Si/Au NP is the highest of all the samples, reaching 37 μA at an irradiance of 20 μW/mm^2, which is 2.5-fold enhancement with respect to the plain Si wafer.

At ultralow light intensity of 0.44 μW/mm^2 (Fig. 3.6b), the photocurrent of Au discs followed the square light pulse shape, showing a Faradaic behavior, and when the light was off, there was no discharging current. The short Si/Au NP also presented a square photocurrent shape, showing the largest photocurrent, with a small reversed current when light was off. In contrast, the Si wafer and long Si/Au NP showed clear combination of capacitive and Faradaic current, with a small discharging current when light was off.

Opto-electric tests with sinusoidal light pulses

Apart from the power and duration of the applied voltage or current, the shape and frequency of the actuation signals can also play an important role for efficient cell stimulation. For example, the percentage of successful action potential spikes in cultured neurons may be different with varying stimulation frequency[72]. This effect has been observed by Parameswaran et. al. in neurons cultured with Si nanowires[60], the cells were able to generate trains of action potentials with injected current at 10 and 20 Hz, but failed to respond to every pulse at 40 Hz. In contrast, DRG neurons cultured with Au nanoparticles were able to generate action potentials at a stimulation rate of at least 40 Hz[83].

The different behavior with respect to the pulse shape and frequency is related to the photo-electro-chemical properties of the structures. This is due to the fact that both the diode response and the impedance of the electrode-electrolyte interface are very dependent on the frequency. According to the equivalent circuit model of electrode-

electrolyte interface shown in Fig. 3.7, the interface impedance can be calculated by the equation:

$$Z = \frac{1}{\frac{1}{R_{dl}} + \omega C_{dl}} + R_{el}$$

where Z represents the interface impedance, R_{dl} represents the charge transfer resistance, ω represents the angular frequency, C_{dl} represents the double layer capacitance, R_{el} represents the electrolyte resistance at the interface.

At high frequencies, $\omega C_{dl} \gg 1/R_{dl}$ ($\omega = 2\pi f$), the equivalent resistance of the C_{dl} and R_{dl} in parallel ($\frac{1}{\frac{1}{Rdl} + \omega Cdl}$) is near the value of the capacitive reactance ($\frac{1}{\omega Cdl}$), which is approximately 0. Thus, the interface impedance is constant and approximately equal to R_{el}. At very low frequencies, $\omega C_{dl} \ll 1/R_{dl}$, the equivalent resistance of the C_{dl} and R_{dl} in parallel ($\frac{1}{\frac{1}{Rdl} + \omega Cdl}$) is near the value of R_{dl}, as a result, the interface impedance is approximately equal to $(R_{dl} + R_{el})$[125].
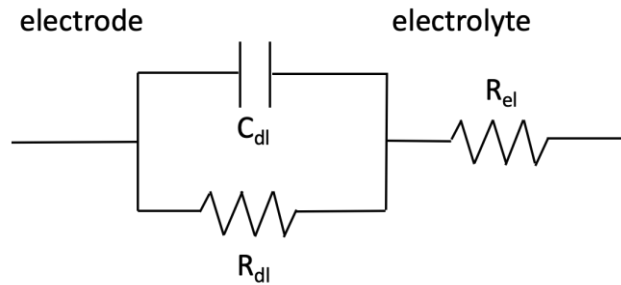

Figure 3.7. Equivalent circuit model of electrode-electrolyte interface. C_{dl} represents the double layer capacitance, R_{dl} represents the charge transfer resistance, R_{el} represents the electrolyte resistance at the interface.

Therefore, we further studied the effect of frequency on photovoltage and photocurrent of the Si/Au nanostructures, using sinusoidal light actuation, with small modulation amplitude from 1.2 to 7.5 µW/mm^2 (i.e. peak-to-peak intensity modulation of 6.3 µW/mm^2), taking the photovoltage and photocurrent as a function of the actuation

frequency for extracting the relevant electric parameters at the Si/Au/electrolyte interfaces.

As can be observed in Fig. 3.8 (a), the short Si/Au NP presented the largest photovoltage response. Besides, all the samples showed a photovoltage drop which gave the bandwidth for efficient photovoltage generation. The short Si/Au NP exhibited higher cut-off frequency (i.e. peak of the imaginary part, 650 Hz) than the Si p-n wafer and Au discs, which were both around 250 Hz. Interestingly, although the photovoltage of long Si/Au NP was lower, its response can be faster due to the cut-off frequency was around 10 kHz.
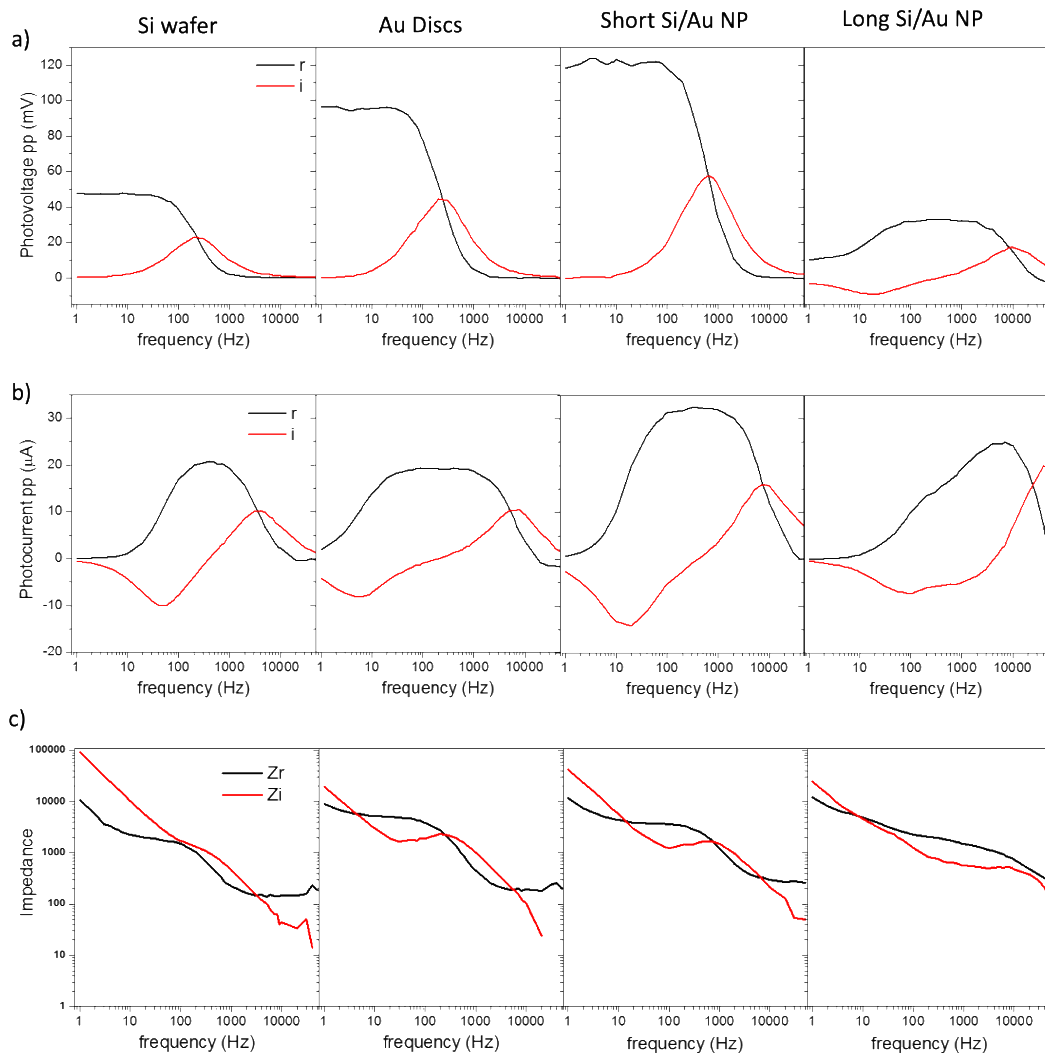

Figure 3.8. (a) Photovoltage and (b) photocurrent peak to peak amplitude generated by sinusoidal light modulation as a function of the frequency. (c) Impedance as a function of the frequency. Black line (r): real part. Red line (i): imaginary part.

The photocurrents for all the samples were low at very low frequencies (< 20 Hz) (Fig. 3.8b), due to their strong impedance at this frequency range imposed by the high capacitance. The high capacitance could also be observed in the impedance curves (Fig. 3.8c), which showed that the imaginary impedance (capacitive impedance) was larger than the real impedance for all the samples. Notably, the Au discs presented the highest photocurrent and lowest imaginary impedance in this range, which confirmed its lowest capacitance due to the higher Au/Si surface ratio.

The photocurrents then increased, and the short Si/Au NP presented the largest photocurrent, showing the maximum photocurrent in the range of 50-1500 Hz. In addition, for the Si p-n wafer, Au discs and long Si/Au NP, the photocurrents were maximized around 430 Hz, 50-900 Hz, and 10 kHz, respectively.

Despite the photovoltage drop in all the samples, the photocurrent could be maintained at higher frequencies due to the decrease of the capacitive impedance. However, there was also a current drop in all the samples, that took place at higher frequencies than the photovoltage drop. The short Si/Au NP also exhibited higher cut-off frequency (8 kHz) than Si p-n wafer (4 kHz) and Au discs (7 kHz). In particular, for the long Si/Au NP the photocurrent decay took place at much higher frequency, i.e. larger than 50 kHz.

Therefore, the short Si/Au NP gave the largest photovoltage and photocurrent response compared with the other samples, especially at ultra-low light intensities, thus being the most promising for cell stimulation. To maximize both the photovoltage and photocurrent in this sample, the frequency analysis suggests a range between 50 Hz and 200 Hz (i.e. 2.5 - 10 ms pulses) for efficient cell stimulation.

3.4 Effect of density in the opto-electric performance of short Si/Au nanopillars

As demonstrated above, the short Si/Au nanopillars presented the highest opto-electric performance compared to the plain p-n Si wafer, Au discs on Si p-n wafer, long Si/Au nanopillars. Taking account that the nanopillars density may also affect their light absorption efficiency (Fig. 3.3b) and the amount of Au nanostructures the electron injection dynamics, we next studied the opto-electric performance of the short Si/Au nanopillars with different densities. We compared short Si/Au NP with pitch of 300 nm

(high density – HD, 111 NPs per 10 μm^2), and short Si/Au NP with average center-to-center separations around 800 nm (middle density – MD, 16 NPs per 10 μm^2) and 5 μm (low density – LD, 0.4 NPs per 10 μm^2), as illustrated in Fig. 3.9.
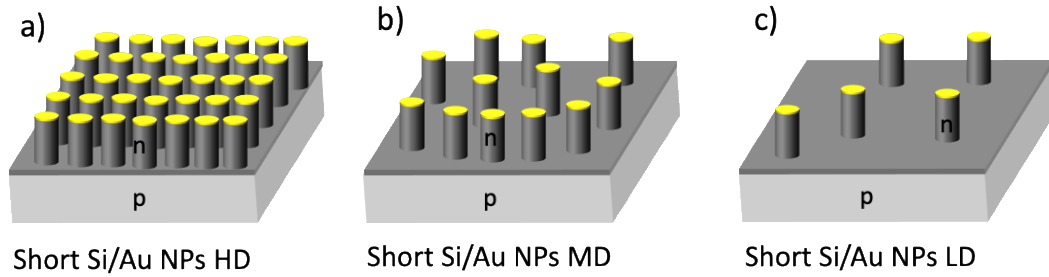

Figure 3.9. Schematic of short Si/Au nanopillars with high density (HD), middle density (MD), and low density (LD).

As can be observed in Fig. 3.10, under square light pulses, the photovoltages of the short Si/Au NP for all the densities follow the square shape, with a slower decay when the light pulse finishes. All the samples showed a non-linear photovoltage response with respect to the light intensity. In the whole light intensity range (0-68 $\mu W/mm^2$), the short Si/Au NP MD sample presented the highest photovoltage, compared to the short Si/Au NP LD and HD samples. This result confirms that the density of hybrid nanostructures is an important parameter to optimize the light absorption efficiency for maximizing the induced photovoltages.

However, the photocurrents behaviour showed a different tendency. The first interesting observation is that the HD sample shows smaller initial current peaks, but a remarkably slower current decay with respect to the LD, and MD samples, which are clearly observed in the Figs. 3.10 a-b for the 10 ms light pulse at 8.7 $\mu W/mm^2$ and 22 $\mu W/mm^2$ illumination intensity. Moreover, the LD sample showed the fastest current decay. This behavior highlights the importance of the density of Au nanostructures to change the current behavior from very capacitive (LD sample) to more Faradaic (HD sample). This different current behavior is even more pronounced at higher light intensities. The photocurrents of the three samples all present non-linear increase of the average current with the light intensity. Notably, although from 1.2 to 28 $\mu W/mm^2$, the short Si/Au NP MD gave the highest photocurrent, above 28 $\mu W/mm^2$, the short Si/Au NP HD clearly outperforms the average current amplitude. This further proved the

importance of the Au discs as electron collector sources to amplify the current response of the nanostructured Si/Au surface.
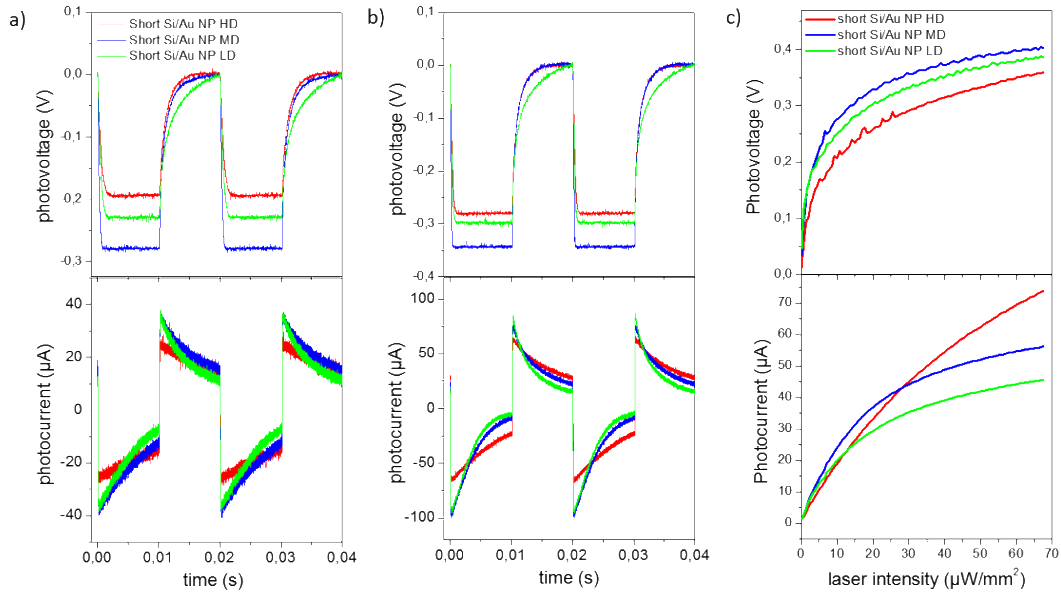

Figure 3.10. Photovoltages and photocurrents of short Si/Au NP with different densities. (a) Photovoltage and photocurrent under square laser pulses at 8.7 µW/mm^2, pulse width 10 ms, (b) at 22 µW/mm^2. (c) Photovoltage and average photocurrent dependence on laser intensity.

Therefore, taking all the results together, the short Si/Au NP MD showed the most interesting opto-electric features for wireless optical cell stimulation under ultra-low light intensities, both in terms of generated photovoltages of photocurrents. However, the higher density of Si/Au nanostructures can be a relevant parameter to tune the photocurrent of the system from a more capacitive to more Faradaic response.

3.5 Effect of p-n junction polarity

Extracellular electrical stimulation can cause depolarization or hyperpolarization of excitable cells depending on the polarity of the electrical stimulator[126]. The electrical stimulation that makes the outside surface of cell membrane more negative, results in a

more positive intracellular potential, which can depolarize the cell membrane and, consequently, trigger action potentials[127]. The Si/Au NP showed above were fabricated on Si p-n wafer with n-type Si on top, inducing a negative photovoltage and a cathodic process at the electrode/electrolyte surface, which can be utilized for depolarization of cells. To explore the ability of the short Si/Au NP for hyperpolarization of the cell membrane, we next studied the effect of the polarity in the Si/Au NP by reversing the p-n junction direction (i.e. p-type Si on top of the wafer). We compared the light induced photovoltages and photocurrents generated by the short Si/Au NP on Si np (n on top) or pn (p on top) wafers, together with the response of the short Si/Au NP on p-type wafer (without p-n junction), keeping the same nanopillars density and diameter of 230nm.

As shown in Fig. 3.11a, the short Si/Au NP pn presented positive photovoltage under pulsed laser illumination, with very similar shape and absolute value as that of the short Si/Au NP np sample. The photovoltage increased with larger laser intensities, and the values were very close to the np counterpart for the whole intensity range. On the other hand, the short Si/Au NP p sample did not show photovoltage and photocurrent response to laser illumination, which confirmed the effect of p-n junction for efficiently separate the photoinduced charge carriers, and the negligible effect of the Au/Si Schottky contact.

In addition, the induced photocurrent of the short Si/Au NP pn also presented opposite polarity to the short Si/Au NP np (Fig. 3.11c), indicating an anodic process at the electrode/electrolyte surface. The photocurrent increased with larger laser intensities, showing similar values with short Si/Au NP np at intensities in the 0.44 to 20 $\mu W/mm^2$ range, and became larger than that in the short Si/Au NP np at intensities above 20 $\mu W/mm^2$.

These results suggested the possibility to efficiently induce the hyperpolarization of the cell membrane through light activation by reversing the polarity in the arrays of short Si/Au NP.
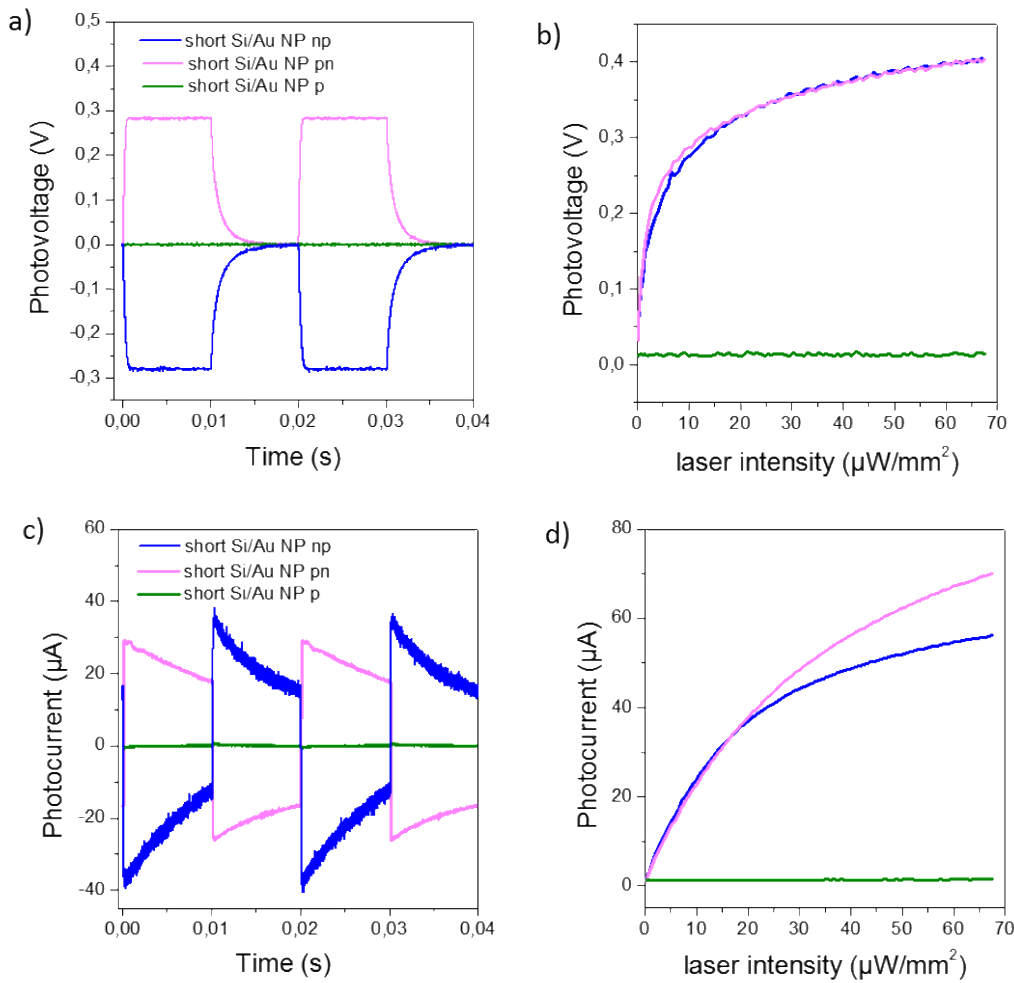
Figure 3.11. (a) Photovoltage and (c) photocurrent of the short Si/Au NP np, short Si/Au NP pn and short Si/Au NP p samples under square laser pulses at 8.7 µW/mm^2, pulse width 10 ms. (b) Photovoltage and (d) photocurrent dependence on laser intensity.

3.6 Opto-electric performance in the second biological window

The second NIR biological window (1000 nm–1350 nm) can provide deeper penetration depth into tissues, reduced phototoxicity[128], and higher maximum permitted light exposures compared to the first biological window. It is worth noting that at 1064 nm the monocrystalline Si is almost transparent, showing an absorption lower than 1%

in the first micron of a flat Si wafer, thus achieving an efficient stimulating at this wavelength is more challenging.

Considering that the FDTD simulations showed a red-shift the hybrid resonances by increasing the diameter of short Si/Au NP (Fig. 3.3a), we selected NP with 350 nm diameter and expected resonance around 1000 nm wavelength to maximize the light absorption efficiency in the range. We compared the opto-electric response of the short Si/Au NP with dimeters of 350 nm and 230 nm and the plain np-wafer under pulsed illumination with 808 nm and 1064 nm lasers, i.e. in the first and second biological window, respectively. However, due to the lack of 350 nm polystyrene spheres to carry out the electrostatic colloidal self-assembly, we employed the hexagonal closed packed self-assembly with diameter of 500 nm, thus yielding much higher density of nanopillars.

As presented in Fig. 3.12a, under square laser pulses of 22 $\mu W/mm^2$, all the samples gave larger photovoltages at 808 nm than at 1064 nm, which is consistent with the lower absorption of Si at longer wavelengths. The photovoltage drop was especially significant for the plain np-wafer, being 4-fold lower at 1064 nm. The decay was lower for the 350 nm diameter NPs（ 1-fold), and remarkably, was minimal for the D230 nm NP (0.17-fold). Therefore, at this intensity with the 1064 nm laser, the short Si/Au with 350 nm and 230 nm diameter achieved a 4-fold and 12-fold amplification of induced photovoltage respect to the Si wafer.

The photovoltage for all the samples presented a non-linear behaviour with increasing laser intensity (Fig. 3.12b), with a much lower response for the n-p wafer. Notably, with the 1064 nm laser, at ultralow intensity of 0.45 $\mu W/mm^2$, it was possible to achieve 90 mV photovoltage pulses for the 230 nm NP samples, whereas the response of the Si wafer barely detectable (2.2 mV), thereby being at least 40-fold larger.

The photocurrent, were also lower for the 1064 nm laser, but the decays were substantially smaller in the nanostructured samples. The D230 nm and D350 nm NP samples exhibited 8-fold and 4-fold amplification with respect to the Si wafer for the 1064 nm laser at 22 $\mu W/mm^2$. The lower energy of the photo-carriers also can influence in the charge injection, and the current peaks showed a more Faradaic shape at this wavelength compared to 808 nm. At ultralow light levels of 2.4 $\mu W/mm^2$ the

amplification with respect to the Si wafer reached 3.6-fold and 1.6-fold for the D230 nm and D350 nm NP samples respectively.

The D350 nm sample was expected to give better opto-electric performance than the D230 nm sample with 1064 nm laser, due to its higher photo absorption around 1000 nm wavelength. However, the results showed lower response which may be caused by its too high density. As we showed before, the highest density of nanopillars (fabricated through hexagonal closed packed self-assembly) resulted in lower opto-electric performance than the middle density sample. Moreover, to properly match the hybrid-resonances to the 1064 nm laser, slightly larger diameter nanopillar (ca. 400 nm) would be needed. Therefore, higher opto-electric efficiency would be expected in Si/Au NPs fabricated by electrostatic colloidal self-assembly with 400 nm particles.

In conclusion, the short Si/Au NP D230 nm presented highly efficient photovoltage and photocurrent response, both for 1064 nm and 808 nm laser, thus exhibiting excellent opto-electric performance in the first and second biological windows at ultralow light intensities.
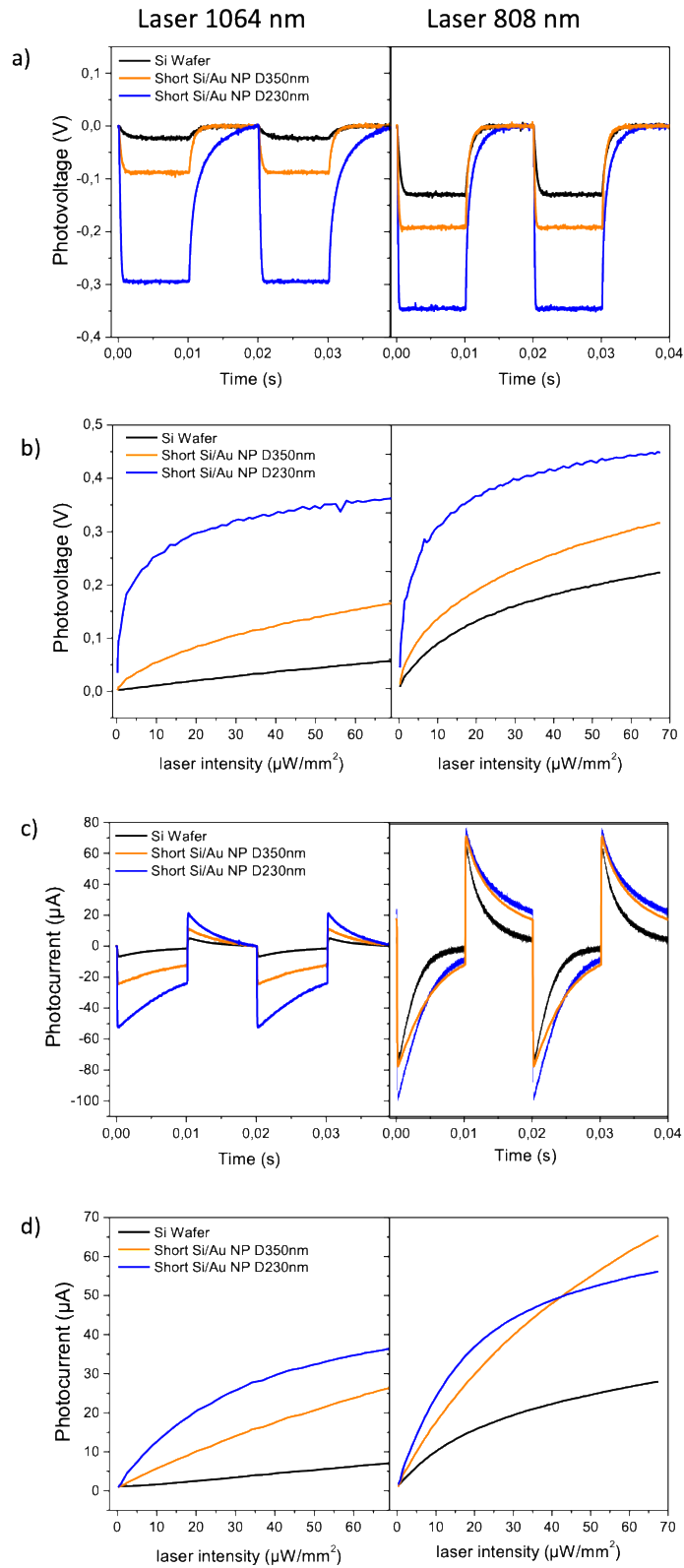
Figure 3.12. Photovoltage and photocurrent of Si wafer, short Si/Au NP D350 nm/ D230 nm, with 1064 nm and 808 nm laser. (a, c) under square laser pulses at 22 μW/mm². (b, d) Photovoltage and photocurrent dependence on laser intensity.

3.7 Cells culture on the arrays of Si/Au nanopillars

Having demonstrated the interesting opto-electronic response of the arrays of Si/Au NPs, we next further studied the cell interaction and proliferation capability on these substrates. We used HEK 293 cells for SEM and Alamar Blue assay to assess whether cells could properly adhere and proliferate on the Si/Au nanostructured surfaces. We used the HEK 293 cells due to their low maintenance, easy handing and the possibility to freeze them for storing. The HEK 293 cells used in this work are a derivative of the HEK 293 cells, which express a single type of voltage-gated K$^+$ shaker channels.
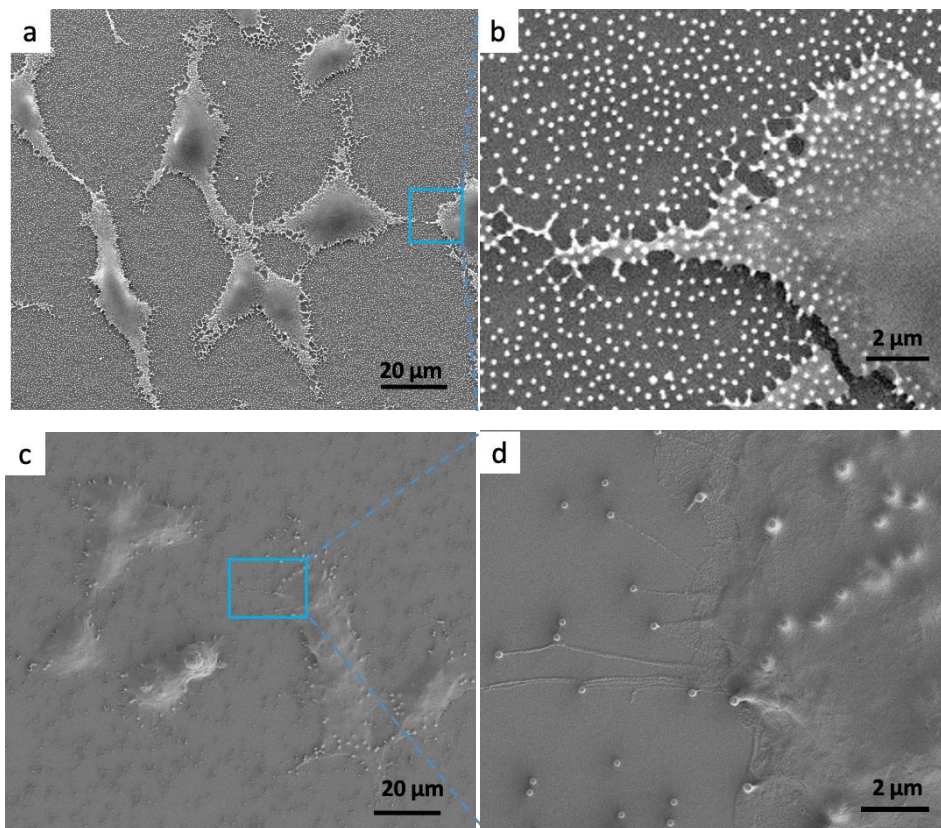
Figure 3.13. HEK 293 cells interaction with Si/Au NPs. (a) SEM image of HEK293 cells growing on middle density Si/Au NPs and (c) on low density Si/Au NPs. (b, d) zoom in images showing the cell and Si/Au NPs LD interface.

After 48 hours culture, the SEM images showed that cells perfectly grow on both the Si/Au NPs arrays with low and medium densities, and presented a flat and spread morphology. Interestingly, cells grew on the surface of NPs (Fig. 3.13a) in the medium density sample without touching the bottom Si substrate. In contrast, on low density

sample, cells could adapt to the NPs morphology and adhere simultaneously to the top of nanopillars and Si substrate (Fig. 3.13 b, c). This different adhesion could have important implications on the cell stimulation efficiency.

The fluorescence live/dead assay images confirmed that the HEK 293 cells could grow well on Si/Au NPs. After 48 hours seeding, no significant difference was observed when compared with the cells control grown on glass coverslip (Fig. 3.14 a, b, c). The capacity of cell proliferation was assessed by Alamar Blue. The results were similar between Si/Au NPs MD, Si/Au NPs LD and control glass at all time points analyzed, which further indicates the biocompatibility of the Si/Au nanopillar arrays (Fig. 3.14d).
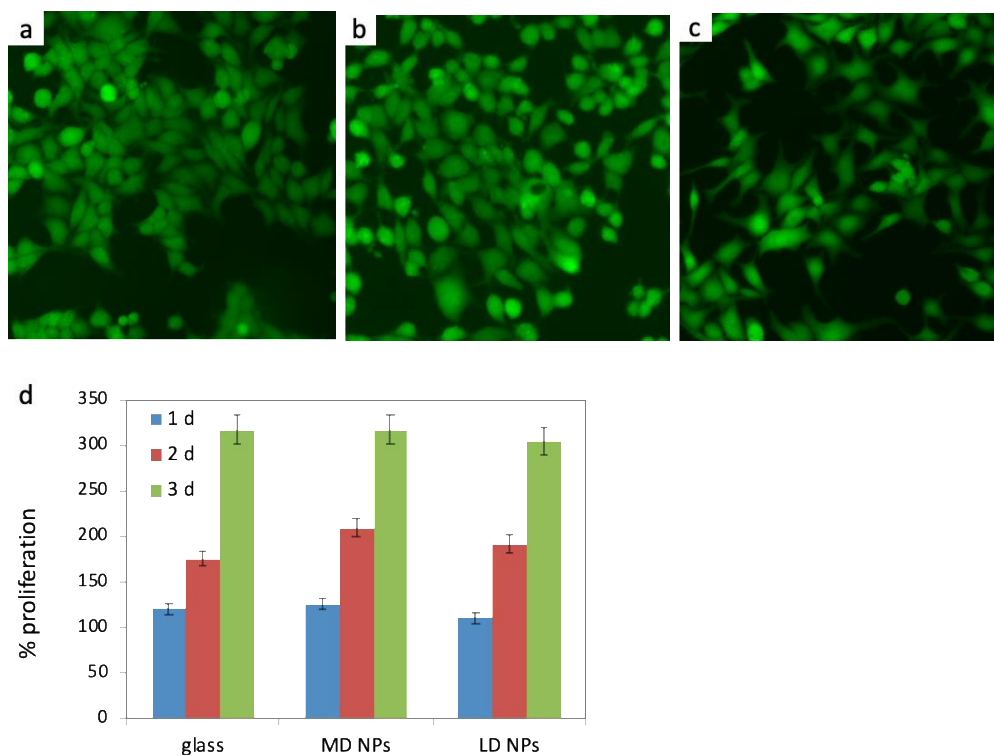

Figure 3.14. Viability of HEK 293 cells grown on Si/Au NPs. (a) Live/dead fluorescence microscope images of cells after 48 hours in culture for the control glass coverslip, (b) middle density Si/Au NPs, (c) low density Si/Au NPs. (d) Cell proliferation on glass control, middle density nanopillars, low density nanopillars by the Alamar Blue assay at days 1, 2 and 3.

3.8 Conclusions

We presented an exhaustive opto-electron-chemical analysis of Si/Au nanostructured surfaces under pulsed and sinusoidal NIR light illumination conditions. The theoretical study showed that Si nanopillar capped by Au disc on Si p-n wafer exhibited 4-fold enhancement of the light absorption at 808 nm wavelength within the first biological window, due to the excitation hybrid metal/dielectric resonances that generated an intense electromagnetic field enhancement at the p-n junction region and the Si/Au interface. The opto-electric tests proved that the short Si/Au nanopillars with middle density achieved the highest photovoltage and photocurrent at ultralow light intensities, exhibiting photovoltage of 80 mV under square laser pulses at ultralow intensity of 0.44 $\mu W/mm^2$, which was 11-fold amplified to the plain Si p-n wafer. And average photocurrent of 37 μA under square laser pulses at 20 $\mu W/mm^2$, which is 2.5-fold amplified to the plain Si p-n wafer. This excellent performance is due to its higher light absorption, more efficient photogenerated charge separation and injection. In contrast, the long Si/Au nanopillars showed the worst opto-electric performance mainly due to the fast charge recombination caused by the short-cut of the p-n junction exposed to the conductive electrolyte, and the increased number surface defects. Besides, the short Si/Au NP also gave the largest photovoltage and photocurrent for the frequency range of 1 to 5 kHz, and to maximize the photovoltage and photocurrent for efficient cell stimulation, the frequency range of 50-200 Hz could be considered.

In addition, the photocurrent of short Si/Au nanopillars with high density presented more faradaic behavior, highlighting the importance of the density of Au nanodiscs to change the current behavior from capacitive to more Faradaic. Furthermore, the direction of photovoltage can be reversed by changing the p-n junction polarity, suggesting the applicable potential of Si/Au nanopillars for hyperpolarization of cell membrane. The short Si/Au nanopillars also presented excellent opto-electric property in the second biological window, achieving photovoltage of 300 mV at intensity of 22 $\mu W/mm^2$ with 1064 nm wavelength laser, which was 11-fold higher than the Si wafer. Finally, we demonstrated the biocompatibility of the Si/Au nanopillars with HEK 293 cells. Therefore, the short Si/Au nanopillars with p-n junction are promising for the

efficient opto-electric actuation of excitable cells in deeper tissue, by employing NIR light within the first and second biological window and ultralow light intensities.

4 FeGa/ZnO nanostructures for magneto-opto-electrical cell stimulation
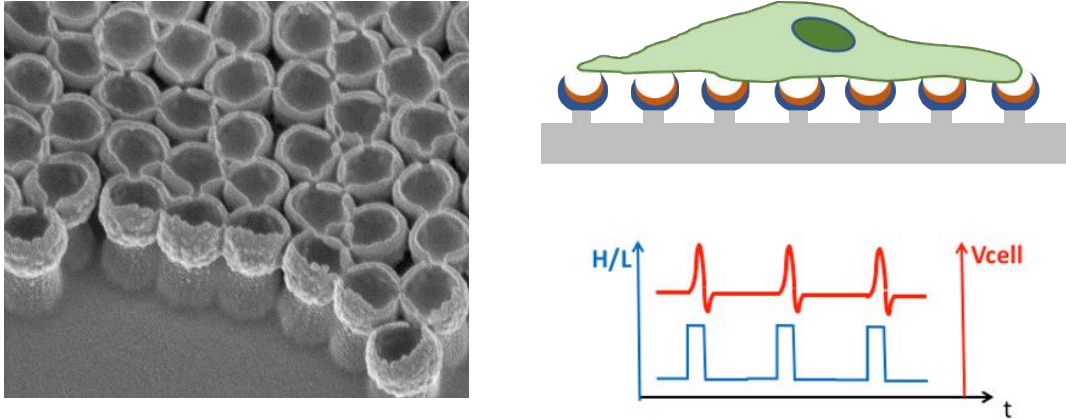
TOC Figure. (a) Patterned hollow FeGa/ZnO nanodomes integrated in PDMS film. (b) Schematic of cell stimulation with pulsed light (L) or magnetic field (H) on FeGa/ZnO nanodomes integrated in PDMS film.

Abstract:

In this chapter we present a novel nanomaterial with the aim of achieving both magnetic and optical wireless cell stimulation, based on FeGa/ZnO nanostructures. We first described the actuation principle for magneto-opto-electrical cell stimulation by arrays of FeGa/ZnO nanodomes. These arrays combine magnetostriction and efficient NIR light absorption in the FeGa layer with the piezoelectricity and pyroelectricity in the ZnO layer for generating local electric potential changes with external magnetic fields and/or NIR light pulses. Next, we analysed and optimized the magnetic behaviour of hollow ZnO/FeGa/ZnO nanodomes with different diameter and distribution, and found that the patterned D400 nm ZnO/FeGa/ZnO (20nm/40nm/20nm) nanodomes provide the best magnetization features, i.e. lowest saturation field and minimal remanence. Besides, the photothermal efficiency of the patterned D400 nm FeGa/ZnO nanodomes was tested with light illumination of 808 nm and 1064 nm wavelengths, which presented a linear temperature increase following the increase of light intensity.

In addition, we proved that the SF_6 RIE did not affect magnetic behavior of the FeGa layer, thus we removed the top ZnO layer to provide lower stiffness for larger magnetostrictive deformations. We also fabricated patterned but isolated FeGa/ZnO nanodomes enabling some degree of mechanical movement to mimic a softer extracellular matrix. Finally, we proved the biocompatibility of the FeGa/ZnO nanodomes integrated in PDMS film, by evaluating the Saos-2 cells viability cultured on the samples, including patterned FeGa/ZnO nanodomes, isolated FeGa/ZnO nanodomes, and patterned ZnO nanodomes.

Wireless magnetic stimulation is another promising non-invasive cell actuation method, which is based on the use of magneto-electric or magneto-thermal materials to remotely convert magnetic energy into electric energy to stimulate the cells. The main advantage of magnetic stimulation over optical stimulation is that the magnetic field can penetrate through the tissues without attenuation. However, there are also some significant drawbacks including poor spatial resolution of applied magnetic field and low temporal precision of the induced cell activity. Nanostructured magneto-electric or magneto-thermal devices can provide nanoscale spatial resolution for the local stimulation by magnetic field.

However, to provide more actuation versatility, strength and the possibility to design complex actuation patterns, the combination of magnetic and optic stimulation could be an interesting alternative. To achieve the magneto-opto-electric actuation, the composition and nanostructuration of the material should enable responding to optical and magnetic signals simultaneously, and transferring the delivered energy to local and quick electric stimuli.

4.1 Principle of the magneto-opto-electric cell stimulation

To attain efficient combined wireless magnetic and optical stimulation of excitable cells, we proposed a novel hybrid magneto-opto-electric nanomaterial, composed of arrays of FeGa/ZnO nanodomes (i.e., semi-shells) on soft, flexible and biocompatible substrates (Fig. 4.1). The magnetic-optic-electric energy conversion exploits the strong magnetostriction and high NIR light absorption properties of the FeGa, and the piezoelectric and pyroelectric properties of the ZnO. Therefore, this nanocomposite merges magnetic, optical and piezo/pyro-electric properties for generating local electric potential changes with external magnetic fields and NIR light pulses.
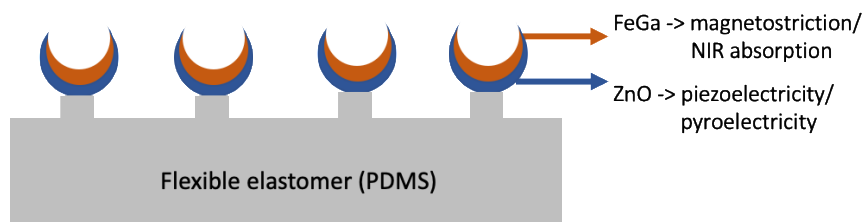

Figure 4.1. Schematic of FeGa/ZnO nanodomes integrated in PDMS film.

The **magneto-electric stimulation** is based on the combination of: i) the magnetostriction of the FeGa layer, to generate mechanical strain by the change of magnetization state, and ii) the piezoelectricity of the ZnO layer, to generate a voltage change by the mechanical deformation transferred from the FeGa layer. We have designed the magnetostrictive FeGa to present a magnetic vortex configuration in the absence of magnetic field. This feature is important to enable generating the magneto-mechanical strain when the magnetic state is transformed from the vortex to the single domain configuration. The magnetic vortex configuration is crucial to enable highly isotropic magneto-electric stimulation, as magnetic fields in any direction can break the magnetic vortex to induce the necessary mechanical strain. Moreover, once the external magnetic field is removed, the nanostructures automatically return to the vortex configuration, thus inducing another mechanical deformation and a voltage change in ZnO layer. This magnetic behaviour also permits the use of magnetic fields in only one direction (only positive or negative), thereby substantially simplifying the driving electronics.
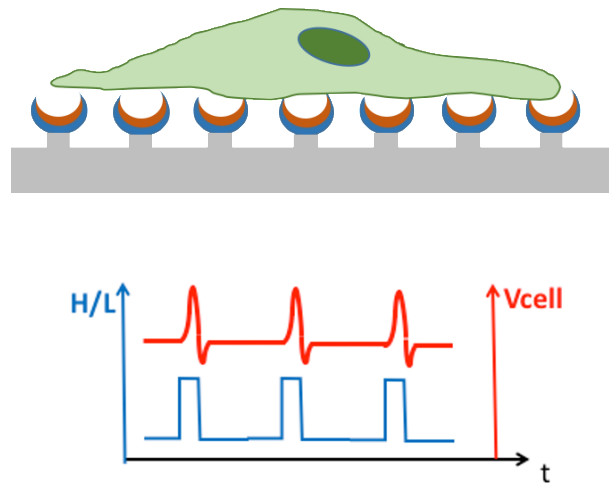

Figure 4.2. Schematic of cell stimulation with pulsed light (L) or magnetic field (H) on FeGa/ZnO nanodomes integrated in PDMS film.

On the other hand, the **opto-electric stimulation** is based on the broadband light absorption of FeGa layer in the NIR range, which can be used to generate a local temperature increase. This temperature increase in the nanostructures can induce a

mechanical stress between the FeGa and ZnO layers due to their different thermal expansion coefficients (i.e., bimetallic effect), which can trigger the piezo-electric actuation of the ZnO. Besides, the temperature rise of the ZnO can also induce the pyroelectric response of ZnO layer to generate the electrical actuation.

Therefore, the FeGa/ZnO nanodomes integrated in PDMS film have the potential to act as efficient implantable magneto-opto-electric actuators of excitable cells, for generating stimulation with pulsed light or magnetic field as shown in Fig. 4.2. When applying magnetic(H) or light (L) pulses, the FeGa/ZnO nanodomes can accordingly induce voltage change to change the cell membrane potential (V_{cell}) for the cell excitation.

4.2 Fabrication of FeGa/ZnO nanodomes integrated in PDMS film

To analyse the capacity to combine magnetic and optical electric cell stimulation, we first fabricated ZnO/FeGa/ZnO nanodomes with different diameters and densities integrated in PDMS film. Our first goal is achieving a magnetic vortex configuration in which the necessary amplitude of magnetic field to break the vortex and saturate the magnetization of the sample is minimized. Therefore, we fabricated ZnO/FeGa/ZnO nanodomes arrays of different diameters, geometric distribution and FeGa thickness.

As shown in Fig. 4.3, the fabrication process started from the self-assembly of nanospheres. We employed the electrostatic colloidal self-assembly method to prepare the separated D200 nm and D400 nm polystyrene nanospheres on Si wafer, with randomly ordered but homogeneous distribution on the whole wafer. On the other hand, the patterned D400 nm and D500 nm nanospheres arrays were prepared by the hexagonal close-packed self-assembly technique, as described in Chapter 2. Then the ZnO/FeGa/ZnO layers of 20/40/20 nm in thickness were sequentially sputtered on the wafer with nanospheres. The configuration with double ZnO layer was also selected to protect the FeGa layer during the RIE etching. Next, liquid PDMS was deposited and cured on the wafer, to fully transfer the sputtered nanosphere array to the PDMS. The PDMS film with integrated nanospheres was then peeled off.

Finally, to offer cells direct contact to the active ZnO/FeGa/ZnO structures and to enable their free magneto/opto-mechanical deformation, we generated hollow

ZnO/FeGa/ZnO nanodomes structures by SF_6 RIE to simultaneously remove the polymer nanospheres and part of the PDMS. This process exploits the extremely low etching rate of ZnO under SF_6 RIE. Therefore, this etching step yields hollow ZnO/FeGa/ZnO structures on PDMS nanoposts (Fig. 4.3).

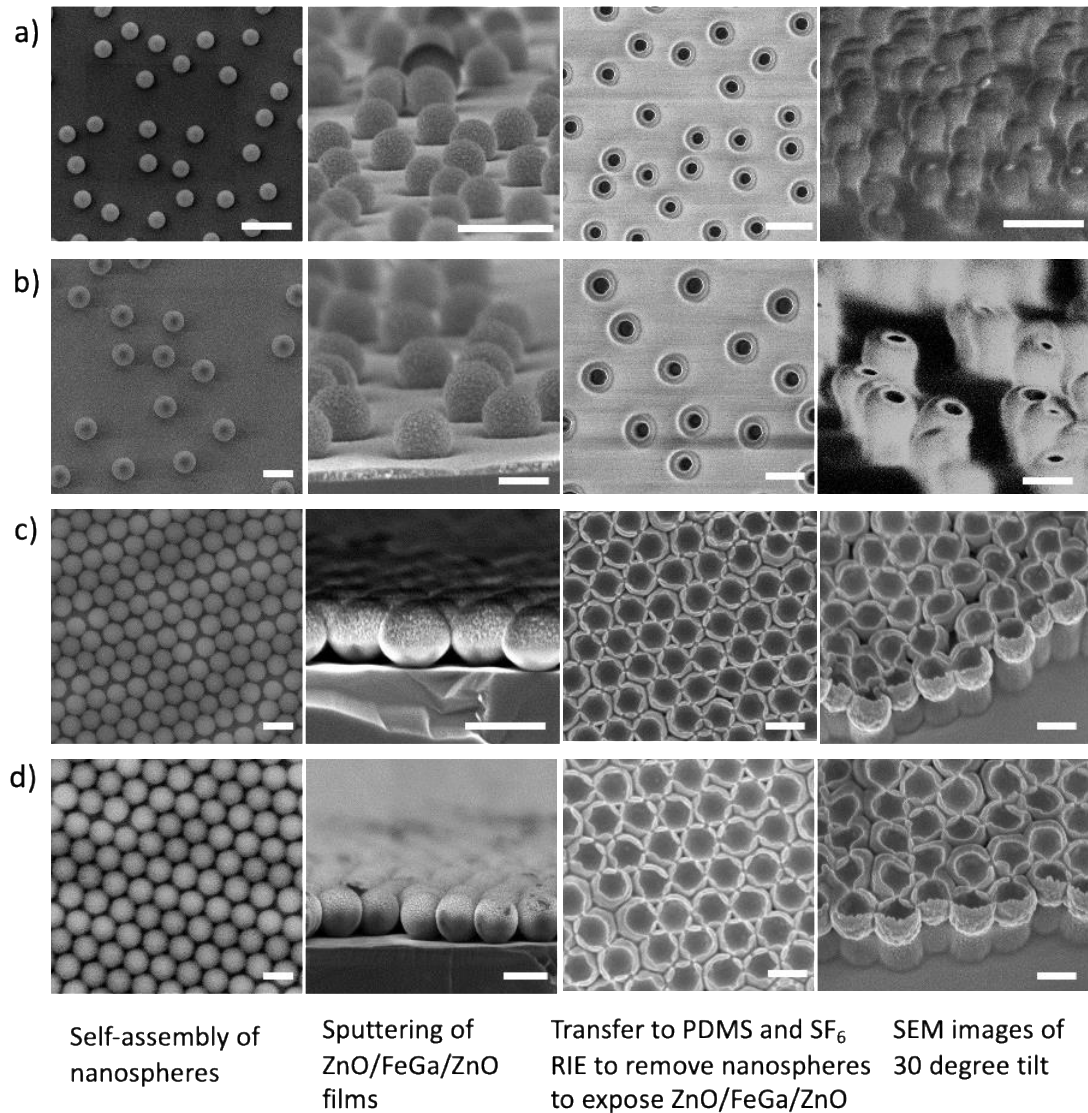| Self-assembly of nanospheres | Sputtering of ZnO/FeGa/ZnO films | Transfer to PDMS and SF_6 RIE to remove nanospheres to expose ZnO/FeGa/ZnO | SEM images of 30 degree tilt |

Figure 4.3. SEM images showing the fabrication process of the hollow ZnO/FeGa/ZnO nanodomes integrated in PDMS film with different diameters and densities. (a) D200 nm separated nanodomes. (b) D400 nm separated nanodomes. (c) D400 nm patterned nanodomes. (d) D500 nm patterned nanodomes. Scale bar: 500 nm.

4.3   Magnetic characterization and optimization

We tested the magnetic properties of the different ZnO/FeGa/ZnO (20nm/40nm/20nm) nanodomes arrays integrated in the PDMS film by VSM, including separated D200nm and D400nm nanodomes, patterned D400nm and D500nm nanodomes, and patterned D500nm nanodomes in which the FeGa layer thickness was reduced to 30nm.
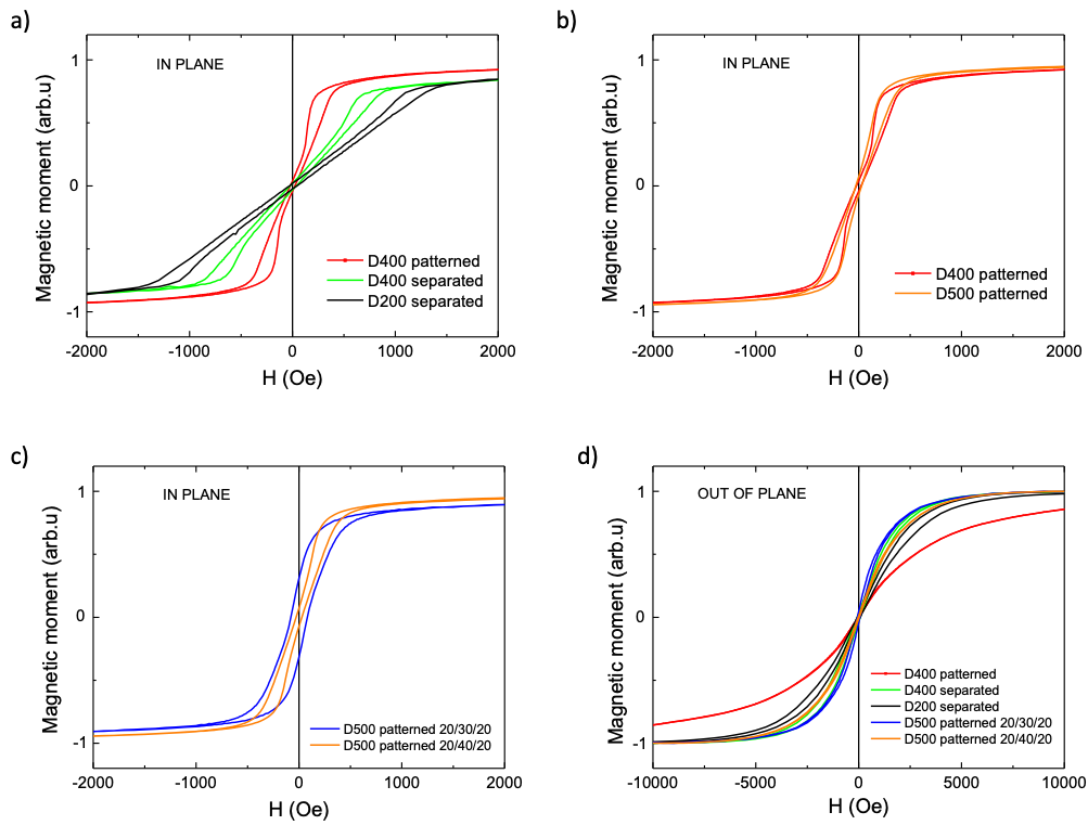
Figure 4.4. Vibrating sample magnetometer magnetization loops of ZnO/FeGa/ZnO nanodomes arrays with different diameters and densities integrated in PDMS film, for in-plane and out-of-plane applied fields. (a, b) ZnO/FeGa/ZnO of 20nm/40nm/20nm in thickness. (c) D500nm patterned nanodomes with ZnO/FeGa/ZnO layers of 20nm/40nm/20nm and 20nm/30nm/20nm in thickness. (d) Magnetization loops for out-of-plane applied fields.

As can be observed in Fig. 4.4a, the in-plane loops all the samples with 40 nm thick FeGa layer showed a vortex-shape magnetization reversal loop. Particularly, the

patterned D400 nm nanodomes needed the lowest magnetic field (around 500 Oe) to saturate the magnetization, followed by the separated D400 nm nanodomes. In contrast, the separated D200 nm nanodomes presented a much more tilted loop, thereby needing the highest magnetic field (around 1500 Oe) to saturate the magnetization. The patterned D500nm nanodomes showed similar magnetization reversal loop with respect to the patterned D400nm nanodomes (Fig. 4.4b).

In contrast, the patterned D500nm ZnO/FeGa/ZnO (20nm/30nm/20nm) nanodomes showed a single domain loop with substantial remanence (Fig. 4.4c). Therefore, the thickness of FeGa layer should be larger than 30 nm to achieve a vortex magnetic state in this range of nanospheres diameters. For all the samples, the magnetic fields required to saturate the magnetization out of plane were much higher than those in plane (Fig. 4.4d). Therefore, the magnetization in all the samples was preferentially in plane.

In conclusion, the patterned D400 nm and D500 nm ZnO/FeGa/ZnO (20nm/40nm/20nm) nanodomes provided the best magnetization features, i.e. lowest saturation field and minimal remanence. This enables the magnetic stimulation with just positive (or negative) magnetic pulses of moderate intensity, which greatly simplifies the driving electronics. Which motivated focusing on these D400 nm nanodomes arrays for the magneto-opto-electric assays and cell stimulation.

4.4   Optimization of the FeGa/ZnO fabrication

To simplify the fabrication and provide nanostructures with lower stiffness for enabling larger magnetostrictive deformations, we also tried to eliminate one of the ZnO layers. To ensure the integrity of the FeGa layer, we studied the effect of SF_6 RIE on the magnetization reversal loops before and after removal of the polystyrene spheres by SF_6 RIE. The VSM results gave almost identical magnetization loops (Fig. 4.5), thus the SF_6 RIE did not significantly etch and affect the magnetic behaviour of the FeGa layer.
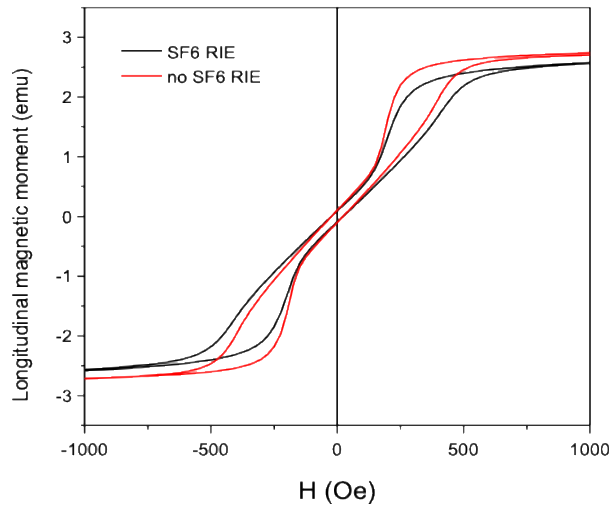
Figure 4.5. Magnetization reversal loops of patterned D400 nm FeGa/ZnO nanodomes before and after removal of the polystyrene spheres by SF_6 RIE.

Representative images of the fabrication process of patterned D400 nm FeGa/ZnO 40 nm/20 nm nanodomes are presented in Fig. 4.6 (a-d). The combination of the patterned hexagonal close-packed self-assembly and the low directionality of the sputtering deposition gave rise to peculiar features in the hollow structures. In the case of seperated particles, the sputtering yielded a very uniform coverage on the nanosphere, in which almost the whole sphere was covered by material, except the region that was in direct contact to the wafer (see Fig. 4.3 a-b). In contrast, when the particles are touching each other, there are regions of the spheres that are inaccessible to the sputtered material (as schematized in Fig. 4.6e.), which resulted in opening points (as marked with the red circle in Fig. 4.6c) between the close-packed hollow FeGa/ZnO nanodomes after removing the nanospheres by SF_6 RIE.

a — Colloidal lithography of D400 nm nanospheres

b — Sputtering of FeGa 40 nm/ ZnO 20 nm films

c — transfer to PDMS and SF$_6$ RIE to remove nanospheres to expose FeGa/ZnO

d — 30 degree tilted SEM image

e)

f)
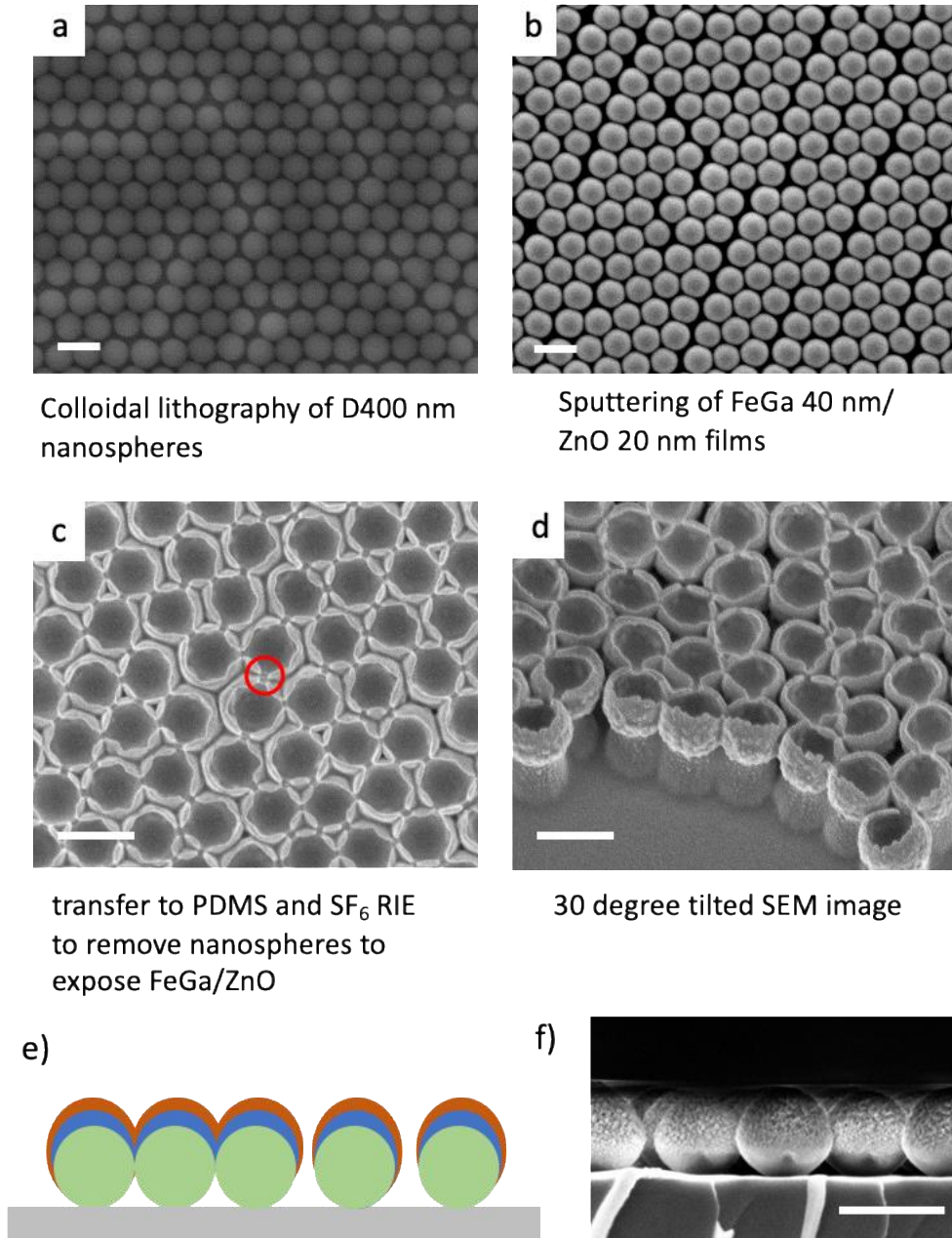
Figure 4.6. (a-d) SEM images showing the fabrication process of patterned D400nm FeGa/ZnO nanodomes. Scale bar: 500 nm. (e) Schematic of sputtered FeGa/ZnO layers structure on the connected nanospheres and disconnected nanospheres. (f) SEM image of the disconnected nanospheres with sputtered FeGa/ZnO layers.

Another interesting point of the sputtered FeGa/ZnO layers over the nanospheres was to assess if the deposited layer is continuous, which could be helpful for the magneto-opto-electric characterization of the layer. In order to prove this, we performed EDX

mapping for the sample (Fig. 4.7). As the carbon C signal mapping shown, it is clear that the polystyrene nanospheres were close-packed and touching each other. Consequently, the FeGa and ZnO layers were continuous at the touching points of the nanospheres. Besides, the Si signal mapping showed the gaps between the disconnected nanospheres after sputtering FeGa/ZnO layers, which allowed the SF_6 RIE of PDMS nanoposts.
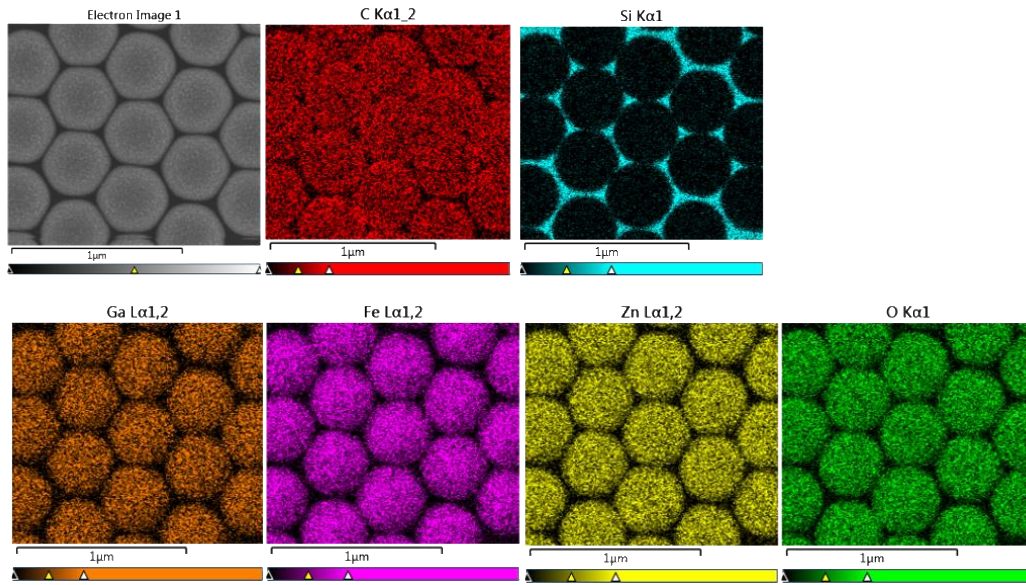
Figure 4.7. Energy dispersive X-ray (EDX) mapping images for C, Si, Ga, Fe, Zn, O signals of FeGa/ZnO layers over patterned nanospheres on Si wafer.

In order to achieve a more homogeneous coverage and to enable some degree of mechanical movement to mimic a softer extracellular matrix, we also fabricated patterned but isolated FeGa/ZnO nanodomes integrated in PDMS film. The fabrication process is shown in Fig. 4.8. We first used O_2 RIE to reduce the size of the close-packed nanospheres from D400 nm to around D330 nm, then sputtered the FeGa/ZnO layers of 40 nm/20 nm on the disconnected nanosphere array. As schematized in Fig. 4.7a, the FeGa/ZnO layers could reach the sidewalls of all the nanospheres, leading to a more homogeneous coverage over the nanospheres. Furthermore, PDMS nanoposts could be produced by SF_6 RIE through the gaps between nanospheres.
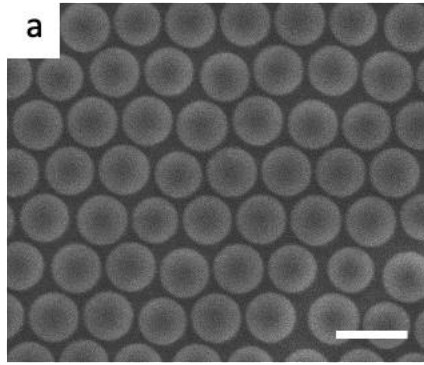
O2 RIE to reduce nanospheres size   Sputtering of FeGa/ZnO films
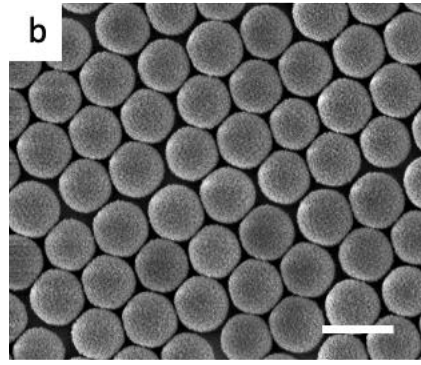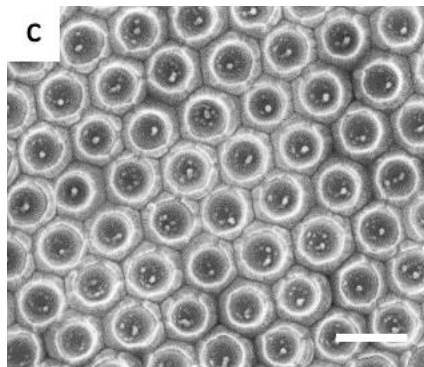
transfer to PDMS and SF$_6$ RIE
to remove nanospheres to
expose FeGa/ZnO
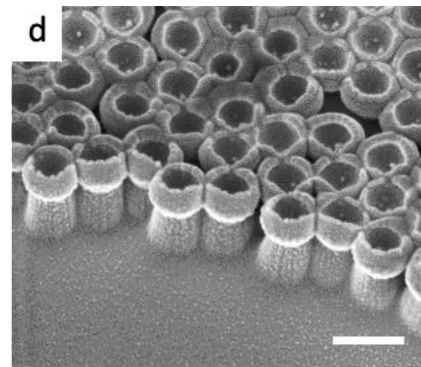
30 degree tilted SEM image

Figure 4.8. SEM images showing the fabrication process of isolated FeGa/ZnO
40nm/20nm nanodomes integrated in PDMS film. Scale bar: 500 nm.

In addition, as the piezoelectricity of the ZnO layer may also be triggered by the self-moving cells, we also fabricated patterned D400 nm ZnO nanodomes integrated in PDMS film as the control sample (Fig. 4.9). Due to the sputtered ZnO layer thickness was only 20 nm, it was quite fragile, especially the part at the sidewalls of nanospheres. As a result, after the SF$_6$ RIE, only halfsphere-shaped ZnO nanodomes were left.
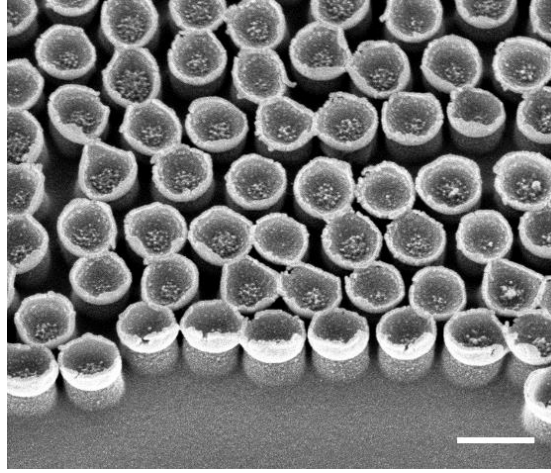
Figure 4.9. SEM image of patterned D400 nm ZnO nanodomes integrated in PDMS film. Scale bar: 500 nm.

4.5   Photothermal effect of FeGa/ZnO nanodomes

Taking advantage of the NIR absorption ability of FeGa layer and the pyroelectricity of ZnO layer, FeGa/ZnO nanodomes integrated in PDMS film can also be promising to achieve efficient opto-electric actuation with NIR light pulses.

We first carried out FDTD simulations to analyze the absorption spectrum of the FeGa/ZnO nanodomes before and after removal of the polystyrene spheres and surrounding PDMS. We assumed that the metal is Fe, due to the lack of good optical constants for the FeGa alloy, and a constant refractive index in the ZnO layer of 1.95 in the 600 nm to 1100 nm range. The thickness of the Fe and ZnO layers were the same as the experiments, i.e. 40 and 20 nm, respectively. Interestingly, only 40 nm of the nanostructured metal provides a very intense and broadband absorption. The arrays of D400nm Fe/ZnO nanodomes with polystyrene nanospheres showed absorption of about 80% in the range from 600 nm to 1100 nm (Fig. 4.11a). After removal the nanospheres, the light absorption decreased from 87% at 600 nm wavelength, but exhibited a steeper reduction up to 75% at 1100 nm wavelength.

To prove this broadband absorption, we studied the heating efficiency of the patterned hollow D400nm FeGa/ZnO nanodomes integrated in PDMS film, using 808 nm and 1064 nm wavelength laser illumination, by checking the temperature increase as a function of the laser intensities. We chose the NIR light wavelengths within the first and second biological windows, for achieving higher penetration depth in tissues.

Particularly, for the longer wavelength 1064 nm light, a higher intensity is allowed for keeping safe irradiation. As can be observed in Fig. 4.11b, the temperature increase showed a linear behavior following the laser intensity increase. Besides, at the same laser intensity, the temperature increase with 808 nm laser was a bit higher than that with 1064 nm laser, due to the slightly higher absorption at 808 nm wavelength than that at 1064 nm, as expected from the FDTD simulations.
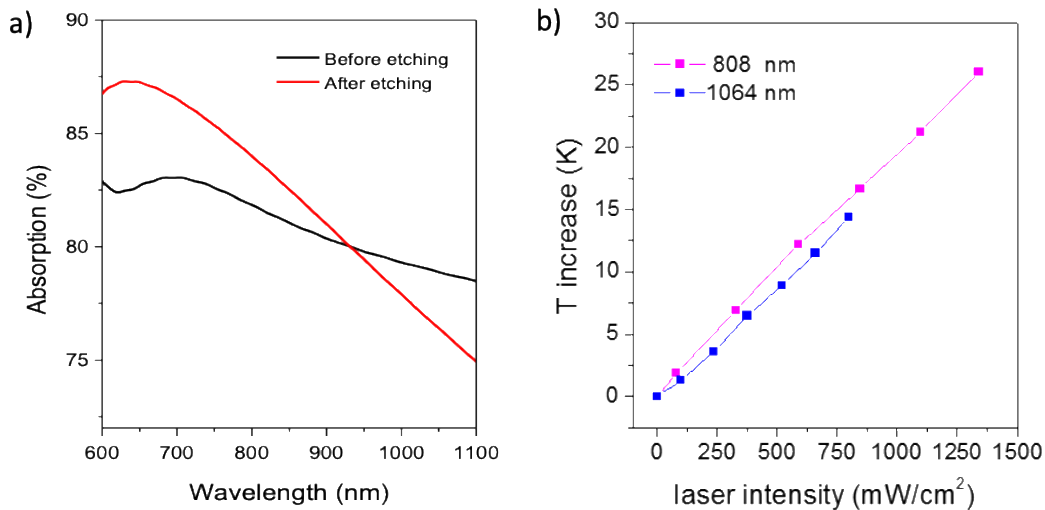
Figure 4.11. (a) FDTD absorption spectra of D400nm Fe/ZnO nanodome arrays with/without nanospheres (before/after SF_6 etching). (b)Temperature increase of patterned D400nm FeGa/ZnO nanodomes integrated in PDMS film as a function of laser intensities of 808 nm and 1064 nm wavelength laser.

4.6 Saos-2 cells interaction with FeGa/ZnO nanodomes

In order to prove the biocompatibility of the FeGa/ZnO nanodomes integrated in PDMS films, we evaluated the Saos-2 cells (human osteosarcoma cell line) viability cultured on the samples, including patterned FeGa/ZnO nanodomes, patterned-isolated FeGa/ZnO nanodomes, and patterned ZnO nanodomes integrated in PDMS film.

As initial experiment, we did the SF_6 RIE for 3 minutes to remove the polystyrene nanospheres on the FeGa/ZnO nanodomes, and we found that the adhesion of

FeGa/ZnO nanodomes on PDMS film was not good, as the nanodomes detached from the substrate during the cell culture procedures. As shown in the EDX analysis in Fig. 4.12-b, clear Ga, Fe, and Zn peaks on the EDX spectrum were present before the cell culture. However, the peaks disappeared after seeding the cell (Fig. 4.12-d). This indicated that the FeGa/ZnO nanodomes had already detached from PDMS film during the steps of cell seeding. This might be due to the overetching of the PDMS nanopost below the nanodomes, which was thinner and longer with SF_6 RIE for 3 minutes, thus leading to weak adhesion of the FeGa/ZnO nanodomes to the PDMS nanoposts. Therefore, we reduced the SF_6 RIE time to 2.5 minutes.

We checked the adhesion of the FeGa/ZnO nanodomes again after cell culture by EDX, and the results clearly showed the Ga, Fe, and Zn peaks (Fig. 4.12-f). Therefore, small reduction of the SF_6 etching time enabled the FeGa/ZnO nanodomes becoming stable with good adhesion to the PDMS film.
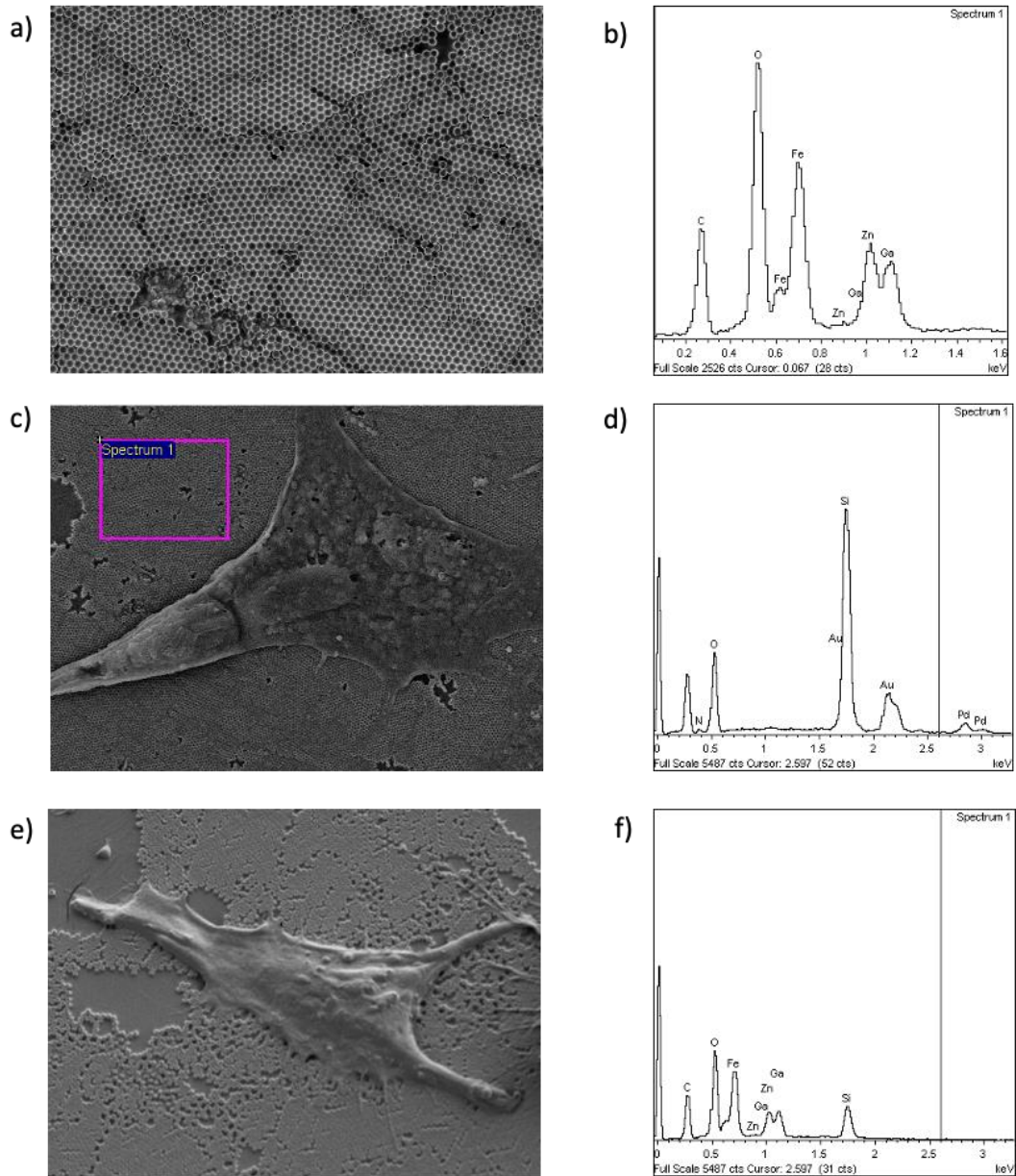
Figure 4.12. SEM images of FeGa/ZnO nanodomes on PDMS film and corresponding EDX spectrums, for SF$_6$ RIE of 3 mins sample before cell culture (a, b) and after cell culture (c, d), and SF$_6$ RIE of 2.5 mins sample after cell culture (e, f).

Next, we evaluated the Saos-2 cells viability cultured on patterned FeGa/ZnO nanodomes, isolated FeGa/ZnO nanodomes, and patterned ZnO nanodomes integrated in PDMS film. We used cell tracker green CMFDA dye assay to check the live cells, SEM to check cell morphology, and Alamar Blue assay to test cell proliferation.
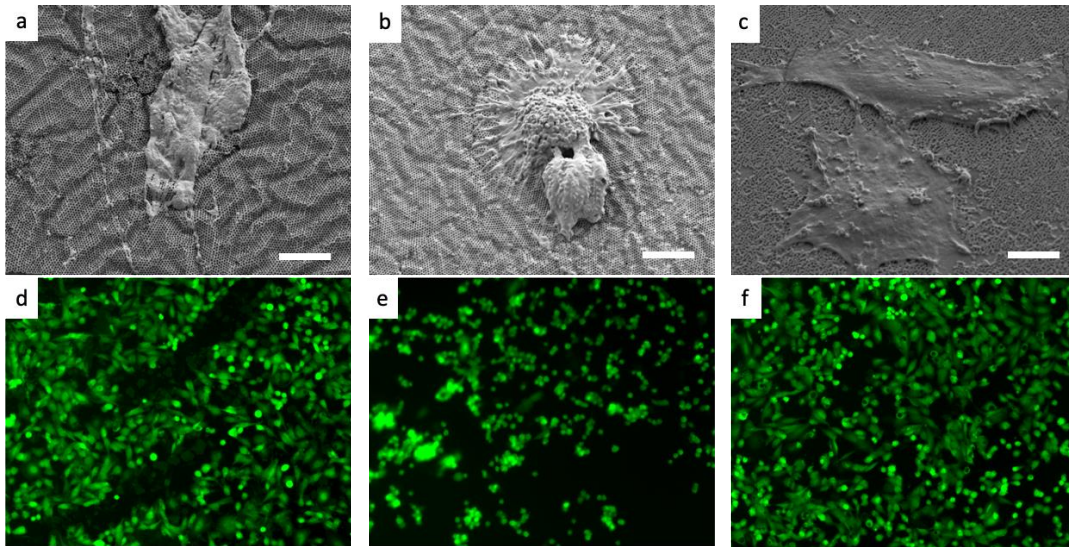
Figure 4.13. SEM images and fluorescence microscope images of Saos-2 cells after 48 hours in culture on patterned FeGa/ZnO nanodomes (a, d), isolated FeGa/ZnO nanodomes (b, e), and patterned ZnO nanodomes (c, f) integrated in PDMS film. Scale bar: 5 μm.

As shown in Fig. 4.13, after 48 hours in culture, the Saos-2 cells on the patterned FeGa/ZnO nanodomes and patterned ZnO nanodomes presented a flat and extended topography (Fig. 4.13 a, c)., indicating good adhesion to the substrate. The cells could grow well on these two samples as can be observed from the fluorescence microscope images (Fig. 4.13 d, f). In contrast, the cells cultured on the isolated FeGa/ZnO nanodomes showed round shape (Fig. 4.13 b, e), which means they could not attach well to the substrate. The bad adhesion may affect the cell metabolic activity and the efficiency of electric actuation by FeGa/ZnO nanodomes. This may be due to the very thin and fragile sputtered FeGa/ZnO layers at the rims of the hollow structured after the SF_6 RIE. This sharp structure might be fractured, detached and internalized by the cells, which may affect their viability.

5. Conclusions

This thesis presented two types of nanomaterials for enabling wireless cell stimulation based on opto-electric and magneto-opto-electric nanostructures, to achieve effective energy conversion from optical or magnetic signals to electrical outputs. In the optical excitation we focused in lights within the NIR biological windows that can penetrate deeper in tissues. These nanomaterials are promising for advanced therapeutic approaches based on electrically stimulation of excitable cells. The main results and conclusions reached are described below.

We proposed a simple, robust and cost-effective strategy for the fabrication of Si/Au nanostructured system for wireless opto-electric stimulation. The rational design and theoretical optical analysis of Si/Au nanostructures showed that the Si nanopillars capped by Au discs on Si wafer exhibit remarkably enhanced light absorption in the NIR, due to the excitation of hybrid metal/dielectric resonances, enabling large amplification of the electromagnetic fields at the Si/Au interface and at the Si nanopillars.

The experimental opto-electric analysis of the Si/Au nanostructures showed that the short Si/Au nanopillars, which only expose the n-region to the electrolyte, provided the highest photovoltage of 80 mV at ultralow light intensity of 0.44 μW/mm^2 using 808 nm light illumination, which is 11-fold higher than the plain p-n Si wafer. This intensity is almost 3 orders of magnitude lower than the smallest intensity reported for cell stimulation. At ultra-low light level, the short Si/Au nanopillars also exhibited the highest photocurrents, ca. 2.5-fold higher than the plain Si p-n wafer. This excellent performance is mainly due to the higher light absorption, more efficient photogenerated charge separation and injection into the electrolyte. In contrast, although the long Si/Au nanopillars showed theoretically the highest absorption, they presented the worst opto-electric performance. This reduction is attributed to the fast charge recombination caused by the p-n junction short-cut exposed to the conductive electrolyte, and the increased number of surface defects. In addition, the short Si/Au nanopillars with higher density presented more faradaic photocurrents, thus highlighting the contribution of the Au discs to change the current behavior from capacitive to faradaic.

Conclusions

By reversing the direction of the p-n junction, the photovoltage polarity could be inverted accordingly, keeping similar photovoltages and photocurrents for short Si/Au NPs, thus indicating their potential also for cell membrane hyperpolarization.

The frequency analysis with sinusoidal light showed that the short Si/Au nanopillars provided the largest photovoltage and photocurrent in the frequency range of 1 to 50 kHz. To maximize the photovoltage and photocurrent for efficient cell stimulation, the frequency range of 50-200 Hz could be utilized.

The short Si/Au nanopillars also presented excellent opto-electric response in the second biological window with 1064 nm wavelength laser, achieving photovoltage of 90 mV at an ultra-low intensity of 0.45 $\mu W/mm^2$, which was 40-fold higher than that in the plain Si wafer.

Finally, the cell viability assays demonstrated the biocompatibility of the Si/Au nanopillars. Therefore, the Si/Au nanopillar devices are promising for efficient opto-electric cell stimulation with ultralow light intensity within the first and second NIR biological window.

The second main block of this thesis was devoted to the development of FeGa/ZnO nanostructures on elastomeric substrates for magneto-opto-electrical cell stimulation. We proposed and fabricated patterned hollow FeGa/ZnO nanodomes structure integrated in soft, flexible and biocompatible PDMS film. This hybrid nanomaterial enables combining the magnetostriction and efficient NIR light absorption in the nanostructured FeGa layer with the piezoelectricity and pyroelectricity in the ZnO layer for generating local electric potential changes by external magnetic fields and/or NIR light pulses simultaneously. The magnetic characterization revealed that the the patterned D400 nm ZnO/FeGa/ZnO (20nm/40nm/20nm) nanodomes provided the best magnetization features, i.e. lowest saturation field and minimal remanence. This enables the magnetic stimulation with just positive (or negative) magnetic pulses of moderate intensity, which greatly simplifies the driving electronics. In addition, the SF_6 RIE did not affect the magnetic behavior of the FeGa layer, thus allowing the removal of the top ZnO layer to provide nanostructures with lower stiffness for larger magnetostrictive deformations.

The FDTD simulations predicted an intense broadband absorption over 80% with just 40 nm of metal. In particular, light absorption of the simulated arrays of D400 nm

Fe/ZnO nanodomes at 808 nm wavelength was approximately only 10% higher than that at 1064 nm wavelength. Confirming these results, the FeGa/ZnO layers exhibited high photothermal efficiency that was only slightly higher at 808 nm than at 1064 nm laser illumination. Finally, we demonstrated the cell viability cultured on the FeGa/ZnO nanodomes integrated in PDMS film. As the illumination in the second biological window enables the use of higher intensities, these nanostructures have a high potential for opto-electric stimulation in relatively deeper tissue.

6. Future work

In the future, there is still much work to be completed to fully demonstrate the opto-electric and magneto-opto-electric cell nanostimulation in vitro and in vivo. The in vitro demonstrations were planned during the first semester of 2020, but they had to be stopped by the COVID lock-down. In this section we first describe the short-term research tasks that were planned, and will try to be done after deposition of this thesis manuscript, together with the main progress so far. Then the long-term perspectives of these technologies are presented, which are mainly related to show the capacity of this or related nanomaterials for cell stimulation in vivo.

6.1 short-term work plan

The next activities are planned:

1. Demonstration of the short Si/Au nanopillars opto-electrical actuation on HEK 293 cells in vitro, by the patch clamp system integrated with the 808/1064 nm laser controller.

For this demonstration, we have already manufactured a special holder (Fig. 1) for cell culture on the Si/Au nanopillars adapted to the patch clamp, and we proved that cells can grow well on it. With this configuration, we will try to stimulate the HEK 293 cells and detect the light induced cell membrane potential change by the patch-clamp system.
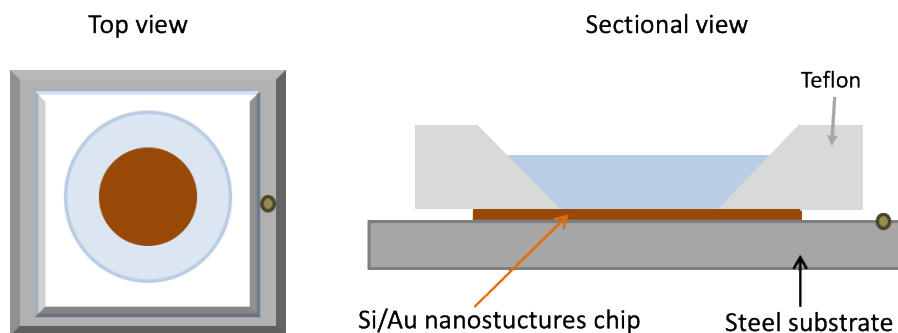
Fig. 6.1. Schematic of the holder for cell culture.

In addition, we have optimized the parameters to make the glass micropipettes necessary for patch-clamp assays, by a DMZ-Universal-Electrode-Puller. The tip of the micropipette is well controlled, with a diameter around 2 μm and smooth edges (as shown in Fig. 6.2). This is critical for forming the giga-seal when touching and clamping the cell membrane. We have been able to position the micropipette precisely to touch cell membrane by the patch clamp micromanipulator.
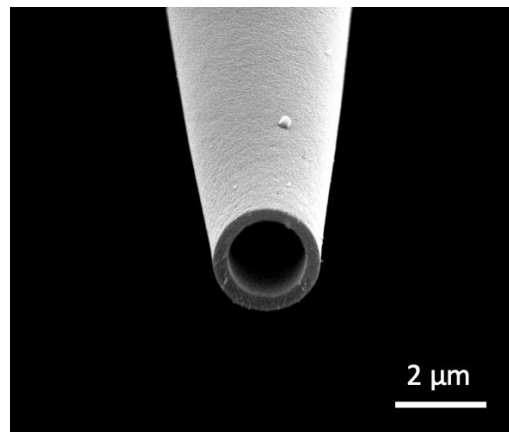
Fig. 6.2. SEM image of the tip of micropipette.

We have also prepared the intracellular and extracellular solutions required for patch-clamp test, the concentration of each compound is shown below. Both solutions were dissolved in milli-Q water and adjusted to pH 7.4 using NaOH and HCl. The osmolarity was adjusted to 355 mOsmol/kg for the intracellular solution, and 335 mOsmol/kg for the extracellular solution using D-Glucose.

Intracellular solution

compound	Concentration (mM)
KCl	140
HEPES	5
EGTA	1

Extracellular solution

compound	Concentration (mM)
NaCl	135
KCl	5
$CaCl_2$	1.8
$MgCl_2$	1
HEPES	5

In addition, we have integrated the laser controller in the patch-clamp system (as shown in Fig. 6.3). Our next objective is demonstrating the stimulation of cells grown on the short-Si/Au nanostructures, and detect the cell membrane potential change induced by ultra-low NIR light pulses by the patch-clamp system, to prove that the Si/Au nanostructures are effective for wireless opto-electric cell stimulation in vitro.
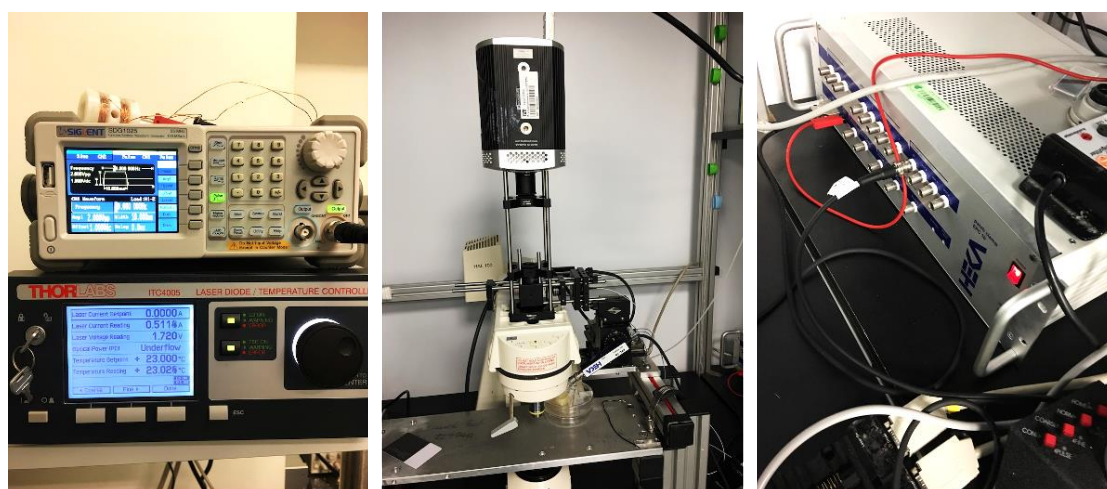
Waveform generator and laser controller   Laser allignment with microscope   Patch clamp amplifier

Fig. 6.3. Photographs of the laser controller integrated in the patch-clamp system.

2. **Magneto-electric performance tests for FeGa/ZnO nanodomes**.

We have fabricated the FeGa/ZnO nanodomes on Al substrate (Fig. 6.4) instead of the PDMS film, to provide a conductive substrate for recording the magneto- and photo-generated voltages/currents.
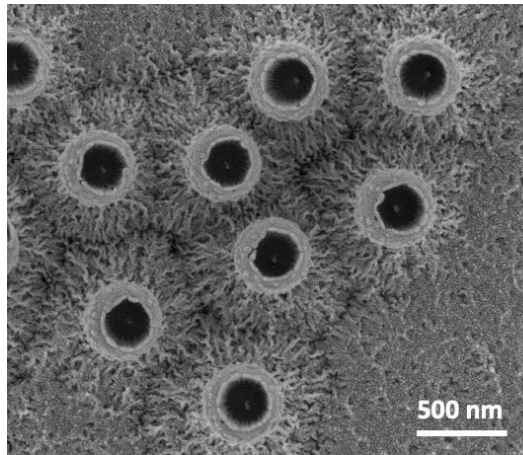
Fig. 6.4. SEM image of FeGa/ZnO nanodomes on Al substrate.

Besides, in collaboration with the company BlackHand Dynamics we have developed a magnetic pulse generator, based on a high permeability ferrite transformer with 26 turns and a gap of 1 cm. The amplitude of the magnetic pulses that can be achieved with this set up is 50 mT, with a frequency of 100 Hz and a duty cycle of 50%, which would be sufficient for the saturation of the FeGa layer on the nanodomes. A schematic of the system is shown below (Fig. 6.5).
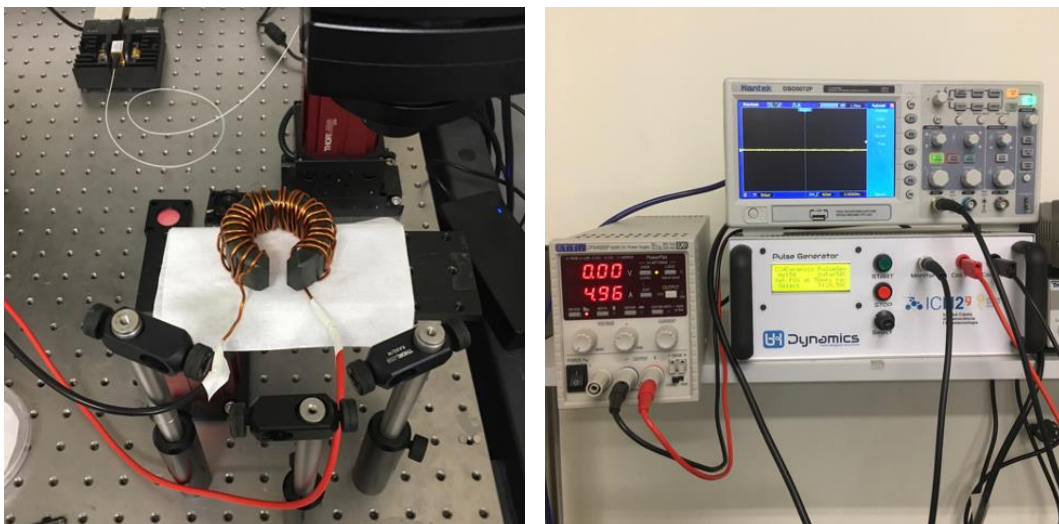
Fig. 6.5. Photographs of the magnetic pulse generator set up.

The Al substrate sample will be put inside a PMMA pool, which is positioned in the gap, so the magnetic field is parallel to the nanostructure, for the aim of actuating the in-plane magnetization. The PMMA pool will be filled with saline solution, together with a Pt wire and the Al substrate as reference and working electrodes, respectively. We have edited the Labview scripts for recording the amplitude of the generated voltages.

3. Demonstration of the magneto-opto-electrical actuation of the FeGa/ZnO nanodomes in PDMS film on Saos-2 cells in vitro, by detecting the intracellular calcium peaks generated by the opening of voltage-gated calcium channels.

We will first integrate the magnetic field pulse generator and the NIR laser controllers in a fluorescence microscope to image the Ca^{2+} peaks.

4. Analysis of ZnO/FeGa nanoleaves for magneto-opto-electrical cell stimulation

We are considering these nanostructures as an alternative to the FeGa/ZnO nanodomes, for maximizing the piezo/pyro-electric response by improving the crystalline structure in the ZnO layer. We have synthesized monocrystalline ZnO nanoleaves on Al/Au (200 nm/50 nm) films through hydrothermal synthesis method, as shown in Fig. 6.6. We have sputtered FeGa layer of 40 nm and 80 nm on the ZnO nanoleaves.

Fig. 6.6. SEM image of ZnO nanoleaves on Al/Au films.

We will first study the magnetization reversal loops by VSM, the optical absorption and the photothermal response. Finally, we will study the magneto-opto-electrical performance. If the results are successful, we will demonstrate the for wireless cell stimulation on Saos-2 cells by the detection of the Ca^{2+} peaks.

6.2 Long-term work plan

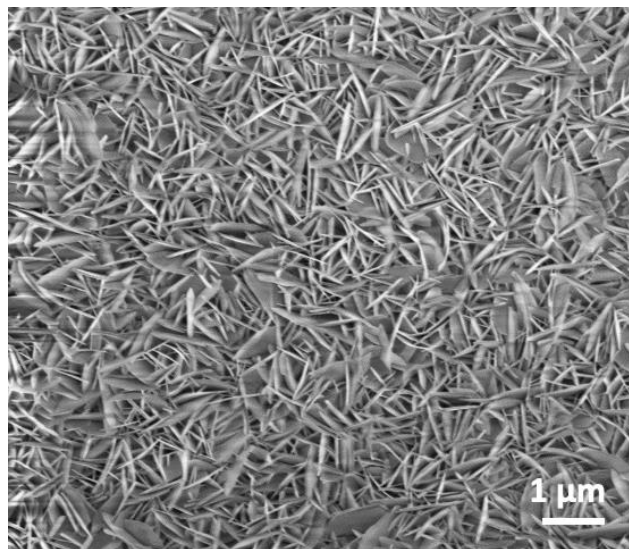In order to apply these nanostructures for cell stimulation in vivo, it is necessary to fabricate the Si/Au nanostructured layer on flexible substrates for implantation or free colloidal nanostructures for injection in vivo. Besides, surface modification of these nanostructures should be performed for targeted cell stimulation. Furthermore, we need to explore and build the physiological recording systems for in vivo cell or tissue activities, with the aim of checking the stimulation efficiency of these nanostructures. The main steps are briefly described below.

   1.   **Fabrication of implantable and injectable Si/Au nanostructured layer for wireless opto-electric cell stimulation in the first or second NIR biological window with ultralow light intensity, and demonstrate their functionality in vitro and in vivo**.

The implantable nanostructures should be integrated on flexible biocompatible substrates (e.g., PDMS or hydrogels). On the other hand, the injectable nanostructures should match the cellular size, show colloidal stability and capacity to targete specific cells. To achieve these structures, two different strategies could be followed:

   a.   Instead of using standard Si wafers of 525 μm in thickness, the short Si/Au nanostructures could be fabricated on silicon on insulator (SOI) wafers, for enabling easy and flexible removal of the active Si/Au nanostructured layer. The device layer (top Si layer) of the SOI wafers, which can be manufactured to be ~1 μm in thickness, can be used for the implantation to form the p-n junction, and the fabrication of the Si/Au nanostructures. After the nanofabrication steps, the wafer can be cut into desired sizes, then the buried oxide layer (insulation SiO_2 layer) can

be removed by buffered hydrofluoric acid (BHF) wet etching, to release the active Si/Au nanostructured layer. At the same time, the very thin Si/Au nanostructured layer could be transferred onto a biocompatible elastomer like PDMS film for implantation. On the other hand, the released Si/Au nanostructured layer with micrometer scale size could be applied for injection.

b. To further improve the opto-electric performance, the implantable and injectable Si/Au nanostructured layer could be fabricated on amorphous Si with p-i-n junctions. Amorphous Si has higher light absorption than monocrystalline Si, and it is promising to generate higher photovoltages due to its direct and wider bandgap. Besides, it has lower manufacturing cost and can be deposited on flexible substrates.

2. In vivo targeted cell stimulation by the injectable Si/Au nanostructures with ultralow intensity NIR light illumination.

To achieve this goal, it would be necessary to first perform surface modification of the injectable Si/Au nanostructures for targeting specific cells. The Si/Au nanostructures could then be injected or implanted into a rat, and probe the light-induced cell activity through in vivo whole-cell patch-clamp recording techniques.

3. In vivo tissue stimulation by implantable Si/Au nanostructures with ultralow intensity NIR light illumination.

The Si/Au nanostructures could be implanted surgically in the brain or heart of a mouse, then the light-induced brain or heart activities could be recorded through electrophysiology apparatus, e.g. silicon probes of 32-channel linear microelectrode arrays (model A1×32-6mm-50-177, NeuroNexus) for electrophysiological recordings.

4. In vivo targeted cell stimulation by the FeGa/ZnO nanostructures with pulsed light and magnetic field.

To achieve this goal, we would need to perform first surface modification of the FeGa/ZnO nanostructures for specific cell targeting. Then we should probe the induced cell activity through in vivo whole-cell patch-clamp recording techniques.

5. Exploring the polyvinylidene fluoride (PVDF) as alternatives to ZnO layer.

This polymer is interesting due to its efficient piezoelectric and pyroelectric properties after poling. In addition, it is a polymer that exhibits more flexibility, high mechanical strength, good general chemical corrosion resistance, with more compliance for structural integration and lower cost.

References

(1)   Miura, R. M. Analysis of Excitable Cell Models. *J. Comput. Appl. Math.* **2002**, *144* (1–2), 29–47. https://doi.org/10.1016/S0377-0427(01)00550-7.

(2)   Prendergast, A.; Wyart, C. Locomotion: Electrical Coupling of Motor and Premotor Neurons. *Curr. Biol.* **2016**, *26* (6), R235–R237. https://doi.org/10.1016/j.cub.2016.02.021.

(3)   Zanetti, G.; Negro, S.; Megighian, A.; Pirazzini, M. Electrophysiological Recordings of Evoked End-Plate Potential on Murine Neuro-Muscular Synapse Preparations. *Bio-Protocol* **2018**, *8* (8), 1–16. https://doi.org/10.21769/bioprotoc.2803.

(4)   Verkhratsky, A.; Verkhratsky, A.; Olabarria, M.; Noristani, H. N.; Yeh, C. Astrocytes in Alzheimer ' s Disease Astrocytes in Alzheimer ' s Disease. *Nurt* **2010**, *7* (4), 399–412. https://doi.org/10.1016/j.nurt.2010.05.017.

(5)   DeMazumder, D.; Tomaselli, G. F. Molecular and Cellular Mechanisms of Cardiac Arrhythmias. *Muscle* **2012**, *1*, 583–599. https://doi.org/10.1016/B978-0-12-381510-1.00041-7.

(6)   Rogawski, M. A. The A-Current: How Ubiquitous a Feature of Excitable Cells Is It? *Trends Neurosci.* **1985**, *8* (C), 214–219. https://doi.org/10.1016/0166-2236(85)90082-7.

(7)   McKinnon, D. Physiology-of-Electrically-Excitable-Cells.

(8)   Luan, S.; Williams, I.; Nikolic, K.; Constandinou, T. G. Neuromodulation: Present and Emerging Methods. *Front. Neuroeng.* **2014**, *7* (JUL), 1–9. https://doi.org/10.3389/fneng.2014.00027.

(9)   Kung, C.; Blount, P. Channels in Microbes: So Many Holes to Fill. *Mol. Microbiol.* **2004**, *53* (2), 373–380. https://doi.org/10.1111/j.1365-2958.2004.04180.x.

(10)   Acker, C. D.; Singh, M. B.; Antic, S. D. Intracellular Voltage-Sensitive Dyes for Studying Dendritic Excitability and Synaptic Integration. In *Advanced Patch-Clamp Analysis for Neuroscientists*; Korngreen, A., Ed.; Springer New York: New York, NY, 2016; pp 247–265. https://doi.org/10.1007/978-1-4939-3411-9_12.

(11)   Luo, C. H.; Rudy, Y. A Model of the Ventricular Cardiac Action Potential. *Circ. Res.* **1991**, *68* (6), 1501–1526. https://doi.org/10.1161/01.RES.68.6.1501.

(12)   Bean, B. P. The Action Potential in Mammalian Central Neurons. *Nat. Rev. Neurosci.* **2007**, *8* (6), 451–465. https://doi.org/10.1038/nrn2148.

(13)   DM., L. Communication Networks in the Brain: Neurons, Receptors, Neurotransmitters, and Alcohol. *Alcohol Res Heal.* **2008**, *31* (3), 196–214. https://doi.org/10.3109/01443618909151288.

(14)   Pereda, A. E. Electrical Synapses and Their Functional Interactions with Chemical Synapses. *Nat. Rev. Neurosci.* **2014**, *15* (4), 250–263. https://doi.org/10.1038/nrn3708.

(15)   Spruston, N. Pyramidal Neurons: Dendritic Structure and Synaptic Integration.

Nat. Rev. Neurosci. **2008**, *9* (3), 206–221. https://doi.org/10.1038/nrn2286.

(16) Connors, B. W.; Long, M. A. ELECTRICAL SYNAPSES IN THE MAMMALIAN BRAIN. *Annu. Rev. Neurosci.* **2004**, *27* (1), 393–418. https://doi.org/10.1146/annurev.neuro.26.041002.131128.

(17) Furness, J. B. Types of Neurons in the Enteric Nervous System. *J. Auton. Nerv. Syst.* **2000**, *81* (1–3), 87–96. https://doi.org/10.1016/S0165-1838(00)00127-2.

(18) Abraira, V. E.; Ginty, D. D. The Sensory Neurons of Touch. *Neuron* **2013**, *79* (4), 618–639. https://doi.org/10.1016/j.neuron.2013.07.051.

(19) Roper, S. D. Introduction to Signal Processing in Peripheral Sensory Organs. *Semin. Cell Dev. Biol.* **2013**, *24* (1), 1–2. https://doi.org/10.1016/j.semcdb.2012.12.003.

(20) Kandel, E. R.; Schwartz, J. H.; Jessell, T. M.; Jessell, D. of B. and M. B. T.; Siegelbaum, S.; Hudspeth, A. J. *Principles of Neural Science*; McGraw-hill New York, 2000; Vol. 4.

(21) McDonald, T. F.; Pelzer, S.; Trautwein, W.; Pelzer, D. J. Regulation and Modulation of Calcium Channels in Cardiac, Skeletal, and Smooth Muscle Cells. *Physiol. Rev.* **1994**, *74* (2), 365–507. https://doi.org/10.1152/physrev.1994.74.2.365.

(22) Woodcock, E. A.; Matkovich, S. J. Cardiomyocytes Structure, Function and Associated Pathologies. *Int. J. Biochem. Cell Biol.* **2005**, *37* (9), 1746–1751. https://doi.org/https://doi.org/10.1016/j.biocel.2005.04.011.

(23) Dehghani-Samani, A.; Madreseh-Ghafarokhi, S.; Dehghani-Samani, A. Mutations of Voltage-Gated Ionic Channels and Risk of Severe Cardiac Arrhythmias. *Acta Cardiol. Sin.* **2019**, *35* (2), 99–110. https://doi.org/10.6515/ACS.201903_35(2).20181028A.

(24) Stutzmann, G. E.; Mattson, M. P. Endoplasmic Reticulum Ca 2+ Handling in Excitable Cells in Health and Disease. *Pharmacol. Rev.* **2011**, *63* (3), 700–727. https://doi.org/10.1124/pr.110.003814.

(25) Sanders, K. M.; Ward, S. M.; Koh, S. D. Interstitial Cells: Regulators of Smooth Muscle Function. *Physiol. Rev.* **2014**, *94* (3), 859–907. https://doi.org/10.1152/physrev.00037.2013.

(26) Köhrle, J.; Jakob, F.; Contempré, B.; Dumont, J. E. Selenium, the Thyroid, and the Endocrine System. *Endocr. Rev.* **2005**, *26* (7), 944–984. https://doi.org/10.1210/er.2001-0034.

(27) Antonica, F.; Kasprzyk, D. F.; Opitz, R.; Iacovino, M.; Liao, X.-H.; Dumitrescu, A. M.; Refetoff, S.; Peremans, K.; Manto, M.; Kyba, M.; Costagliola, S. Generation of Functional Thyroid from Embryonic Stem Cells. *Nature* **2012**, *491* (7422), 66–71. https://doi.org/10.1038/nature11525.

(28) Päth, G.; Scherbaum, W. A.; Bornstein, S. R. The Role of Interleukin-6 in the Human Adrenal Gland. *Eur. J. Clin. Invest.* **2000**, *30* (s3), 91–95. https://doi.org/10.1046/j.1365-2362.2000.0300s3091.x.

(29) Šišková, Z.; Justus, D.; Kaneko, H.; Friedrichs, D.; Henneberg, N.; Beutel, T.; Pitsch, J.; Schoch, S.; Becker, A.; vonderKammer, H.; Remy, S. Dendritic Structural Degeneration Is Functionally Linked to Cellular Hyperexcitability in a Mouse Model of Alzheimer's Disease. *Neuron* **2014**, *84* (5), 1023–1033.

https://doi.org/10.1016/j.neuron.2014.10.024.

(30) Chen, L.; Hambright, W. S.; Na, R.; Ran, Q. Ablation of the Ferroptosis Inhibitor Glutathione Peroxidase 4 in Neurons Results in Rapid Motor Neuron Degeneration and Paralysis. *J. Biol. Chem.* **2015**, *290* (47), 28097–28106. https://doi.org/10.1074/jbc.M115.680090.

(31) Fiske, J. L.; Fomin, V. P.; Brown, M. L.; Duncan, R. L.; Sikes, R. a. Voltage-Sensitive Ion Channels and Cancer. *Cancer Metastasis Rev.* **2006**, *25* (3), 493–500. https://doi.org/10.1007/s10555-006-9017-z.

(32) Le Scouarnec, S.; Bhasin, N.; Vieyres, C.; Hund, T. J.; Cunha, S. R.; Koval, O.; Marionneau, C.; Chen, B.; Wu, Y.; Demolombe, S.; Song, L. S.; Le Marec, H.; Probst, V.; Schott, J. J.; Anderson, M. E.; Mohler, P. J. Dysfunction in Ankyrin-B-Dependent Ion Channel and Transporter Targeting Causes Human Sinus Node Disease. *Proc. Natl. Acad. Sci. U. S. A.* **2008**, *105* (40), 15617–15622. https://doi.org/10.1073/pnas.0805500105.

(33) Zimliki, C. L.; Chenault, V. M.; Mears, D. Glucose-Dependent and -Independent Electrical Activity in Islets of Langerhans of Psammomys Obesus, an Animal Model of Nutritionally Induced Obesity and Diabetes. *Gen. Comp. Endocrinol.* **2009**, *161* (2), 193–201. https://doi.org/https://doi.org/10.1016/j.ygcen.2008.12.017.

(34) Wustmann, K.; Kucera, J. P.; Zanchi, A.; Burow, A.; Stuber, T.; Chappuis, B.; Diem, P.; Delacrétaz, E. Activation of Electrical Triggers of Atrial Fibrillation in Hyperthyroidism. *J. Clin. Endocrinol. Metab.* **2008**, *93* (6), 2104–2108. https://doi.org/10.1210/jc.2008-0092.

(35) Arlt, W.; Allolio, B. Adrenal Insufficiency. *Lancet* **2003**, *361* (9372), 1881–1893. https://doi.org/https://doi.org/10.1016/S0140-6736(03)13492-7.

(36) Joye, N.; Schmid, A.; Leblebici, Y. An Electrical Model of the Cell-Electrode Interface for High-Density Microelectrode Arrays. *Proc. 30th Annu. Int. Conf. IEEE Eng. Med. Biol. Soc. EMBS'08 - "Personalized Healthc. through Technol.* **2008**, 559–562. https://doi.org/10.1109/iembs.2008.4649214.

(37) Hess, L. H.; Becker-Freyseng, C.; Wismer, M. S.; Blaschke, B. M.; Lottner, M.; Rolf, F.; Seifert, M.; Garrido, J. A. Electrical Coupling between Cells and Graphene Transistors. *Small.* 2015, pp 1703–1710. https://doi.org/10.1002/smll.201402225.

(38) Keren, L. B.; Hanein, Y. Carbon Nanotube Based Multi Electrode Arrays for Neuronal Interfacing: Progress and Prospects. *Front. Neural Circuits* **2012**, No. DEC. https://doi.org/10.3389/fncir.2012.00122.

(39) Tjong, F. V. Y.; Koop, B. E. The Modular Cardiac Rhythm Management System: The EMPOWER Leadless Pacemaker and the EMBLEM Subcutaneous ICD. *Herzschrittmachertherapie und Elektrophysiologie* **2018**, *29* (4), 355–361. https://doi.org/10.1007/s00399-018-0602-y.

(40) Ashkan, K.; Rogers, P.; Bergman, H.; Ughratdar, I. Insights into the Mechanisms of Deep Brain Stimulation. *Nat. Rev. Neurol.* **2017**, *13* (9), 548–554. https://doi.org/10.1038/nrneurol.2017.105.

(41) Fisher, R. S.; Velasco, A. L. Electrical Brain Stimulation for Epilepsy. *Nat. Rev. Neurol.* **2014**, *10* (5), 261–270. https://doi.org/10.1038/nrneurol.2014.59.

(42) Moritz, C. T.; Perlmutter, S. I.; Fetz, E. E. Direct Control of Paralysed Muscles by Cortical Neurons. *Nature* **2008**, *456* (7222), 639–642. https://doi.org/10.1038/nature07418.

(43) Testerman, R. L.; Rise, M. T.; Stypulkowski, P. H. Electrical Stimulation as Therapy for Neurological Disorders: The Basics of Implantable Neurological Stimulators. *IEEE Eng. Med. Biol. Mag.* **2006**, *25* (5), 74–78. https://doi.org/10.1109/MEMB.2006.1705750.

(44) Stingl, K.; Bartz-Schmidt, K. U.; Besch, D.; Braun, A.; Bruckmann, A.; Gekeler, F.; Greppmaier, U.; Hipp, S.; Hortdorfer, G.; Kernstock, C.; Koitschev, A.; Kusnyerik, A.; Sachs, H.; Schatz, A.; Stingl, K. T.; Peters, T.; Wilhelm, B.; Zrenner, E. Artificial Vision with Wirelessly Powered Subretinal Electronic Implant Alpha-IMS. *Proc. R. Soc. B Biol. Sci.* **2013**, *280* (1757), 1–8. https://doi.org/10.1098/rspb.2013.0077.

(45) Stingl, K.; Bartz-Schmidt, K. U.; Besch, D.; Chee, C. K.; Cottriall, C. L.; Gekeler, F.; Groppe, M.; Jackson, T. L.; MacLaren, R. E.; Koitschev, A.; Kusnyerik, A.; Neffendorf, J.; Nemeth, J.; Naeem, M. A. N.; Peters, T.; Ramsden, J. D.; Sachs, H.; Simpson, A.; Singh, M. S.; Wilhelm, B.; Wong, D.; Zrenner, E. Subretinal Visual Implant Alpha IMS - Clinical Trial Interim Report. *Vision Res.* **2015**, *111*, 149–160. https://doi.org/10.1016/j.visres.2015.03.001.

(46) R.V., S. Advances in Auditory Prostheses. *Curr. Opin. Neurol.* **2012**, *25* (1), 61–66. https://doi.org/10.1097/WCO.0b013e32834ef878.Advances.

(47) Besch, D.; Sachs, H.; Szurman, P.; Gülicher, D.; Wilke, R.; Reinert, S.; Zrenner, E.; Bartz-Schmidt, K. U.; Gekeler, F. Extraocular Surgery for Implantation of an Active Subretinal Visual Prosthesis with External Connections: Feasibility and Outcome in Seven Patients. *Br. J. Ophthalmol.* **2008**, *92* (10), 1361–1368. https://doi.org/10.1136/bjo.2007.131961.

(48) Eickenscheidt, M.; Jenkner, M.; Thewes, R.; Fromherz, P.; Stingl, K.; Bartz-schmidt, K. U.; Besch, D.; Braun, A.; Bruckmann, A.; Gekeler, F.; Greppmaier, U.; Hipp, S.; Hörtdörfer, G.; Kernstock, C.; Koitschev, A.; Kusnyerik, A.; Sachs, H.; Schatz, A.; Stingl, K. T.; Wilhelm, B.; Zrenner, E.; Zeck, G. Electrical Stimulation of Retinal Neurons in Epiretinal and Subretinal Configuration Using a Multicapacitor Array Electrical Stimulation of Retinal Neurons in Epiretinal and Subretinal Configuration Using a Multicapacitor Array. 2014, pp 2742–2755. https://doi.org/10.1152/jn.00909.2011.

(49) Bettinger, C. J. Materials Advances for Next-Generation Ingestible Electronic Medical Devices. *Trends Biotechnol.* **2015**, *33* (10), 575–585. https://doi.org/10.1016/j.tibtech.2015.07.008.

(50) Famm, K.; Litt, B.; Tracey, K. J.; Boyden, E. S.; Slaoui, M. A Jump-Start for Electroceuticals. *Nature* **2013**, *496* (7444), 159–161. https://doi.org/10.1038/496159a.

(51) Savchenko, A.; Cherkas, V.; Liu, C.; Braun, G. B.; Kleschevnikov, A.; Miller, Y. I.; Molokanova, E. Graphene Biointerfaces for Optical Stimulation of Cells. *Sci. Adv.* **2018**, *4* (5). https://doi.org/10.1126/sciadv.aat0351.

(52) Guduru, R.; Liang, P.; Hong, J.; Rodzinski, A.; Hadjikhani, A.; Horstmyer, J.; Levister, E.; Khizroev, S. Magnetoelectric "spin" on Stimulating the Brain.

Nanomedicine **2015**, *10* (13), 2051–2061. https://doi.org/10.2217/nnm.15.52.

(53)   Legon, W.; Sato, T. F.; Opitz, A.; Mueller, J.; Barbour, A.; Williams, A.; Tyler, W. J. Transcranial Focused Ultrasound Modulates the Activity of Primary Somatosensory Cortex in Humans. *Nat. Neurosci.* **2014**, *17* (2), 322–329. https://doi.org/10.1038/nn.3620.

(54)   Boyden, E. S.; Zhang, F.; Bamberg, E.; Nagel, G.; Deisseroth, K. Millisecond-Timescale, Genetically Targeted Optical Control of Neural Activity. *Nat. Neurosci.* **2005**, *8* (9), 1263–1268. https://doi.org/10.1038/nn1525.

(55)   Williams, J. C.; Denison, T. From Optogenetic Technologies to Neuromodulation Therapies. *Sci. Transl. Med.* **2013**, *5* (177), 1–4. https://doi.org/10.1126/scitranslmed.3003100.

(56)   Pappas, T. C.; Wickramanyake, W. M. S.; Jan, E.; Motamedi, M.; Brodwick, M.; Kotov, N. a. Nanoscale Engineering of a Cellular Interface with Semiconductor Nanoparticle Films for Photoelectric Stimulation of Neurons. *Nano Lett.* **2007**, *7* (2), 513–519. https://doi.org/10.1021/nl062513v.

(57)   Mathieson, K.; Loudin, J.; Goetz, G.; Huie, P.; Wang, L.; Kamins, T. I.; Galambos, L.; Smith, R.; Harris, J. S.; Sher, A.; Palanker, D. Photovoltaic Retinal Prosthesis with High Pixel Density. *Nat. Photonics* **2012**, *6* (6), 391–397. https://doi.org/10.1038/nphoton.2012.104.

(58)   Jiang, Y.; Tian, B. Inorganic Semiconductor Biointerfaces. *Nat. Rev. Mater.* **2018**, *3* (12), 473–490. https://doi.org/10.1038/s41578-018-0062-3.

(59)   Shapiro, M. G.; Homma, K.; Villarreal, S.; Richter, C.-P.; Bezanilla, F. Infrared Light Excites Cells by Changing Their Electrical Capacitance. *Nat. Commun.* **2012**, *3* (1), 736. https://doi.org/10.1038/ncomms1742.

(60)   Parameswaran, R.; Carvalho-De-Souza, J. L.; Jiang, Y.; Burke, M. J.; Zimmerman, J. F.; Koehler, K.; Phillips, A. W.; Yi, J.; Adams, E. J.; Bezanilla, F.; Tian, B. Photoelectrochemical Modulation of Neuronal Activity with Free-Standing Coaxial Silicon Nanowires. *Nat. Nanotechnol.* **2018**, *13* (3), 260–266. https://doi.org/10.1038/s41565-017-0041-7.

(61)   Delori, F. C.; Webb, R. H.; Sliney, D. H. Maximum Permissible Exposures for Ocular Safety (ANSI 2000), with Emphasis on Ophthalmic Devices. *J. Opt. Soc. Am. A* **2007**, *24* (5), 1250. https://doi.org/10.1364/josaa.24.001250.

(62)   Jiang, Y.; Carvalho-De-Souza, J. L.; Wong, R. C. S.; Luo, Z.; Isheim, D.; Zuo, X.; Nicholls, A. W.; Jung, I. W.; Yue, J.; Liu, D. J.; Wang, Y.; De Andrade, V.; Xiao, X.; Navrazhnykh, L.; Weiss, D. E.; Wu, X.; Seidman, D. N.; Bezanilla, F.; Tian, B. Heterogeneous Silicon Mesostructures for Lipid-Supported Bioelectric Interfaces. *Nat. Mater.* **2016**, *15* (9), 1023–1030. https://doi.org/10.1038/nmat4673.

(63)   Zhou, W.; Dai, X.; Lieber, C. M. Advances in Nanowire Bioelectronics. *Reports Prog. Phys.* **2017**, *80* (1), 16701. https://doi.org/10.1088/0034-4885/80/1/016701.

(64)   Zhang, A.; Lieber, C. M. Nano-Bioelectronics. *Chem. Rev.* **2016**, *116* (1), 215–257. https://doi.org/10.1021/acs.chemrev.5b00608.

(65)   Fang, Y.; Jiang, Y.; Acaron Ledesma, H.; Yi, J.; Gao, X.; Weiss, D. E.; Shi, F.; Tian, B. Texturing Silicon Nanowires for Highly Localized Optical Modulation

of Cellular Dynamics. *Nano Lett.* **2018**, *18* (7), 4487–4492.
https://doi.org/10.1021/acs.nanolett.8b01626.

(66) Jiang, Y.; Li, X.; Liu, B.; Yi, J.; Fang, Y.; Shi, F.; Gao, X.; Sudzilovsky, E.;
Parameswaran, R.; Koehler, K.; Nair, V.; Yue, J.; Guo, K. H.; Fang, Y.; Tsai,
H. M.; Freyermuth, G.; Wong, R. C. S.; Kao, C. M.; Chen, C. T.; Nicholls, A.
W.; Wu, X.; Shepherd, G. M. G.; Tian, B. Rational Design of Silicon
Structures for Optically Controlled Multiscale Biointerfaces. *Nat. Biomed. Eng.*
2018, *2* (7), 508–521. https://doi.org/10.1038/s41551-018-0230-1.

(67) Parameswaran, R.; Koehler, K.; Rotenberg, M. Y.; Burke, M. J.; Kim, J.;
Jeong, K. Y.; Hissa, B.; Paul, M. D.; Moreno, K.; Sarma, N.; Hayes, T.;
Sudzilovsky, E.; Park, H. G.; Tian, B. Optical Stimulation of Cardiac Cells
with a Polymer-Supported Silicon Nanowire Matrix. *Proc. Natl. Acad. Sci. U.
S. A.* **2019**, *116* (2), 413–421. https://doi.org/10.1073/pnas.1816428115.

(68) Xu, J.; Wang, S.; Wang, G.-J. N.; Zhu, C.; Luo, S.; Jin, L.; Gu, X.; Chen, S.;
Feig, V. R.; To, J. W. F.; Rondeau-Gagné, S.; Park, J.; Schroeder, B. C.; Lu,
C.; Oh, J. Y.; Wang, Y.; Kim, Y.-H.; Yan, H.; Sinclair, R.; Zhou, D.; Xue, G.;
Murmann, B.; Linder, C.; Cai, W.; Tok, J. B.-H.; Chung, J. W.; Bao, Z. Highly
Stretchable Polymer Semiconductor Films through the Nanoconfinement
Effect. *Science (80-.).* **2017**, *355* (6320), 59 LP – 64.
https://doi.org/10.1126/science.aah4496.

(69) Bareket-Keren, L.; Hanein, Y. Novel Interfaces for Light Directed Neuronal
Stimulation: Advances and Challenges. *Int. J. Nanomedicine* **2014**, *9*
(SUPPL.1), 65–83. https://doi.org/10.2147/IJN.S51193.

(70) Janssen, R. a. J.; Nelson, J. Factors Limiting Device Efficiency in Organic
Photovoltaics. *Adv. Mater.* **2013**, *25* (13), 1847–1858.
https://doi.org/10.1002/adma.201202873.

(71) Ghezzi, D.; Antognazza, M. R.; Dal Maschio, M.; Lanzarini, E.; Benfenati, F.;
Lanzani, G. A Hybrid Bioorganic Interface for Neuronal Photoactivation. *Nat.
Commun.* **2011**, *2* (1), 164–167. https://doi.org/10.1038/ncomms1164.

(72) Ghezzi, D.; Antognazza, M. R.; MacCarone, R.; Bellani, S.; Lanzarini, E.;
Martino, N.; Mete, M.; Pertile, G.; Bisti, S.; Lanzani, G.; Benfenati, F. A
Polymer Optoelectronic Interface Restores Light Sensitivity in Blind Rat
Retinas. *Nat. Photonics* **2013**, *7* (5), 400–406.
https://doi.org/10.1038/nphoton.2013.34.

(73) Kong, L.; Zepp, R. G. Production and Consumption of Reactive Oxygen
Species by Fullerenes. *Environ. Toxicol. Chem.* **2012**, *31* (1), 136–143.
https://doi.org/10.1002/etc.711.

(74) Maya-Vetencourt, J. F.; Ghezzi, D.; Antognazza, M. R.; Colombo, E.; Mete,
M.; Feyen, P.; Desii, A.; Buschiazzo, A.; Di Paolo, M.; Di Marco, S.; Ticconi,
F.; Emionite, L.; Shmal, D.; Marini, C.; Donelli, I.; Freddi, G.; MacCarone, R.;
Bisti, S.; Sambuceti, G.; Pertile, G.; Lanzani, G.; Benfenati, F. A Fully Organic
Retinal Prosthesis Restores Vision in a Rat Model of Degenerative Blindness.
Nat. Mater. **2017**, *16* (6), 681–689. https://doi.org/10.1038/nmat4874.

(75) Jakešová, M.; Silverå Ejneby, M.; Đerek, V.; Schmidt, T.; Gryszel, M.; Brask,
J.; Schindl, R.; Simon, D. T.; Berggren, M.; Elinder, F.; Głowacki, E. D.
Optoelectronic Control of Single Cells Using Organic Photocapacitors. *Sci.*

Adv. **2019**, *5* (4), eaav5265. https://doi.org/10.1126/sciadv.aav5265.

(76) Rand, D.; Jakešová, M.; Lubin, G.; Vėbraitė, I.; David-Pur, M.; Đerek, V.; Cramer, T.; Sariciftci, N. S.; Hanein, Y.; Głowacki, E. D. Direct Electrical Neurostimulation with Organic Pigment Photocapacitors. *Adv. Mater.* **2018**, *30* (25), 1–11. https://doi.org/10.1002/adma.201707292.

(77) Marciniak, S.; Crispin, X.; Uvdal, K.; Trzcinski, M.; Birgerson, J.; Groenendaal, L.; Louwet, F.; Salaneck, W. R. Light Induced Damage in Poly(3,4-Ethylenedioxythiophene) and Its Derivatives Studied by Photoelectron Spectroscopy. *Synth. Met.* **2004**, *141* (1–2), 67–73. https://doi.org/10.1016/j.synthmet.2003.08.017.

(78) Bodelón, G.; Costas, C.; Pérez-Juste, J.; Pastoriza-Santos, I.; Liz-Marzán, L. M. Gold Nanoparticles for Regulation of Cell Function and Behavior. *Nano Today* **2017**, *13*, 40–60. https://doi.org/10.1016/j.nantod.2016.12.014.

(79) Weissleder, R. A Clearer Vision for in Vivo Imaging. *Nat. Biotechnol.* **2001**, *19* (4), 316–317. https://doi.org/10.1038/86684.

(80) Eom, K.; Kim, J.; Choi, J. M.; Kang, T.; Chang, J. W.; Byun, K. M.; Jun, S. B.; Kim, S. J. Enhanced Infrared Neural Stimulation Using Localized Surface Plasmon Resonance of Gold Nanorods. *Small* **2014**, *10* (19), 3853–3857. https://doi.org/10.1002/smll.201400599.

(81) Yong, J.; Needham, K.; Brown, W. G. a.; Nayagam, B. a.; Mcarthur, S. L.; Yu, A.; Stoddart, P. R. Gold-Nanorod-Assisted Near-Infrared Stimulation of Primary Auditory Neurons. *Adv. Healthc. Mater.* **2014**, *3* (11), 1862–1868. https://doi.org/10.1002/adhm.201400027.

(82) Tang, J.; Qin, N.; Chong, Y.; Diao, Y.; Yiliguma; Wang, Z.; Xue, T.; Jiang, M.; Zhang, J.; Zheng, G. Nanowire Arrays Restore Vision in Blind Mice. *Nat. Commun.* **2018**, *9* (1), 1–13. https://doi.org/10.1038/s41467-018-03212-0.

(83) Carvalho-de-Souza, J. L.; Treger, J. S.; Dang, B.; Kent, S. B. H.; Pepperberg, D. R.; Bezanilla, F. Photosensitivity of Neurons Enabled by Cell-Targeted Gold Nanoparticles. *Neuron* **2015**, *86* (1), 207–217. https://doi.org/10.1016/j.neuron.2015.02.033.

(84) Lavoie-Cardinal, F.; Salesse, C.; Bergeron, É.; Meunier, M.; De Koninck, P. Gold Nanoparticle-Assisted All Optical Localized Stimulation and Monitoring of Ca2+ Signaling in Neurons. *Sci. Rep.* **2016**, *6* (October 2015), 1–9. https://doi.org/10.1038/srep20619.

(85) Murray, C. B.; Kagan, C. R.; Bawendi, M. G. Synthesis and Characterization of Monodisperse Nanocrystals and Close-Packed Nanocrystal Assemblies. *Annu. Rev. Mater. Sci.* **2000**, *30* (1), 545–610. https://doi.org/10.1146/annurev.matsci.30.1.545.

(86) Rossetti, R.; Nakahara, S.; Brus, L. E. Quantum Size Effects in the Redox Potentials, Resonance Raman Spectra, and Electronic Spectra of CdS Crystallites in Aqueous Solution. *J. Chem. Phys.* **1983**, *79* (2), 1086–1088. https://doi.org/10.1063/1.445834.

(87) Koch, S. W. *Semiconductor Quantum Dots*; World Scientific, 1993; Vol. 2.

(88) Ruland, A.; Schulz-Drost, C.; Sgobba, V.; Guldi, D. M. Enhancing Photocurrent Efficiencies by Resonance Energy Transfer in CdTe Quantum

Dot Multilayers: Towards Rainbow Solar Cells. *Adv. Mater.* **2011**, *23* (39), 4573–4577. https://doi.org/10.1002/adma.201101423.

(89) Lugo, K.; Miao, X.; Rieke, F.; Lin, L. Y. Remote Switching of Cellular Activity and Cell Signaling Using Light in Conjunction with Quantum Dots. *Biomed. Opt. Express* **2012**, *3* (3), 447. https://doi.org/10.1364/boe.3.000447.

(90) Chan, W. H.; Shiao, N. H.; Lu, P. Z. CdSe Quantum Dots Induce Apoptosis in Human Neuroblastoma Cells via Mitochondrial-Dependent Pathways and Inhibition of Survival Signals. *Toxicol. Lett.* **2006**, *167* (3), 191–200. https://doi.org/10.1016/j.toxlet.2006.09.007.

(91) Lovrić, J.; Bazzi, H. S.; Cuie, Y.; Fortin, G. R. a.; Winnik, F. M.; Maysinger, D. Differences in Subcellular Distribution and Toxicity of Green and Red Emitting CdTe Quantum Dots. *J. Mol. Med.* **2005**, *83* (5), 377–385. https://doi.org/10.1007/s00109-004-0629-x.

(92) Novoselov, K. S.; Geim, A. K.; Morozov, S. V; Jiang, D.; Zhang, Y.; Dubonos, S. V; Grigorieva, I. V; Firsov, A. A. Electric Field Effect in Atomically Thin Carbon Films. *Science (80-.).* **2004**, *306* (5696), 666 LP – 669. https://doi.org/10.1126/science.1102896.

(93) Yan, L.; Zhao, B.; Liu, X.; Li, X.; Zeng, C.; Shi, H.; Xu, X.; Lin, T.; Dai, L.; Liu, Y. Aligned Nanofibers from Polypyrrole/Graphene as Electrodes for Regeneration of Optic Nerve via Electrical Stimulation. *ACS Appl. Mater. Interfaces* **2016**, *8* (11), 6834–6840. https://doi.org/10.1021/acsami.5b12843.

(94) Kim, S. J.; Cho, K. W.; Cho, H. R.; Wang, L.; Park, S. Y.; Lee, S. E.; Hyeon, T.; Lu, N.; Choi, S. H.; Kim, D. H. Stretchable and Transparent Biointerface Using Cell-Sheet-Graphene Hybrid for Electrophysiology and Therapy of Skeletal Muscle. *Adv. Funct. Mater.* **2016**, *26* (19), 3207–3217. https://doi.org/10.1002/adfm.201504578.

(95) Weissleder, R. A Clearer Vision for in Vivo Imaging. *Nat. Biotechnol.* **2001**, *19* (4), 316–317.

(96) Richter, C.-P.; Matic, A. I.; Wells, J. D.; Jansen, E. D.; Walsh, J. T. Neural Stimulation with Optical Radiation. *Laser Photon. Rev.* **2011**, *5* (1), 68–80. https://doi.org/10.1002/lpor.200900044.

(97) Lorach, H.; Goetz, G.; Smith, R.; Lei, X.; Mandel, Y.; Kamins, T.; Mathieson, K.; Huie, P.; Harris, J.; Sher, A.; Palanker, D. Photovoltaic Restoration of Sight with High Visual Acuity. *Nat. Med.* **2015**, *21* (5), 476–482. https://doi.org/10.1038/nm.3851.

(98) Gentemann, L.; Kalies, S.; Coffee, M.; Meyer, H.; Ripken, T.; Heisterkamp, A.; Zweigerdt, R.; Heinemann, D. Modulation of Cardiomyocyte Activity Using Pulsed Laser Irradiated Gold Nanoparticles. *Biomed. Opt. Express* **2017**, *8* (1), 177. https://doi.org/10.1364/boe.8.000177.

(99) Hallett, M. Transcranial Magnetic Stimulation and the Human Brain. *Nature* **2000**, *406* (6792), 147–150. https://doi.org/10.1038/35018000.

(100) Zangen, A.; Roth, Y.; Voller, B.; Hallett, M. Transcranial Magnetic Stimulation of Deep Brain Regions: Evidence for Efficacy of the H-Coil. *Clin. Neurophysiol.* **2005**, *116* (4), 775–779. https://doi.org/10.1016/j.clinph.2004.11.008.

(101) Yue, K.; Guduru, R.; Hong, J.; Liang, P.; Nair, M.; Khizroev, S. Magneto-Electric Nano-Particles for Non-Invasive Brain Stimulation. *PLoS One* **2012**, *7* (9), 1–5. https://doi.org/10.1371/journal.pone.0044040.

(102) Guduru, R. Bionano Electronics : Magneto-Electric Nanoparticles for Drug Delivery , Brain Stimulation and Imaging Applications. **2013**, 177. https://doi.org/10.25148/etd.FI13112201.

(103) Palneedi, H.; Annapureddy, V.; Priya, S.; Ryu, J. Status and Perspectives of Multiferroic Magnetoelectric Composite Materials and Applications. *Actuators* **2016**, *5* (1). https://doi.org/10.3390/act5010009.

(104) Kargol, A.; Malkinski, L.; Caruntu, G. Biomedical Applications of Multiferroic Nanoparticles. *Adv. Magn. Mater.* **2012**, 89–118.

(105) Chen, X. Z.; Shamsudhin, N.; Hoop, M.; Pieters, R.; Siringil, E.; Sakar, M. S.; Nelson, B. J.; Pané, S. Magnetoelectric Micromachines with Wirelessly Controlled Navigation and Functionality. *Mater. Horizons* **2016**, *3* (2), 113–118. https://doi.org/10.1039/c5mh00259a.

(106) Nair, M.; Guduru, R.; Liang, P.; Hong, J.; Sagar, V.; Khizroev, S. Externally Controlled On-Demand Release of Anti-HIV Drug Using Magneto-Electric Nanoparticles as Carriers. *Nat. Commun.* **2013**, *4*, 1707. https://doi.org/10.1038/ncomms2717.

(107) Wickens, A., Avants, B., Verma, N., Lewis, E., Chen, J.C., Feldman, A.K., Dutta, S., Chu, J., O'Malley, J., Beierlein, M. and Kemere, C. Magnetoelectric Materials for Miniature, Wireless Neural Stimulation at Therapeutic Frequencies. *BioRxiv* **2018**, 461855. https://doi.org/10.1017/CBO9781107415324.004.

(108) Ribeiro, C.; Correia, V.; Martins, P.; Gama, F. M.; Lanceros-Mendez, S. Proving the Suitability of Magnetoelectric Stimuli for Tissue Engineering Applications. *Colloids Surfaces B Biointerfaces* **2016**, *140*, 430–436. https://doi.org/10.1016/j.colsurfb.2015.12.055.

(109) Noh, S. hyun; Moon, S. H.; Shin, T. H.; Lim, Y.; Cheon, J. Recent Advances of Magneto-Thermal Capabilities of Nanoparticles: From Design Principles to Biomedical Applications. *Nano Today*. 2017, pp 61–76. https://doi.org/10.1016/j.nantod.2017.02.006.

(110) Caterina, M. J.; Schumacher, M. A.; Tominaga, M.; Rosen, T. A.; Levine, J. D.; Julius, D. The Capsaicin Receptor: A Heat-Activated Ion Channel in the Pain Pathway. *Nature* **1997**, *389* (6653), 816–824. https://doi.org/10.1038/39807.

(111) Huang, H.; Delikanli, S.; Zeng, H.; Ferkey, D. M.; Pralle, A. Remote Control of Ion Channels and Neurons through Magnetic-Field Heating of Nanoparticles. *Nat. Nanotechnol.* **2010**, *5* (8), 602–606. https://doi.org/10.1038/nnano.2010.125.

(112) Chen, R.; Romero, G.; Christiansen, M. G.; Mohr, A.; Anikeeva, P. Wireless Magnetothermal Deep Brain Stimulation. *Science (80-.).* **2015**, *347* (6229), 1477–1480. https://doi.org/10.1126/science.1261821.

(113) Stanley, S. A.; Gagner, J. E.; Damanpour, S.; Yoshida, M.; Dordick, J. S.; Friedman, J. M. Radio-Wave Heating of Iron Oxide Nanoparticles Can Regulate Plasma Glucose in Mice. *Science (80-.).* **2012**, *336* (6081), 604 LP –

608. https://doi.org/10.1126/science.1216753.

(114) Chen, R.; Canales, A.; Anikeeva, P. Neural Recording and Modulation Technologies. *Nat. Rev. Mater.* **2017**, *2* (2), 1–16.

(115) Taflove, A.; Hagness, S. C.; Piket-May, M. Computational Electromagnetics: The Finite-Difference Time-Domain Method. *Electr. Eng. Handb.* **2005**, *3*.

(116) Chu, P. K.; Wu, G. S. *Surface Design of Biodegradable Magnesium Alloys for Biomedical Applications*; 2015; Vol. 1. https://doi.org/10.1016/B978-1-78242-077-4.00003-6.

(117) Ai, B.; Möhwald, H.; Wang, D.; Zhang, G. Advanced Colloidal Lithography Beyond Surface Patterning. *Adv. Mater. Interfaces* **2017**, *4* (1). https://doi.org/10.1002/admi.201600271.

(118) Caruso, F.; Lichtenfeld, H.; Giersig, M.; Mohwald, H. Electrostatic Self-Assembly of Silica Nanoparticle-Polyelectrolyte Multilayers on Polystyrene Latex Particles [4]. *J. Am. Chem. Soc.* **1998**, *120* (33), 8523–8524. https://doi.org/10.1021/ja9815024.

(119) Kelly, P. J.; Arnell, R. D. Magnetron Sputtering: A Review of Recent Developments and Applications. *Vacuum* **2000**, *56* (3), 159–172. https://doi.org/https://doi.org/10.1016/S0042-207X(99)00189-X.

(120) Graham, F. L.; Smiley, J.; Russell, W. C.; Nairn, R. Characteristics of a Human Cell Line Transformed by DNA from Human Adenovirus Type 5. *J. Gen. Virol.* **1977**, *36* (1), 59–72. https://doi.org/10.1099/0022-1317-36-1-59.

(121) Walter, M. G.; Warren, E. L.; McKone, J. R.; Boettcher, S. W.; Mi, Q.; Santori, E. A.; Lewis, N. S. Solar Water Splitting Cells. *Chem. Rev.* **2010**, *110* (11), 6446–6473. https://doi.org/10.1021/cr1002326.

(122) Ouyang, W.; Teng, F.; He, J. H.; Fang, X. Enhancing the Photoelectric Performance of Photodetectors Based on Metal Oxide Semiconductors by Charge-Carrier Engineering. *Adv. Funct. Mater.* **2019**, *29* (9), 1–20. https://doi.org/10.1002/adfm.201807672.

(123) Liu, Q.; Kidd, P. B.; Dobosiewicz, M.; Bargmann, C. I. C. Elegans AWA Olfactory Neurons Fire Calcium-Mediated All-or-None Action Potentials. *Cell* **2018**, *175* (1), 57-70.e17. https://doi.org/10.1016/j.cell.2018.08.018.

(124) Patolsky, F.; Timko, B. P.; Yu, G.; Fang, Y.; Greytak, A. B.; Zheng, G.; Lieber, C. M. Detection, Stimulation, and Inhibition of Neuronal Signals with High-Density Nanowire Transistor Arrays. *Science (80-.).* **2006**, *313* (5790), 1100 LP – 1104. https://doi.org/10.1126/science.1128640.

(125) Button, V. L. D. S. N. *Electrodes for Biopotential Recording and Tissue Stimulation*; 2015. https://doi.org/10.1016/b978-0-12-800774-7.00002-7.

(126) Vogel, R. W. Understanding Anodal and Cathodal Stimulation. *ASNM Monit.* **2017**.

(127) Cameron, M. A.; Al Abed, A.; Buskila, Y.; Dokos, S.; Lovell, N. H.; Morley, J. W. Differential Effect of Brief Electrical Stimulation on Voltage-Gated Potassium Channels. *J. Neurophysiol.* **2017**, *117* (5), 2014–2024. https://doi.org/10.1152/jn.00915.2016.

(128) Hemmer, E.; Benayas, A.; Légaré, F.; Vetrone, F. Exploiting the Biological Windows: Current Perspectives on Fluorescent Bioprobes Emitting above 1000

Nm. *Nanoscale Horizons* **2016**, *1* (3), 168–184.

Curriculum vitae

PERSONAL INFORMATION

Yue Zhang

Birthday: 16/12/1989

Nationality: China

E-mail: yuezh99@gmail.com

EDUCATION

Sep. 2008 ~ Jun. 2012	**Bachelor**	**Wuhan University of Technology**
		School of Material Science and Engineering
		Major: Inorganic Non-metallic Material Engineering

Sep. 2012 ~ Jan. 2015	**Master**	**Wuhan University of Technology**
		State Key Laboratory of Advanced Technology for Material Progressing
		Major: Advanced energy material

Oct. 2016 ~ Sep. 2020	**Ph.D**	**University of Barcelona**

Oct. 2016~Jun. 2017
Catalonia Institute for Energy Research (IREC)

Jul. 2017~ Sep. 2020
Catalan institute of nanoscience and nanotechnology (ICN2)
Barcelona microelectronics institute of national microelectronics center (IBM-CNM)

Doctoral program: Nanoscience

Project: Wireless opto-electric and magneto-electric nanoactuators for biomedical application

WORKING EXPERIENCE

Apr. 2015 ~ Jul. 2016: SAIC MOTOR CORPORATION LIMITED, CHINA.

- Worked in Research &Advanced Technology Division, focused on development of proton exchange membrane fuel cell (PEMFC) key materials.
- Responsible for contacting with international suppliers of PEMFC key components.

RESEARCH EXPERIENCE

Jul. 2017 ~ Sep.2020   Ph.D

- Design and development of Si photodiode nanoactuators for wireless opto-electric stimulation of excitable cells.
- Nanofabrication of magneto-opto-electric nanostructures for wireless cell modulation.

Sep. 2012 ~ Jan. 2015   Master

- Electropolymerization and characterization of ordered polyaniline nanofibers, and its application in supercapacitors.
- 2000 hours durability study of the proton exchange membrane fuel cell (PEMFC) stack.

PUBLICATIONS

1. Albert Serrà, **Yue Zhang**, Borja Sepúlveda, Elvira Gómez, Josep Nogués, Johann Michler, and Laetitia Philippe. "Highly reduced ecotoxicity of ZnO-based micro/nanostructures on aquatic biota: Influence of architecture, chemical composition, fixation, and photocatalytic efficiency." Water research 169 (2020): 115210.
2. Albert Serrà, **Yue Zhang**, Borja Sepúlveda, Elvira Gómez, Josep Nogués, Johann Michler, and Laetitia Philippe. "Highly active ZnO-based biomimetic fern-like microleaves for photocatalytic water decontamination using sunlight." Applied Catalysis B: Environmental 248 (2019): 129-146.
3. **Yue Zhang**, Guangjin Wang, Mu Pan. Fast electropolymerization of Polyaniline Nanofibers on Carbon Paper. Chemical Journal of Chinese Universities. 2014, 35(10): 2234-2238.
4. **Yue Zhang**, Guangjin Wang, Shuang Sun, Mu Pan. Research Progress of Nanostructure Polyaniline and Polyaniline Nanocomposites. Materials Review, 2014, 28(02):56-59.

CONFERENCE

1. **Yue Zhang**, et al. 2nd International Conference on Photonics Research, Antalya, Turkey, November 2019.

SKILLS & QUALIFICATIONS

- **English**: IELTS (6.0).
- **Spanish**: Certificate A1, basic level.
- **Laboratory:** Proficient in Electron beam evaporation, ICP-RIE for semiconductor fabrication, SEM, XRD, UV-Vis, electrochemical testing.

List of publications

1. Serrà, A., **Zhang, Y**., Sepúlveda, B., Gómez, E., Nogués, J., Michler, J. and Philippe, L., 2019. Highly active ZnO-based biomimetic fern-like microleaves for photocatalytic water decontamination using sunlight. *Applied Catalysis B: Environmental*, *248*, pp.129-146.

2. Serrà, A., **Zhang, Y**., Sepúlveda, B., Gómez, E., Nogués, J., Michler, J. and Philippe, L., 2020. Highly reduced ecotoxicity of ZnO-based micro/nanostructures on aquatic biota: Influence of architecture, chemical composition, fixation, and photocatalytic efficiency. *Water research*, *169*, p.115-210.

Annex

Highly active ZnO-based biomimetic fern-like microleaves for photocatalytic water decontamination using sunlight

Albert Serrà[a,*], Yue Zhang[b], Borja Sepúlveda[b], Elvira Gómez[c,d], Josep Nogués[b,e], Johann Michler[a], Laetitia Philippe[a,*]

[a] Empa Swiss Federal Laboratories for Materials Science and Technology, Laboratory for Mechanics of Materials and Nanostructures, Feuerwerkerstrasse 39, CH-3602 Thun, Switzerland
[b] Catalan Institute of Nanoscience and Nanotechnology (ICN2), CSIC and BIST, Campus UAB, Bellaterra, E-08193 Barcelona, Spain
[c] Grup d'Electrodeposició de Capes Primes i Nanoestructures (GE-CPN), Departament de Ciència de Materials i Química Física, Universitat de Barcelona, Martí i Franquès, 1, E-08028, Barcelona, Catalonia, Spain
[d] Institute of Nanoscience and Nanotechnology (IN²UB), Universitat de Barcelona, Barcelona, Catalonia, Spain
[e] ICREA, Pg. Lluís Companys 23, E-08010, Barcelona, Spain

ARTICLE INFO

ABSTRACT

Here we present the highly enhanced sunlight photocatalytic efficiency and photocorrosion resistance of biomimetic ZnO-modified micro/nanofern fractal architectures, which are synthesized by using a novel, simple, inexpensive and green electrochemical deposition approach in high stirring conditions. Such fern-like hierarchical structures simultaneously combine enhanced angle independent light trapping and surface/bulk modifications of the ZnO morphology to drastically increase: i) the light trapping and absorption in the visible nearinfrared range, and ii) the surface to volume ratio of the architecture. This combination is crucial for boosting the sunlight photocatalytic efficiency. To modulate the electronic properties for extending the operation of the ZnO photocatalysts into the visible domain we have used three different modification approaches: sulfidation (leading to a ZnS shell), Ag decoration, and Ni-doping. The different ZnO-modified bioinspired fern-like fractal structures have been used to demonstrate their efficiency in the photodegradation and photoremediation of three different persistent organic pollutants –methylene blue, 4-nitrophenol, and Rhodamine B – under UV light, simulated and natural UV-filtered sunlight. Remarkably, the ZnO@ZnS core@shell structures exhibited an outstanding photocatalytic activity compared to the pristine ZnO catalyst, with over 6-fold increase in the pollutant degradation rate when using solar light. In fact, the catalytic performance of the ZnO@ZnS micro/nanoferns for the photoremediation of persistent organic pollutants is comparable to or better than the most competitive state-of-the-art ZnO photocatalysts, but showing a negligible photocorrosion. Ag-decorated ZnO, and Ni-doped ZnO exhibited similar excellent visible-sunlight photodegradation efficiency. Although the Ni-doped photocatalysts showed a relatively poor photocorrosion resistance, it was acceptable for Ag-decorated ZnO. Therefore, the easy fabrication and the capacity to drastically enhance the sunlight photocatalytic efficiency of the ZnO@ZnS bioinspired micro/nanoferns, together with their practically negligible photocorrosion and simple recyclability in terms of non-catalyst poisoning, makes them very promising photocatalysts for water remediation.
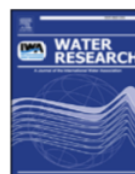
Highly reduced ecotoxicity of ZnO-based micro/nanostructures on aquatic biota: Influence of architecture, chemical composition, fixation, and photocatalytic efficiency

Albert Serrà [a, *], Yue Zhang [b], Borja Sepúlveda [b], Elvira Gómez [c, d], Josep Nogués [b, e], Johann Michler [a], Laetitia Philippe [a]

[a] Empa, Swiss Federal Laboratories for Materials Science and Technology, Laboratory for Mechanics of Materials and Nanostructures, Feuerwerkerstrasse 39, CH-3602, Thun, Switzerland
[b] Catalan Institute of Nanoscience and Nanotechnology (ICN2), CSIC and BIST, Campus UAB, Bellaterra, E-08193, Barcelona, Spain
[c] Grup d'Electrodeposició de Capes Primes i Nanoestructures (GE-CPN), Departament de Ciència de Materials i Química Física, Universitat de Barcelona, Martí i Franquès, 1, E-08028, Barcelona, Catalonia, Spain
[d] Institute of Nanoscience and Nanotechnology (IN²UB), Universitat de Barcelona, Barcelona, Catalonia, Spain
[e] ICREA, Pg. Lluís Companys 23, E-08010, Barcelona, Spain

ARTICLE INFO

ABSTRACT

Developing efficient sunlight photocatalysts with enhanced photocorrosion resistance and minimal ecotoxicological effects on aquatic biota is critical to combat water contamination. Here, the role of chemical composition, architecture, and fixation on the ecotoxicological effects on microalgae of different ZnO and ZnO@ZnS based water decontamination photocatalysts was analyzed in depth. In particular, the ecotoxicological effects of films, nanoparticles and biomimetic micro/nano-ferns were carefully assessed by correlating the algae's viability to the Zn(II) release, the photocatalyst—microalgae interaction, and the production of reactive oxygen species (ROS). The results showed a drastic improvement in algal viability for supported ZnO@ZnS core@shell micro/nanoferns, as their ecotoxicity after 96 h light exposure was significantly lower (3.7−10.0% viability loss) compared to the ZnO films (18.4−35.5% loss), ZnO micro/nanoferns (28.5−53.5% loss), ZnO nanoparticles (48.3−91.7% loss) or ZnO@ZnS nanoparticles (8.6−19.2% loss) for catalysts concentrations ranging from 25 mg L^{-1} to 400 mg L^{-1}. In particular, the ZnO@ZnS micro/nanoferns with a concentration of 400 mg L^{-1} exhibited excellent photocatalytic efficiency to mineralize a multi-pollutant solution (81.4 ± 0.3% mineralization efficiency after 210 min under UV-filtered visible light irradiation) and minimal photocorrosion (<5% of photocatalyst dissolution after 96 h of UV-filtered visible light irradiation). Remarkably, the ZnO@ZnS micro/nanoferns showed lower loss of algal viability (9.8 ± 1.1%) after 96 h of light exposure, with minimal reduction in microalgal biomass (9.1 ± 1.0%), as well as in the quantity of chlorophyll-a (9.5 ± 1.0%), carotenoids (8.6 ± 0.9%) and phycocyanin (5.6 ± 0.6%). Altogether, the optimized ZnO@ZnS core@shell micro/nanoferns represent excellent ecofriendly photocatalysts for water remediation in complex media, as they combine enhanced sunlight remediation efficiency, minimal adverse effects on biological microorganisms, high reusability and easy recyclability.

127